SANDIA REPORT
SAND2009-0351
Unlimited Release
Printed January 2009

Experimental Assessment of Unvalidated Assumptions in Classical Plasticity Theory

Rebecca Brannon, Jeffrey A. Burghardt, David Bronowski, Stephen Bauer

Prepared by
Sandia National Laboratories
Albuquerque, New Mexico 87185 and Livermore, California 94550

Sandia is a multiprogram laboratory operated by Sandia Corporation,
a Lockheed Martin Company, for the United States Department of Energy's
National Nuclear Security Administration under Contract DE-AC04-94-AL85000.

Approved for public release; further dissemination unlimited.



Issued by Sandia National Laboratories, operated for the United States Department of Energy by Sandia Corporation.

NOTICE: This report was prepared as an account of work sponsored by an agency of the United States Government. Neither the United States Government, nor any agency thereof, nor any of their employees, nor any of their contractors, subcontractors, or their employees, make any warranty, express or implied, or assume any legal liability or responsibility for the accuracy, completeness, or usefulness of any information, apparatus, product, or process disclosed, or represent that its use would not infringe privately owned rights. Reference herein to any specific commercial product, process, or service by trade name, trademark, manufacturer, or otherwise, does not necessarily constitute or imply its endorsement, recommendation, or favoring by the United States Government, any agency thereof, or any of their contractors or subcontractors. The views and opinions expressed herein do not necessarily state or reflect those of the United States Government, any agency thereof, or any of their contractors.

Printed in the United States of America. This report has been reproduced directly from the best available copy.

Available to DOE and DOE contractors from
U.S. Department of Energy
Office of Scientific and Technical Information
P.O. Box 62
Oak Ridge, TN 37831

Telephone: (865) 576-8401
Facsimile: (865) 576-5728
E-Mail: reports@adonis.osti.gov
Online ordering: http://www.osti.gov/bridge

Available to the public from
U.S. Department of Commerce
National Technical Information Service
5285 Port Royal Rd
Springfield, VA 22161

Telephone: (800) 553-6847
Facsimile: (703) 605-6900
E-Mail: orders@ntis.fedworld.gov
Online ordering: http://www.ntis.gov/help/ordermethods.asp?loc=7-4-0#online



SAND2009-0351
Unlimited Release
Printed January 2009

Experimental Assessment of Unvalidated Assumptions in Classical Plasticity Theory

Rebecca Brannon
University of Utah Mechanical Engineering
50 S. Central Campus Drive
2134 MEB
Salt Lake City, UT 84112
Rebecca.Brannon@utah.edu

Jeffrey A. Burghardt
University of Utah Mechanical Engineering
50 S. Central Campus Drive
2255 MEB
Salt Lake City, UT 84112
jeff788@gmail.com

David R. Bronowski
Geomechanics, Dept 06315
Sandia National Laboratories
Albuquerque, NM 87185-1031
drbrono@sandia.gov

Stephen J Bauer
Geomechanics, Dept 06315
Sandia National Laboratories
Albuquerque, NM 87185-1033
sjbauer@sandia.gov

Abstract

This report investigates the validity of several key assumptions in classical plasticity theory regarding material response to changes in the loading direction. Three metals, two rock types, and one ceramic were subjected to non-standard loading directions, and the resulting strain response increments were displayed in Gudehus diagrams to illustrate the approximation error of classical plasticity theories. A rigorous mathematical framework for fitting classical theories to the data, thus quantifying the error, is provided. Further data analysis techniques are presented that allow testing for the effect of changes in loading direction without having to use a new sample and for inferring the yield normal and flow directions without having to measure the yield surface. Though the data are inconclusive, there is indication that classical, incrementally linear, plasticity theory may be inadequate over a certain range of loading directions. This range of loading directions also coincides with loading directions that are known to produce a physically inadmissible instability for any nonassociative plasticity model.

Contents

1 Introduction **11**

2 Terminology and Mathematics **17**

Regular Flow Rule 19

Dimensional reduction for axisymmetric loading 20

Visualization of linear transformations 22

Data interpolation to a single state 24

Non-Associated Flow Rule 27

Effect of Triaxial Compression on Hydrostatic Limit 30

3 Axisymmetric Plasticity **35**

4 Methodology **39**

Flow Rule Validation 39

Cap Model Hardening Validation 42

5 Testing Procedure **45**

Sample Preparation 45

Test Method 47

Calibration 50

6 Discussion of Results **53**

Regular Flow Rule 53

Non-associated Flow Rule 56

Cap Model Validation 57

7 Conclusions **59**

References **61**

Appendix

A Summary of Tests **63**

A.1 Cap Model Validation Tests 63

A.2 Flow Rule Validation Tests 69

List of Figures

1.1 Results of ACTD Mohr-Coulomb Verification Study 12

1.2 Common isotropic yield surfaces. Von Mises and Drucker-Prager models are often used for metals. Gurson's function, and others like it, are used for porous media. Tresca and Mohr-Coulomb models approximate the yield threshold for brittle media. Fossum's model, and others like it, combine these features to model realistic geological media. 14

2.1 Visualization of vector transformations. 23

2.2 Triaxial compression load path used in DEM simulations performed by Tamagnini. Here q is the equivalent shear stress, and p is the mean stress. Also ε_z is the strain in the z(axial)-direction, and ε_v is the volumetric strain. The points at which stress probes were applied are labeled B and B'. (Courtesy of C. Tamagnini) 25

2.3 Results of Tamagnini's DEM stress probe simulations. A set of axisymmetric stress increments represented by a unit circle in stress space (left), and the resulting strain increments mapped to strain space (right). 26

2.4 Strain response envelope for axisymmetric stress probes at stress state B' from Tamagnini's DEM simulations. (Courtesy of C. Tamagnini) 27

2.5 Results of Tamagnini's DEM stress probe simulations. A set of deviatoric stress increments represented by a unit circle in stress space (left), and the resulting strain increments mapped to strain space (right). (Courtesy of C. Tamagnini) 28

2.6 Semi-infinite solid with initial stress state placing it on the Ducker-Prager yield surface. The perturbation is designed such that it loads the material into the Sandler-Rubin wedge. (Figure from unpublished work of T.A. Pučik [23]) 30

2.7 The yield surface and plastic potential with the Sandler-Rubin wedge illustrated. (Figure from unpublished work of T.A. Pučik [23]) 31

2.8 Possible analytical solutions to the example problem of Fig. 2.6 (derived by Pučik [23]). Pučik's analytical solution resulted in a family of solutions with two free parameters (v_p and $\dot{\sigma}_p$). Each set of plots represents a different choice for the free parameter $\dot{\sigma}_p$, as labeled. The plots on the left show a propagating triangular stress pulse, while the plots on the right show the corresponding velocity profiles. 32

2.9 Some finite-element solutions to the Pučik wave-propagation problem. (Simulations performed by Pučik [23]) The plots on the left represent stress profiles of the shock wave, while the plots on the right represent the velocity profiles of the shock wave. Each plot shows the profile of the wave at various distances into the material. Each case was performed with the exact same material properties and boundary conditions. The only different was a slight change of the initial positions of the nodes (on the order of round-off error). 33

4.1 A simple cyclically applied incremental loading. Solid vector lines indicate stress vectors, dotted vector lines indicate strain vectors. 40

4.2 Sketch of a triaxial compression test (bold arrow) with a corresponding unvalidated yield surface evolution that predicts outward motion of the cap even after onset of dilatation; in the theoretical model under investigation, the onset of dilatation corresponds to the point where the load path crosses over the peak point of the evolving cap. 43

5.1 Strain gaged aluminum specimens 46

5.2 Right circular cylinder of Castlegate sandstone. 47

5.3 Right circular cylinder of Castlegate sandstone jacketed in copper with end caps attached. 48

5.4 Right circular cylinder of deformed Castlegate sandstone, showing the complete sample assembly with axial and radial LVDTs 49

5.5 Testing system used to conduct quasi-static triaxial compression tests. 50

6.1 Response envelopes for the second stress cycle of tests LP-TA22 (a), LP-TA23 (a) and LP-TA24 (c). Black dots indicate total strain increments, red dots indicate plastic strain increments. All strain increments have been interpolated to a common material state using a cyclical loading cycle. The partial ellipses are a visualization of the best fit tangent stiffness tensors C (black) and T (gray), which were found via a pseudo-inverse method using the four stress/strain increment pairs. These ellipses represent a circle in stress space mapped to strain space. 54

6.2 Response envelopes for the third stress cycle of tests LP-TA22 (a), LP-TA23 (b) and LP-TA24 (c). Black dots indicate total strain increments, red dots indicate plastic strain increments. All strain increments have been interpolated to a common material state using a cyclical loading cycle. The partial ellipses are a visualization of the best fit tangent stiffness tensors C (black) and T (gray), which were found via a pseudo-inverse method using the four stress/strain increment pairs. These ellipses represent a circle in stress space mapped to strain space. 55

6.3 The σ_r vs. ε_r stress strain curve for test LP-TA20, illustrating the initial anisotropy in the material. The anisotropy is evidenced by the change (decrease) in the strain ε_r during the initial hydrostatic loading leg of the test where the σ_r stress remains nearly constant. This indicates that the material is undergoing a shear deformation due to a purely hydrostatic loading. 57

6.4 Validation of a geomechanics model for loading of Sidewinder Tuff under triaxial compression [27]. (Note: the present work aims to extend validation for changes in the loading direction away from standard triaxial compression load paths of this kind.) 58

List of Tables

5.1 Experiment number, test date, specimen dimensions and confining pressure. 51

6.1 Description of stress increments where α is the angle formed with the hydrostatic compression axis, and $\dot{\Sigma}$ is the total increment magnitude. 53

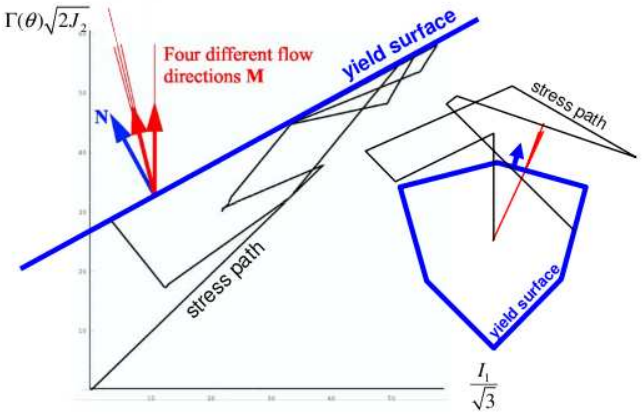
6.2 Direction of the yield surface normal N and the plastic strain rate M referenced to the hydrostatic compression axis. 56

Chapter 1

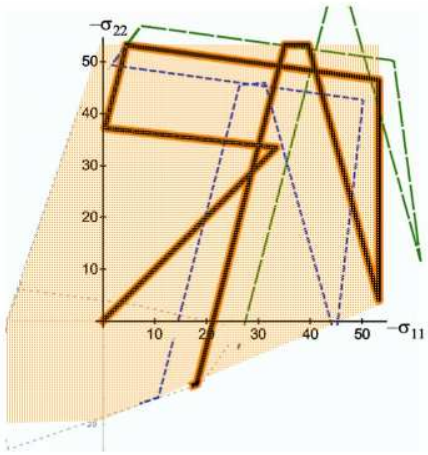
Introduction

Predicting inelastic material response is key in several active Sandia mission areas including penetration and impact, vulnerability assessment, hydrocarbon reservoir and porous media. Essential to these predictions is the use of generalized plasticity and damage models. Many problems of practical importance induce significant changes in the loading directions. For example, in a penetration problem, the material near the impact point first experiences a nearly uniaxial strain loading upon passage of the initial shock wave, but then the stress state transitions toward simple shear as the penetrator itself passes. Virtually every plasticity model at Sandia (and elsewhere) relies on unvalidated theories for predicting material response to changes in loading direction. However, laboratory testing for parameterizing engineering plasticity models is typically limited to unidirectional axisymmetric compression, thus forcing guesswork in the development of constitutive models to predict material response for deviations from calibration test load directions. This uncertainty in the physical foundations of the governing equations must be eliminated via systematic validation experiments. Without such validation, much doubt is cast on the results of any simulation that uses a model to simulate load paths that significantly deviate from the load paths used in calibration testing. For example, rocks and rock-like materials often exhibit non-associativity of the plastic flow direction when they are loaded in triaxial compression. Under classical plasticity theory, the non-associative flow direction observed in this one calibration loading direction (triaxial compression) is then assumed – without proof – to apply to *all* loading directions. Suppose, however, that (contrary to classical plasticity theory) the flow direction should actually vary with the loading direction. How much error can be expected by neglecting the variation? To illustrate sensitivity of simulation results to modeling uncertainty in the flow direction, Fig. 1.1 shows a verification problem that was part of an ACTD inter-agency V&V study. For prescribed Mohr-Coulomb parameters, this problem prescribes a highly variable strain path for which the analytical solution is known be the plane stress response shown by the thick orange line in Fig. 1.1. The dashed lines in that figure show that a small (2°) change in the flow direction M produces a large (˜10%) change in the stress response – even inducing significant deviation from plane stress. This sensitivity study suggests that large validation errors under general loading can be expected if the classical assumption of a path-insensitive flow direction is even slightly inappropriate.

"Engineering plasticity models" are here defined to be those that are simple enough in their structure, efficiency, and robustness to be practical for large scale engineering applications. To date, this means that engineering plasticity models are usually phenomenological and, for tractability, often include simplifying assumptions (such as isotropy) that have not been well justified in the laboratory. More complicated approaches might apply first-principles materials science [1] or



Lode-normalized meridional and octahedral yield surface profiles (with normal **N** and four flow directions **M**). The central reference flow direction (middle of red cluster) and the strain path were designed to give plane stress response. The multiplier $\Gamma(\theta)$ transforms the distorted hexagon and stress path to a circle for normalization in the meridional view (i.e., converts to an equivalent Drucker-Prager space strictly for the purpose of visualization).



Thick orange and *thin black* (overlaid) lines are the analytical and simulated plane-stress solution using the central reference flow direction (solid fill is the elastic domain). Blue and green dashed lines are the results using the same prescribed strain path with only slightly different flow directions (less than 2° error in **M** produces ~10% error in stress, even large excursions from plane stress conditions). The light grey dashed line is the deviatoric associativity solution (different from the baseline analytical solution by orders of magnitude).

Figure 1.1. Results of ACTD Mohr-Coulomb Verification Study

atomistic modeling [2] or mesoscale modeling [3] to explicitly account for microstructural aspects such as grain boundary effects on dislocations, crack and inclusion distributions obtained from tomography, etc. [4]. However, even the advanced theories are not exempt from validation, since they also rely on numerous unproven assumptions. Although the computational overhead of these more sophisticated theories often precludes their direct use in engineering applications, they still serve as valuable resources for improving predictions of engineering plasticity theories in domains for which experimental data are not available.

This report describes systematic laboratory investigations of the validity of some fundamental assumptions that are common to virtually every engineering plasticity model. Of particular interest is a need to determine material behavior for a particular loading direction that is known to theoretically admit a physically inadmissible instability if the material is modeled using *any* classical, non-associative, rate-independent, engineering plasticity theory. As discussed in detail later, the unstable range of loading directions forms a “wedge” in stress space (above yield but below the flow surface) that is located far away from the probing direction used in standard parameterization testing. Therefore, the primary goal of our laboratory investigation is to probe material response in or near this wedge. More broadly, the goals are (1) to design inexpensive methods for exploring the effect of a variety of non-standard loading directions and (2) to develop means of analyzing the

data without introducing unnecessary constitutive assumptions.

Non-standard loading is also needed to investigate a prediction of some plasticity models for rocks and ceramics that dilatate in compression (attributed to opening of microcracks in shear) actually strengthens the material in hydrostatic compression. This result seems to contradict the commonly held view that an increase in void space should decrease the hydrostatic elastic limit pressure. The concern is that efforts to reproduce a very limited data set (shear-enhanced dilatation) might have resulted in a model that gives very poor predictions for changes in loading direction from that state. This is just one example of a more broad observation that engineering plasticity models are typically designed to match unidirectional model parameterization tests, yet such models repeatedly are non-predictive in more complicated validation tests that usually involve far more complicated changes in loading. Clearly, laboratory testing for plasticity models needs to be expanded to include a greater variety of loading directions, beyond the minimum needed to merely parameterize the models.

Relative to simplistic plasticity models such as von Mises or Tresca theory, the somewhat more realistic engineering plasticity models such as Johnson-Cook theory [5] and the Sandia GeoModel [6], allow many more factors to alter the material response. In such models (as well as in simpler models), the stress rate ($\dot{\sigma}$) is assumed to be a function of the strain rate ($\dot{\varepsilon}$), current state of stress (σ), and a set of internal state variables ($\eta_1, \eta_2, ...$) that characterize the internal structure of the material. The internal variables are themselves *functionals* of the loading history, giving rise to path dependence. Setting aside the details of any particular model, engineering plasticity theories are typically written in the following basic incremental form:

$$\dot{\sigma} = \mathscr{H}(\dot{\varepsilon}, \sigma, \eta_1, \eta_2, ...). \tag{1.1}$$

Here, a superimposed dot may be regarded as an increment or time rate (where, for rate-independent plasticity "time" is any monotonically increasing scalar parameterizing the deformation path). In laboratory work, it is often presumed that the roles of stress and strain can be reversed in Eq. (1.1) so that the stress increment is the controlled independent variable, while the strain increment is the measured dependent variable. Such a view will be adopted in our experimental investigations. Most plasticity theories assume that there exists a scalar-valued yield function (f) such that elastic deformation occurs when

$$f(\sigma, \eta_1, \eta_2 ...) < 0. \tag{1.2}$$

For isotropic plasticity models, the zeros of this function are often plotted as an isosurface (called the yield surface) in three-dimensional principal stress space, as illustrated in Fig. (1.2).

This yield function is used to determine if elasticity theory or plasticity theory is used to describe a given deformation. This is done as follows:

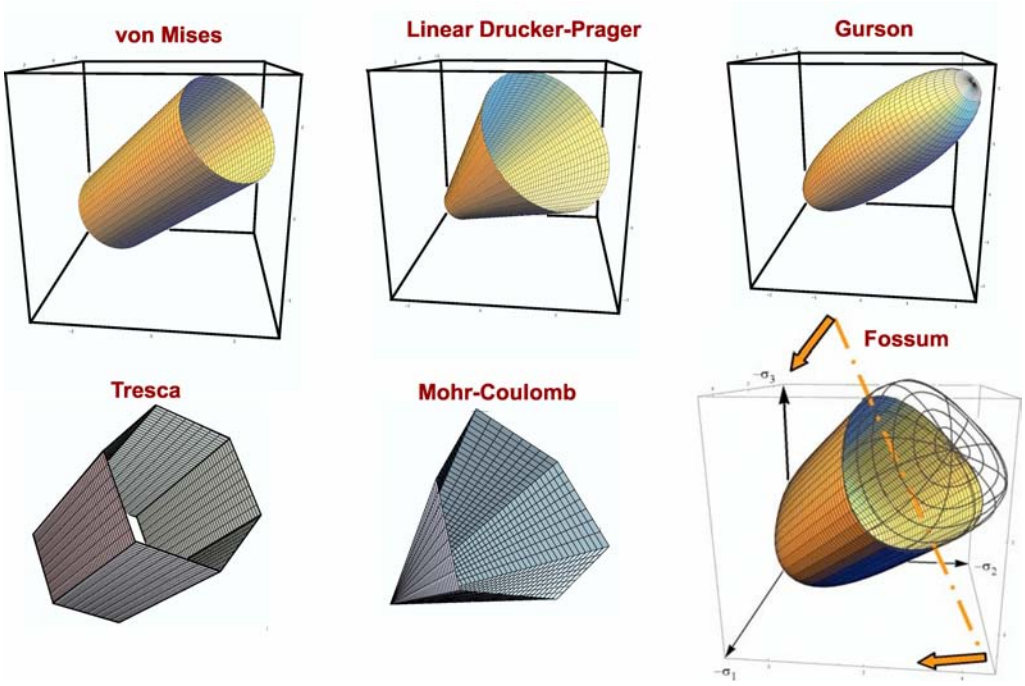


Figure 1.2. Common isotropic yield surfaces. Von Mises and Drucker-Prager models are often used for metals. Gurson's function, and others like it, are used for porous media. Tresca and Mohr-Coulomb models approximate the yield threshold for brittle media. Fossum's model, and others like it, combine these features to model realistic geological media.

$$\begin{array}{ll} f=0,\ \frac{\partial f}{\partial \sigma_{ij}} C_{ijkl}\dot{\varepsilon}_{kl} > 0 & \text{Plastic} \\ f=0,\ \frac{\partial f}{\partial \sigma_{ij}} C_{ijkl}\dot{\varepsilon}_{kl} = 0 & \text{Neutral} \\ f=0,\ \frac{\partial f}{\partial \sigma_{ij}} C_{ijkl}\dot{\varepsilon}_{kl} < 0 & \text{Elastic} \\ f<0 & \text{Elastic} \end{array} \tag{1.3}$$

where C_{ijkl} are the components of the fourth-order elastic tangent stiffness tensor. It is noted that for the neutral case, plasticity theory and elasticity theory will give the same result. Our experimental data for the effect of loading changes will be examined in this very broad context that makes no reference to any particular engineering plasticity model.

Several other assumptions that are common in engineering plasticity will not be adopted in this work. For example, the vast majority of (commonly used) engineering plasticity models presume material isotropy. While isotropy might be a reasonable assumption for the virgin material,

it is not defensible under general deformation even in the elastic regime. Neglect of elastically induced anisotropy generally violates thermodynamics [7], which is a prediction that itself merits experimental investigation to support model revisions for elastically induced anisotropy, or else risk improper parameterization of dissipation in the plastic part of the model to compensate for errors in the elastic part. Of course, induced anisotropy is expected to be even more pronounced under plastic loading, as is well known from the metal rolling industry [8, 9]. Constitutive modelers are forced to assume persistent isotropy for several reasons: (1)lack of data (2) lack of time or resources needed to develop solvable anisotropic governing equations, and (3) lack of computational resources needed to solve the larger, more complicated, set of equations. Additionally, many host codes are not prepared to handle anisotropic constitutive models. Once, for example, we found that the host code's treatment of transmitting (outflow) boundary conditions implicitly assumed material isotropy and was unstable (crashed within two time steps) as soon as a simple transversely isotropic material began to deform at the boundary. Also, the critical timestep built into explicit time integrators is usually based on the assumption that there are only two elastic constants (shear and bulk modulus), which is not correct for anisotropic models.

Our experimental investigation will address the first need by quantifying the extent of both elastic and plastic induced anisotropy. The data will show that the very framework of classical plasticity is incomplete. However, the data analysis will include error-minimizing methods for projecting the observed material response into the framework of classical isotropic engineering plasticity theory. The magnitude of the residual in such an analysis is then a quantitative measure of the approximation error associated with the use of classical engineering plasticity models.

Even experimental work must necessarily introduce assumptions, but those assumptions should be validated in the experiments whenever it is possible to do so. For tractability, our laboratory investigations will involve purely axisymmetric loading, and it will be assumed that the material is initially either isotropic or transversely isotropic so that we may also assume induced anisotropy is, at worst, transversely isotropic. Naturally, redundant gaging is used to assess validity of this assumption during testing. Under general loading, where stress and strain tensors are six-dimensional because they have six independent components, comprehensive validation testing of a classical plasticity theory would require measuring 36 continually evolving tangent stiffness variables, which is well beyond the scope of any laboratory effort to date. Axisymmetric loading, on the other hand, involves two-dimensional representations of stress and strain (each constructing the 6D tensors from two numbers: axial and lateral components), thus reducing the number of tangent stiffnesses to be measured in the laboratory down to only four. Importantly, to quantify the error associated with assumptions in classical engineering plasticity theory, our data reduction allows for the possibility of "incrementally nonlinear response", for which a tangent tensor does not even exist in the classical sense. The definition of incremental nonlinearity, along with the mathematics of the dimensional reduction from 6D to 2D tensors and methods for quantifying error associated with classical plasticity theory are discussed in the next chapter, after which the experimental techniques and results are discussed.

Chapter 2

Terminology and Mathematics

The basic function of a constitutive material model is to quantify evolving relationships between stress (σ), strain (ε), and other variables that characterize the material state. Simple constitutive models characterize the material state by very few variables. For example, an elastic model presumes that the stress tensor depends only the strain tensor:

$$\sigma = \mathscr{F}(\varepsilon) \tag{2.1}$$

Even in this case of elasticity, laboratory data are sometimes erroneously analyzed under an unnecessary assumption of linearity that reduces Eq. (2.1) to

$$\sigma_{ij} = C_{ijkl}\varepsilon_{kl} \tag{2.2}$$

where C_{ijkl} are the components of the fourth-order elastic stiffness tensor. [1] For tractability, data might even be analyzed under the assumption that an elastic model is not only linear, but also that the stiffness is isotropic, making Eq. (2.2) reduce even further to

$$S_{ij} = 2G\gamma_{ij} \qquad \text{and} \qquad p = K\varepsilon_v \tag{2.3}$$

where S_{ij} are the components of the stress deviator, γ_{ij} are the components of the strain deviator, p is the pressure, ε_v is the volumetric strain, K is the bulk modulus, and G is the shear modulus. An aim of the current work is to avoid these and similarly unneeded constitutive assumptions in the analysis of the data.

Of course, for realistic materials, an assumption of linearity of elastic response is not usually adopted. If the function $\mathscr{F}$ in Eq. (2.1) is nonlinear in ε, then its rate form is

$$\dot{\sigma}_{ij} = C_{ijkl}\dot{\varepsilon}_{kl} \tag{2.4}$$

where

$$C_{ijkl} = \frac{\partial \sigma_{ij}}{\partial \varepsilon_{kl}} \tag{2.5}$$

[1] All indices range from 1 to 3, and repeated subscripts indicate summations from 1 to 3.

The fourth-order tensor C_{ijkl} is the local tangent to the nonlinear function relating stress to strain. If the tangent tensor is constant, then this result reduces to the linear form in Eq. 2.2. Otherwise, the tangent stiffness tensor is a function of strain (equivalently, the tangent tensor can be alternatively written as a function of stress if the elastic relationship between stress and strain is invertible to express strain as a function of stress).

An assumption of elasticity (i.e., that stress is a differentiable function of strain) ensures not only the existence of the tangent stiffness, but it also guarantees that the tangent stiffness is *independent of the strain rate* even though it varies with the strain. Stated mathematically,

$$\sigma = \sigma(\varepsilon) \Rightarrow \text{ There exists a tensor } C \text{ such that } \dot{\sigma}_{ij} = C_{ijkl}\dot{\varepsilon}_{kl} \tag{2.6}$$

As is well known from the theory of exact differentials, however, the converse is false. For the converse to be true, the right-hand side of Eq. (2.6) must be supplemented with the additional statement that C depends only on ε (not on $\dot{\varepsilon}$ or anything else) and, moreover, the equation on the right-hand side must be integrable, which requires $dC_{ijkl}/d\varepsilon_{rs} = dC_{ijrs}/d\varepsilon_{kl}$. These additional requirements are extremely difficult to detect from experimental data. Specifically, suppose that it is observed that a fourth-order tensor Y exists such that

$$\dot{\sigma}_{ij} = Y_{ijkl}\dot{\varepsilon}_{kl} \tag{2.7}$$

Does this imply that Y is the same as C in Eq. (2.4)? No, it might be that this tensor Y depends on more than just the strain. Even if Y depends only on strain, Eq. (2.7) might not be integrable for stress as a function of strain. In laboratory work, where only stress and strain increments are measured, it might be possible to find the components of Y, but it is impossible to know with certainty the variables on which Y depends under general loading. Suppose that Y seems to depend on any number of "unknowable other variables," but suppose that it is also known (or assumed) that Y is independent of the strain rate. Then the relationship in Eq. (2.7) is "incrementally linear." On the other hand, if the Y tensor might possibly depend on the strain rate itself, then the relationship between stress and strain (and any number of other state variables) is "incrementally nonlinear." In the simpler case of a scalar (one-dimensional) stress-strain relationship, incremental nonlinearity simply implies that the local slope is discontinuous so that one slope applies to loading ($\dot{\varepsilon} > 0$) and a different slope applies to unloading ($\dot{\varepsilon} < 0$). Whereas in the one-dimensional case, there are only two possible loading directions (forward or backward), in the two or three-dimensional case there are an infinite number of possible loading directions.

A goal of this project is to minimize constitutive assumptions in data analysis in order to assess validity of constitutive assumptions commonly made in engineering plasticity theories. Specifically, in plasticity theory the stress rate is presumed to be expressible in the form

$$\dot{\sigma}_{ij} = \begin{cases} C_{ijkl}\dot{\varepsilon}_{kl} & \text{during elastic loading} \\ T_{ijkl}\dot{\varepsilon}_{kl} & \text{during plastic loading} \end{cases} \tag{2.8}$$

where C is called the elastic tangent stiffness, and T is the plastic tangent stiffness. This statement of the basic structure of plasticity equations can be written in the form of Eq. (2.7) by taking

$$Y_{ijkl} = \begin{cases} C_{ijkl} & \text{during} \quad \text{elastic loading} \\ T_{ijkl} & \text{during} \quad \text{plastic loading} \end{cases} \tag{2.9}$$

In classical rate-independent plasticity, neither C nor T depends on the strain rate, but as discussed above the determination of whether or not loading is elastic or plastic does depend on the strain rate according to Eq. (1.3). Therefore, even classical plasticity is incrementally nonlinear in the strictest sense. However, classical plasticity theory is generally nevertheless referred to as incrementally linear because it is *piecewise* incrementally linear.

The laboratory investigations for this research seek to determine whether or not even the most basic form of classical plasticity (piecewise incremental linearity) is a valid approximation. To be consistent with an assumption of rate independence, the experimental investigations are limited to very slow loading rates with hold periods between elastic unloading cycles. (Even with hold periods, some creep is recognized in the upcoming data, but means for quantifying the error of an assumption of rate independence in classical plasticity theory will not be addressed in this work.)

Regular Flow Rule

The vast majority of engineering plasticity models not only assume that the strain rate can be decomposed into elastic and plastic parts,

$$\dot{\varepsilon} = \dot{\varepsilon^e} + \dot{\varepsilon^p}, \tag{2.10}$$

but they also invariably adopt a *"regular flow rule"*, which presumes that only the *magnitude* of the plastic strain rate $\dot{\varepsilon^p}$ depends on the total strain rate $\dot{\varepsilon}$, whereas the *direction* of the plastic strain rate is determined purely from the material state, not from the rate of change of state.

The direction of a tensor A is defined by a tensor of unit magnitude $\hat{A}$ just as with a vector:

$$\hat{A}_{ij} = \frac{A_{ij}}{\sqrt{A_{mn}A_{mn}}} \tag{2.11}$$

where the term in the denominator is the magnitude of the tensor A. Of course, any tensor can be decomposed multiplicatively into its magnitude times a unit tensor in its direction. When applied to the plastic strain rate, this decomposition is

$$\dot{\varepsilon}^p_{ij} = \dot{\lambda} M_{ij} \qquad \text{where} \qquad \dot{\lambda} = \sqrt{\dot{\varepsilon}^p_{ij}\dot{\varepsilon}^p_{ij}} \qquad M_{ij} = \dot{\varepsilon}^p_{ij}/\dot{\lambda} \tag{2.12}$$

An ability to express the plastic strain rate in this form does not imply a regular flow rule. To be a regular flow rule, the tensor M must be independent of the total strain rate. A regular flow rule states that the direction of the plastic strain rate tensor $\dot{\varepsilon}^p$ is independent of the direction of the total strain rate $\dot{\varepsilon}$. If in addition to a regular flow rule, it is also assumed that material response is rate independent, then it can be shown that equation (1.1) becomes linear in $\dot{\varepsilon}$. Namely,

$$\mathscr{H}(\dot{\varepsilon}, \sigma, \eta_1, \eta_2, ...) = T_{ijkl}(\sigma, \eta_1, \eta_2 ...)\dot{\varepsilon}_{kl} \tag{2.13}$$

where T_{ijkl} is the fourth-order *plastic* tangent stiffness tensor. When written without explicitly showing dependencies, this becomes simply

$$\dot{\sigma}_{ij} = T_{ijkl}\dot{\varepsilon}_{kl} \tag{2.14}$$

Just as with the elasticity equations, such a formulation greatly simplifies the implementation of the material model as compared to equation (1.1) because it leads to a linear system which is solvable for increments in all variables. Each variable is then integrated through time to update the material state at each time step. Although most plasticity models rely on this assumption, very little work has been done to assess its validity.

Dimensional reduction for axisymmetric loading

As mentioned in the introduction, the scope of our laboratory investigation is limited to axisymmetic loading of a material that is, at most, transversely isotropic. Then it may be reasonably presumed (and verified through redundant gaging) that any second-order tensor in the analysis may be written in the form

$$[A] = \begin{bmatrix} A_A & 0 & 0 \\ 0 & A_L & 0 \\ 0 & 0 & A_L \end{bmatrix} \tag{2.15}$$

where the subscripts "A" and "L" refer to axial and lateral components. This may be written as a linear combination of *unit* base tensors as

$$\begin{bmatrix} A_A & 0 & 0 \\ 0 & A_L & 0 \\ 0 & 0 & A_L \end{bmatrix} = (A_A) \begin{bmatrix} 1 & 0 & 0 \\ 0 & 0 & 0 \\ 0 & 0 & 0 \end{bmatrix} + \left(\sqrt{2}A_L\right) \frac{1}{\sqrt{2}} \begin{bmatrix} 0 & 0 & 0 \\ 0 & 1 & 0 \\ 0 & 0 & 1 \end{bmatrix} \tag{2.16}$$

The normalization of the base tensors allows reducing the generally 6-dimensional entity (a fully-populated symmetric tensor [A]) to a simple two-dimensional vector having components A_A and $\sqrt{2}A_L$. The introduction of the $\sqrt{2}$ ensures that the ordinary magnitude of the *vector*,

$$\begin{bmatrix} A_L \\ \sqrt{2}A_L \end{bmatrix}, \tag{2.17}$$

is the same as the magnitude of the tensor. For this reason, the two values (A_A and $\sqrt{2}A_L$) are said to be isomorphic to stress space. They are Euclidean coordinates within a two-dimensional plane that "cuts through" six-dimensional tensor space. With this reduction in dimension, Eq. (2.14) then reduces to simply

$$\begin{bmatrix} \dot{\sigma}_A \\ \dot{\sigma}_L \end{bmatrix} = \begin{bmatrix} T_{AA} & T_{AL} \\ T_{LA} & T_{LL} \end{bmatrix} \begin{bmatrix} \dot{\varepsilon}_A \\ \dot{\varepsilon}_L \end{bmatrix} \tag{2.18}$$

Whereas the above decomposition into axial and lateral components is most natural for the laboratory control, data analysis that aims to draw connections with conventional plasticity theories is better served by introducing a change of variables. For any axisymmetric tensor [A] defined by its isomorphic components (A_A and $\sqrt{2}A_L$), an alternative pair of isomorphic components, corresponding to an orthogonal basis rotation in the same two-dimensional space, is given by

$$\begin{bmatrix} A_z \\ A_r \end{bmatrix} = \frac{1}{\sqrt{3}} \begin{bmatrix} 1 & \sqrt{2} \\ \sqrt{2} & 1 \end{bmatrix} \begin{bmatrix} A_A \\ \sqrt{2}A_L \end{bmatrix} \tag{2.19}$$

With this change of variables, Eq. (2.16) can be written as an equivalent expansion in terms of a different pair of unit base tensors as

$$\begin{bmatrix} A_A & 0 & 0 \\ 0 & A_L & 0 \\ 0 & 0 & A_L \end{bmatrix} = (A_z) \frac{1}{\sqrt{3}} \begin{bmatrix} 1 & 0 & 0 \\ 0 & 1 & 0 \\ 0 & 0 & 1 \end{bmatrix} + (A_r) \frac{1}{\sqrt{6}} \begin{bmatrix} 2 & 0 & 0 \\ 0 & -1 & 0 \\ 0 & 0 & -1 \end{bmatrix} \tag{2.20}$$

which illustrates that these two alternative coordinates decompose axisymmetric tensors into their isotropic and deviatoric parts.

These alternative axisymmetric measures are subscripted "*r*" and "*z*" because they can be shown to correspond to the cylindrical coordinates that are naturally implied in the symmetries of Fig. 1.2. For axisymmetric loading the angular coordinate, called the Lode angle, is fixed on the compressive meridian. Therefore, because *z*-*r* Lode coordinates are isomorphic to stress space, our upcoming plots in *z*-*r* stress space are *geometrically* accurate (same lengths and angles) depictions of a "side view" of the yield surfaces in Fig. 1.2. It is this feature, as well as inheritance of tensor properties, such as symmetries and eigensystems of the tangent tensor, that recommends isomorphic tensor measures over perhaps more (initially) intuitive or familiar coordinate pairs. The Lode axial coordinate σ_z is the hydrostatic component of the stress, and it is related to pressure p by $\sigma_z = \sqrt{3}p$. The Lode radius σ_r is a measure of equivalent shear stress, and it is related to the conventional measure of shear stress, q, by $\sigma_r = q\sqrt{3/2}$. Thus, not only may a plot of σ_r vs. σ_z be regarded as a "side view" of an isotropic yield surface, such a plot may be also seen as loosely depicting shear strength vs. pressure, with the only difference being constant scaling of the axes. The Lode coordinates represent decomposition of the tensor into isotropic and deviatoric parts,

which reveals structure in simple idealized solid mechanics theories. For example, with the Lode measures for axisymmetric problems, the isotropic Hooke's Law of Eq. (2.3) becomes simply

$$\begin{bmatrix} \dot{\sigma}_z \\ \dot{\sigma}_r \end{bmatrix} = \begin{bmatrix} 3K & 0 \\ 0 & 2G \end{bmatrix} \begin{bmatrix} \dot{\varepsilon}_z \\ \dot{\varepsilon}_r \end{bmatrix} \tag{2.21}$$

Of course, the general form for incremental plasticity becomes

$$\begin{bmatrix} \dot{\sigma}_z \\ \dot{\sigma}_r \end{bmatrix} = \begin{bmatrix} T_{zz} & T_{zr} \\ T_{rz} & T_{rr} \end{bmatrix} \begin{bmatrix} \dot{\varepsilon}_z \\ \dot{\varepsilon}_r \end{bmatrix} \tag{2.22}$$

For simplicity, we may write this in a more compact notation as simply $\dot{\sigma} = T\dot{\varepsilon}$, where it must be understood from context that $\dot{\sigma}$ and $\dot{\varepsilon}$ are 2x1 vectors, while T is a 2x2 matrix.

Our analysis of laboratory data will *not* presume that a classical (incrementally linear) plastic tangent stiffness tensor even exists. Suppose that incremental nonlinearity is observed in the data, but only incrementally linear plasticity models are available in our finite element codes. Then a short-term workaround is needed while awaiting model enhancements to be delivered by the constitutive modelers, which could take many years since there are few validated models for incremental nonlinearity. A *rational* strategy for interim use of existing classical plasticity models would set the incrementally linear parameters to values that minimize error with observed incrementally nonlinear data. In analogous problems involving scalars (instead of tensors), the rational approach is to use a least squares fit to nonlinear data until a nonlinear model is available. In our more general case for which the data consists of a collection of stimulus *vectors* and their corresponding response *vectors*, an unweighted least squares best linear fit to the data is obtained as follows: (1)place the stimulus vectors into columns of a matrix $[S]$, (2)place the corresponding response vectors into columns of a matrix $[R]$, and (3)evaluate the best fit linear transformation matrix $[L] = [R][S]^{(-1)}$, where the superscript "(-1)" denotes the pseudo-inverse (available in most numerical linear algebra packages, and required in data analysis because $[S]$ is generally non-square). The pseudoinverse is an ordinary inverse if there are exactly the same number of linearly independent stimulus vectors as the dimension of the space. The residual error of the approximation is quantified by the norm of $[R] - [L][S]$. Of course, a *weighted* linear regression may be used if greater accuracy for particular loading directions is desired. Incidentally, the experiments described in this report are all stress controlled. Therefore, the "stimulus" matrix $[S]$ holds the stress increment vectors, and the "response" matrix $[R]$ holds the measured strain increment vectors (interpolated to the current material state, as described later). Therefore, the $[L]$ matrix computed in our data analysis is actually the tangent *compliance*, $[L] = [T]^{-1}$.

Visualization of linear transformations

As mentioned in the previous section, analysis of out laboratory experiments will make no assumptions that the material is incrementally linear or even isotropic. We will simply plot the strain

increment (response) vectors resulting from stress increment (stimulus) vectors that are in various directions, but each of equal length. Because the stimulus vectors are all of equal length, plotting them joined at the tails produces a set of vectors whose tips form a circle, as illustrated in Fig. 2.1. Doing the same type of tail-to-tail plot for the response vectors allows direct visualization of the degree to which the transformation from stress increments to strain increments is linear. A necessary condition for a transformation to be linear is that the response envelope must form an ellipse, as in 2.1(b). This is not a sufficient condition, as seen in Fig. 2.1(d); a linear transform has the appearance of a uniform stretching of the stimulus disk, possibly in combination with some rotation. An example of a more "ordinary" nonlinear transformation is shown in Fig. 2.1(c).

Incidentally, the plots in Fig. 2.1 are superior to Reynolds glyphs [10] because a Reynolds glyph fails to convey information about rotation and, as mentioned, it does not depict irregular vector distributions on the ellipse (or ellipsoid in 3D). Reynolds glyphs for stress-strain transformations are often referred to as "Gudehus" diagrams [11].

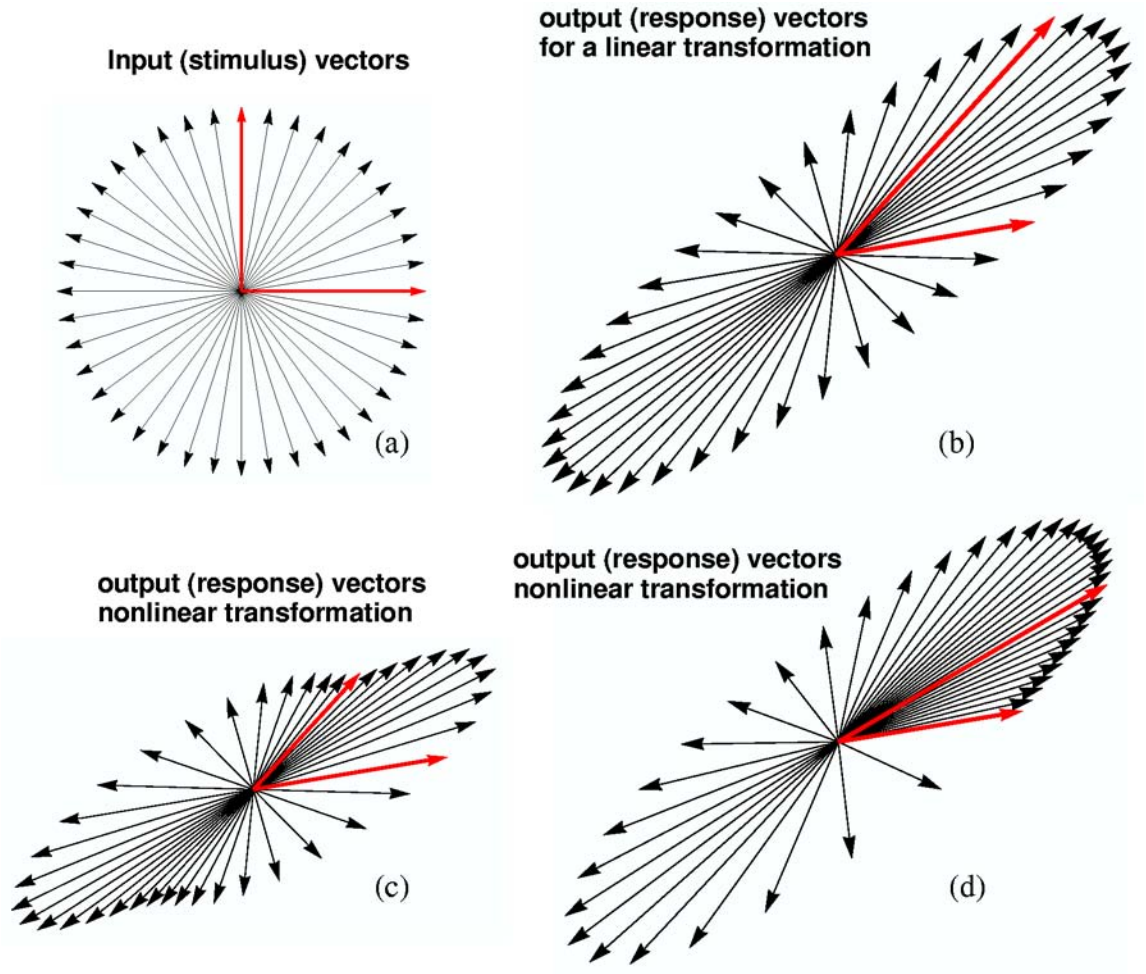


Figure 2.1. Visualization of vector transformations.

Data interpolation to a single state

For stress-controlled axisymmetric loading, inferring an incremental relationship between stress and strain requires a *minimum* of two stress (stimulus) increments and the corresponding measured strain (response) increments. Far more than two stimulus (stress increment) directions are required to detect incremental nonlinearity. Importantly, the relationship between stress and strain increments is a *material state function* – it represents how the material would respond to any given stimulus *at the current state*. However, this state function is also an *evolving* state function, which means the act of measuring material response to any one stimulus will generally irreversibly change the material, making it impossible to know with certainty how the material *would* have responded to some other stimulus. Let it be emphasized that identical material states mean identical materials, under identical stress states, and identical loading histories. In practice such a measurement is impossible because the act of inelastically deforming the material to measure the response for the first stimulus irreversibly changes the material, making it impossible to know with certainty what the material response *would have been* if the material had been instead loaded in a different direction. To answer that question, one would have to be able to manufacture an *identical* sample and load it through an *identical* path under *identical* ambient conditions in order to measure the response to any new stimulus. Obviously, attaining identical conditions for a second measurement is impossible from a practical standpoint as well because of variability in samples and loading procedures.

Two methods have been used to overcome these difficulties. The most common method used to assess the validity of a regular flow rule is through the use of discrete element method (DEM) simulations or other computational schemes. The advantage of this method is that it is a simple matter to create identical material states in a computer simulation. Several simulations may be performed with the same initial conditions and different loading directions. One such study by Tamagnini [12] compared such "stress probe" DEM simulations with various constitutive models. These simulations were meant to model a soil specimen. The "specimen" geometry used was a cube of material whose faces were aligned with the principal stress/strain directions. These simulations were performed by loading the material through a prescribed axisymmetric loading path as shown in Fig. (2.2). The loading path consisted of hydrostatic compression to 100 kPa, then triaxial compression until the deviatoric stress reached 300 kPa, then unloading along the same path until the deviatoric stress was 100 kPa. Two points along the path were selected as reference states for stress probing. The first point B was on the triaxial loading path when the deviatoric stress was 100 kPa. The second point B' was at the same stress state, only on the unloading portion of the path.

Beginning at these two reference states, small stress increments (probes) were applied in several directions. For each loading direction the simulation was performed once with energy dissipation mechanisms active, and once with no energy dissipation allowed. The particle displacements with the energy dissipation mechanisms active were used to calculate the total strain increment, while the displacements that occurred when no energy dissipation was allowed were used to calculate the elastic strain increments. The stress probe directions were constrained to the axisymmetric plane ($\dot{\sigma}_x = \dot{\sigma}_y$) and the deviatoric plane ($\dot{\sigma}_x + \dot{\sigma}_y + \dot{\sigma}_z = 0$). Stated differently, the first set of tests, like ours, held the Lode angle constant. Unlike ours, the second set of tests held the pressure (or,

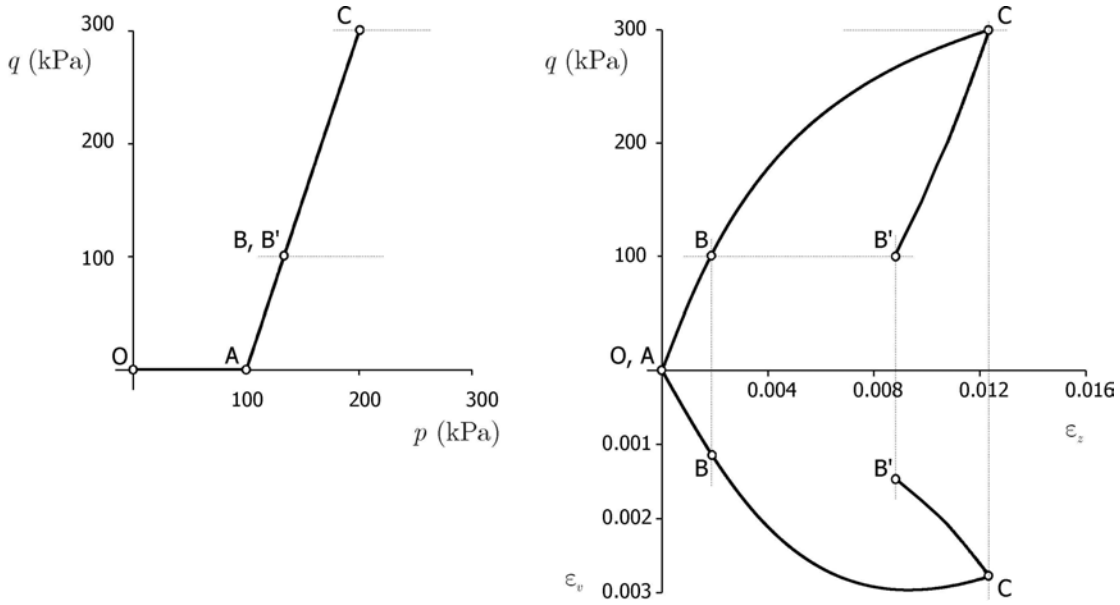


Figure 2.2. Triaxial compression load path used in DEM simulations performed by Tamagnini. Here q is the equivalent shear stress, and p is the mean stress. Also ε_z is the strain in the z(axial)-direction, and ε_v is the volumetric strain. The points at which stress probes were applied are labeled B and B'. (Courtesy of C. Tamagnini)

equivalently, the z Lode coordinate) fixed, which corresponds to an octahedral plane orthogonal to the meridional plane used in the first set of tests.

The results of this study are displayed using incremental strain response envelopes. These envelopes represent the unit circle in stress space (as in Fig. (2.3)) mapped to strain space. They provide a convenient way of visualizing material response. Figure (2.3) illustrates the response in the axisymmetric plane while at the virgin state that is labeled B in Fig. (2.2). Notice that the plastic strain response envelope is a single line. This means that the direction of plastic strain is independent of loading direction, indicating a regular flow rule. In other words no matter what stress increment is applied, the direction of $\dot{\varepsilon}^p$ is fixed (only its magnitude depends on the stress increment). Applying the same stress probes at the state B' on the unloading leg produced the strain response envelope shown in Fig. (2.4). This strain envelope looks much like the one from virgin state B, except that plastic strain increments were observed in the unloading directions as well as loading directions. Classical plasticity theory would predict an entirely elastic response at this point since it lies within the now expanded yield surface. Aside from this disagreement with classical plasticity theory, these probes seem to suggest that a regular flow rule is in fact a valid assumption. However, the results from the stress probes in the deviatoric plane are quite different. Figure (2.5) illustrates the strain response envelope at virgin state B for stress probes in the deviatoric plane.

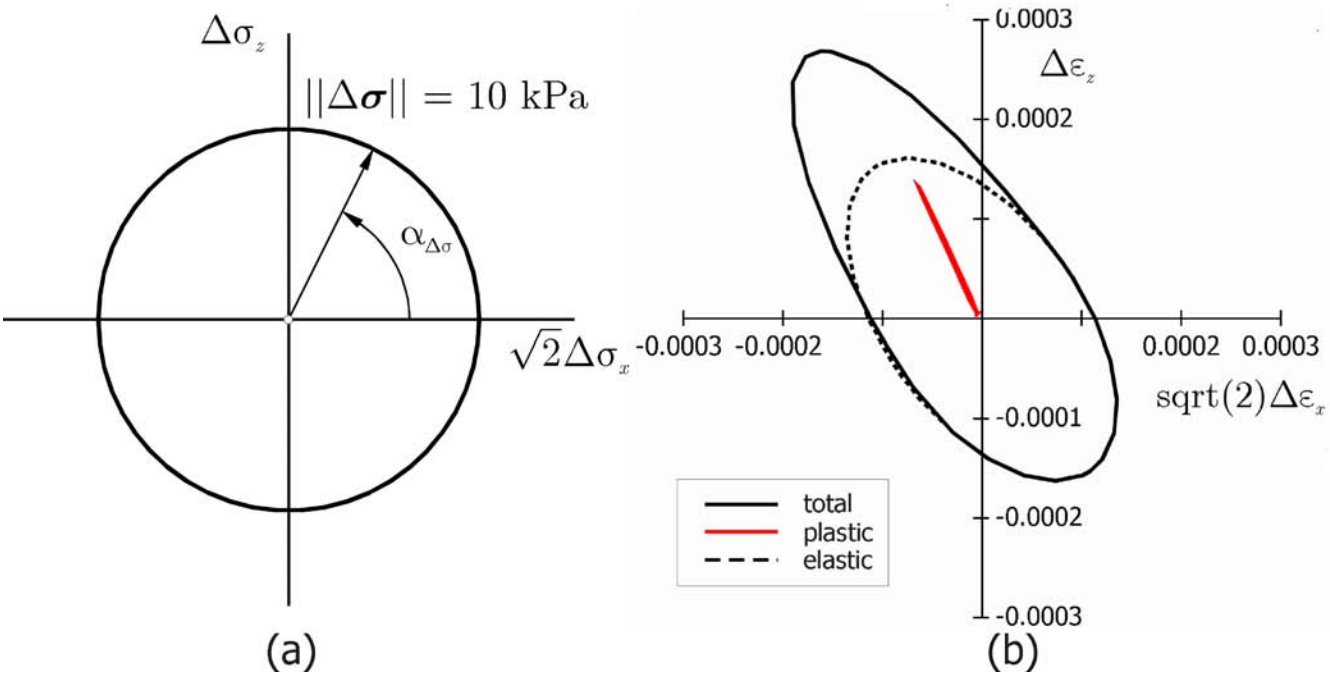


Figure 2.3. Results of Tamagnini's DEM stress probe simulations. A set of axisymmetric stress increments represented by a unit circle in stress space (left), and the resulting strain increments mapped to strain space (right).

The strain response envelope at material state B' was similar to that at state B. The strain response envelope shows that the direction of plastic strain has a strong dependence on the loading direction. This indicates an irregular flow rule. Other studies [13, 14] have had similar results. The major drawback to these DEM simulations is that the simulations themselves rely on many unvalidated assumptions.

Another method that has been used to study the validity of a regular flow rule is to perform stress probing experiments in the laboratory. One such study [15] fabricated a set of nominally identical samples composed of sand. Just as with the DEM study, each sample was loaded though a specified axisymmetric loading path to a particular point in stress space. After reaching the desired stress state, a small stress increment was applied, then reversed. The strain that remained after the unloading was assumed to be the plastic strain increment. This process was repeated with stress increments in a variety of directions, using a different sample each time. Since these tests were performed in a triaxial compression fixture, all loading increments were constrained to the axisymmetric meridian. For stress states near failure, a regular flow rule was observed. However, for stress states near the hydrostat, the direction of the plastic strain increment depended strongly on the loading direction. The author was quick to point out that because of the small strain increments for probes near the hydrostat the experimental error was also greater in this region.

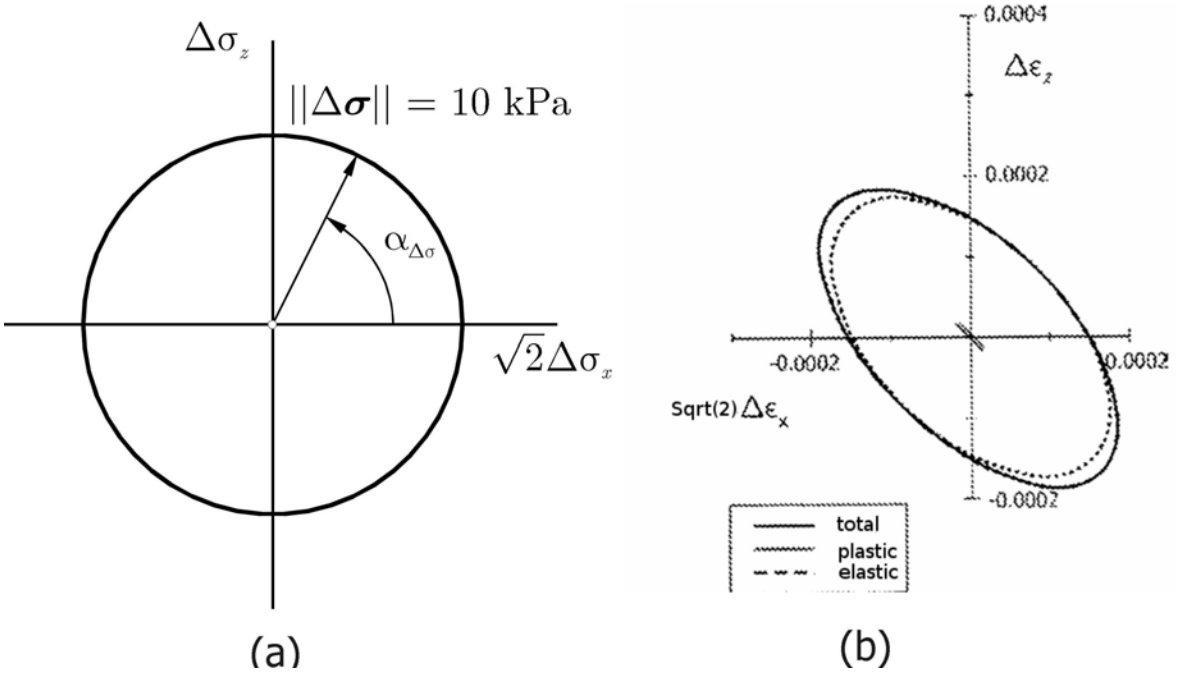


Figure 2.4. Strain response envelope for axisymmetric stress probes at stress state B' from Tamagnini's DEM simulations. (Courtesy of C. Tamagnini)

Another study by Royis [16] had similar findings. While this type of testing has yielded some very interesting and valuable results, the results depend on the fabrication of "identical" samples. The methods they used were specific to soil specimens, and could not easily be extended to other engineering materials.

These previous studies cast some doubt on the validity of a regular flow rule. Below, we propose an alternative method for studying the validity of a regular flow rule which may be more straightforward than the methods discussed above. The proposed new approach is premised on certain interpolation assumptions that will rely on these previous studies for validation. After discussing additional assumptions, the details of this method will be explained.

Non-Associated Flow Rule

Accepting the assumption of a regular flow rule requires the direction of the plastic strain rate to be defined for all states of stress where inelastic deformation is possible. Here we will assume that the yield function is differentiable, and therefore the yield surface has no vertices. This assumption is adopted not because it is necessarily true, but because the goal of this study is to determine whether or not models that make this assumption are capable of being fit to the data.

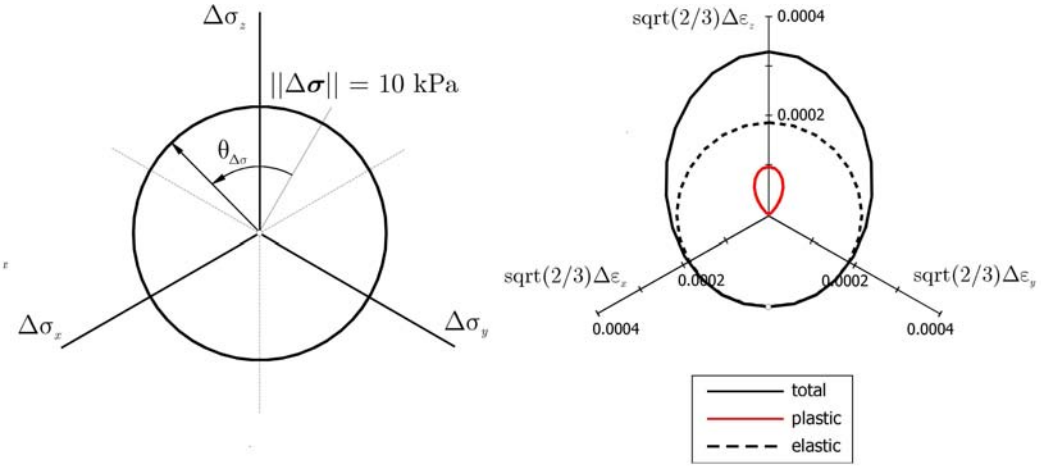


Figure 2.5. Results of Tamagnini's DEM stress probe simulations. A set of deviatoric stress increments represented by a unit circle in stress space (left), and the resulting strain increments mapped to strain space (right). (Courtesy of C. Tamagnini)

Drucker [17, 18] investigated the requirements that stability placed upon the direction of the plastic strain rate. The analysis begins with a unit volume of material in which there is a homogeneous state of stress and strain. An external agency then applies a stress increment which loads the material in such a way that the stress state lies on the yield surface. The external agency then applies a small stress increment directed outward from the yield surface. The external agency then releases the small stress increment, and returns the stress state to the initial state. Drucker asserted that stability requires that positive work be done by the external agency during the application of the stress increments, and that the net work performed by the external agency over the cycle of application and removal of the stress increments be zero or positive. With these two requirements it can be shown that the plastic strain rate must be normal to the yield surface. The resulting flow rule is called an associated flow rule and is given by:

$$\dot{\varepsilon^p} = \dot{\lambda} \frac{\dfrac{\partial f}{\partial \sigma}}{\left\| \dfrac{\partial f}{\partial \sigma} \right\|} \tag{2.23}$$

where $\dot{\lambda}$ is the magnitude of the plastic strain rate. For materials whose yield strength has a strong dependence on hydrostatic pressure, the normal to the yield surface will have a significant dilatational component. It has been widely reported that for such materials, an associated flow rule over predicts plastic dilatation [19, 20, 14]. To remedy this problem, a non-associated flow rule is often employed. This type of flow rule uses a separate flow potential function g to define the

plastic strain rate direction:

$$\dot{\varepsilon}^p = \dot{\lambda} \frac{\dfrac{\partial g}{\partial \sigma}}{\left\| \dfrac{\partial g}{\partial \sigma} \right\|} \tag{2.24}$$

Non-associated flow rules appear to better predict plastic dilatation under monotonic loading. However, as indicated by Drucker, models based on such a flow rule suffer from instability for certain boundary value problems [17, 21, 22, 23, 24]. An additional potentially problematic aspect of (2.24) is that, unlike (2.23) which is evaluated only when $f = 0$ and therefore giving the normal to the yield surface, equation (2.24) is typically evaluated at stress states for which $g \neq 0$ and therefore there is no corresponding notion of a flow surface.

Sandler and Rubin [21] built upon Drucker's work by demonstrating a connection between Drucker's instability and non-uniqueness in applications of rate independent plasticity to dynamic problems. Sandler and Rubin concluded with a recommendation that rate dependence is essential to preventing the unstable or non-unique results. Like Drucker, Sandler and Rubin premised their analysis on the assumption of a regular flow rule. Later Pučik [23] confirmed Sandler and Rubin's analytical solution and demonstrated similar results with a finite element and analytical case study. The example problem consisted of a semi-infinite medium with an initial stress state lying on a Drucker-Prager yield surface, with a non-associated flow rule as illustrated in Fig. (2.6).

A small disturbance is applied which causes a wave to propagate through the material. The disturbance was chosen so that the trial stress increment has a positive inner product with the yield normal, but a negative inner product with the flow potential normal as illustrated in Fig. (2.7). The region of stress space that has this property is known as the Sandler-Rubin wedge.

It was shown that with this disturbance, the plastic wave speed is faster than the elastic wave speed. The fact that classical non-associative plasticity allows certain plastic waves to travel faster than elastic waves has also been independently confirmed by Brannon [25], who showed that every ordering of plastic wave speeds relative to elastic wave speeds is possible, depending on the details of the nonassociativity. Moreover, Brannon showed that there are only two classes of non-associativity (marked regions A and F in Fig. 2 of [25]) for which the plastic wave speeds are ensured to be always slower than the elastic longitudinal wave speed. In short, this possibility of plastic waves moving faster than elastic waves is not limited to the idealization of Drucker-Prager models; any nonassociative model admits this possibility. This causes the loading and unloading ramps to separate and the pulse width to increase with time. Also the region between the two ramps, which initially consists of a single point, opens up into a finite region. There exists a two-parameter family of non-unique solutions in this region. Figure (2.8) illustrates possible analytical solutions to this problem as found by Sandler, Rubin and Pučik.

As shown in Fig. (2.8) there are solutions for which the wave amplitude grows with time. In the limit of small disturbances, this implies spontaneous motion from a quiescent state, clearly a troubling possibility. Pučik also explored this non-uniqueness and instability in the context of

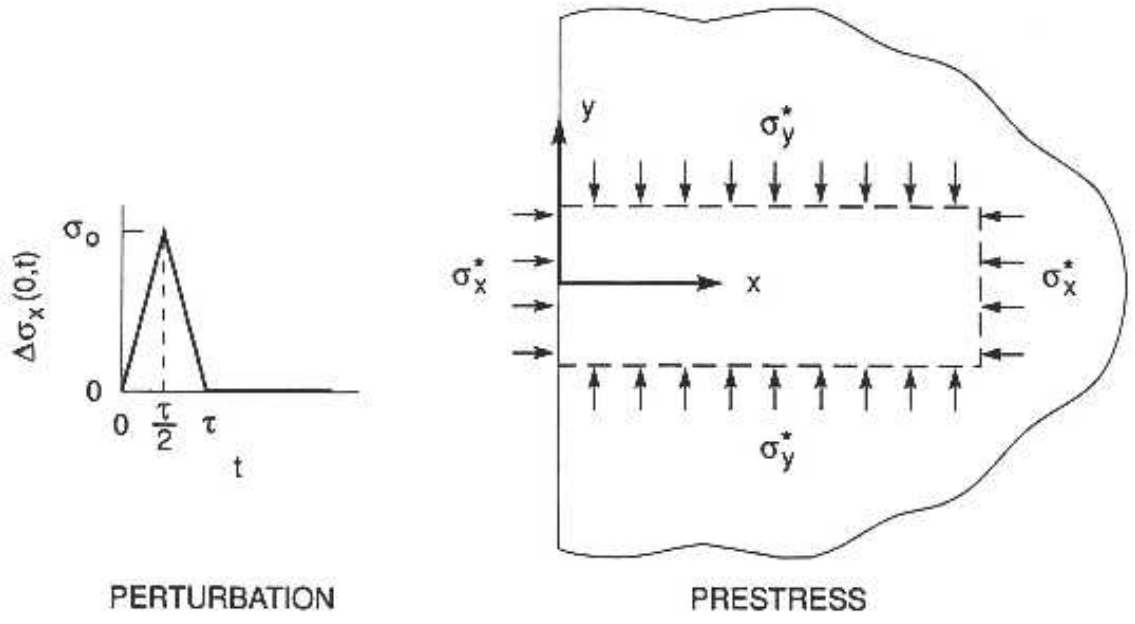


Figure 2.6. Semi-infinite solid with initial stress state placing it on the Ducker-Prager yield surface. The perturbation is designed such that it loads the material into the Sandler-Rubin wedge. (Figure from unpublished work of T.A. Pučik [23])

finite-element simulations. Pučik discovered that the non-uniqueness and instability may show up in a finite-element simulation, but they are often difficult to discern in a complex problem since the instabilities appear to grow linearly with time rather than exponentially. The non-uniqueness was demonstrated by slightly varying the initial positions of the nodes. Changing the initial positions by a distance on the order of the round-off error created dramatic changes in the numerical solution. Some of these solutions are shown in Fig. (2.9).

Effect of Triaxial Compression on Hydrostatic Limit

An additional assumption that is investigated involves the effect of triaxial compression loading on the hydrostatic yield limit for porous materials. As mentioned in the introduction the yield function is permitted to depend upon the loading history. This occurs through hardening (or softening, which we regard as negative hardening). Engineering models for hardening usually support either kinematic or isotropic hardening. Kinematic hardening involves the translation of the yield surface in stress space, whereas isotropic hardening involves the expansion of the yield surface. This report will focus on some assumptions regarding how the yield surface expands through isotropic hardening that is usually attributed to pore collapse.

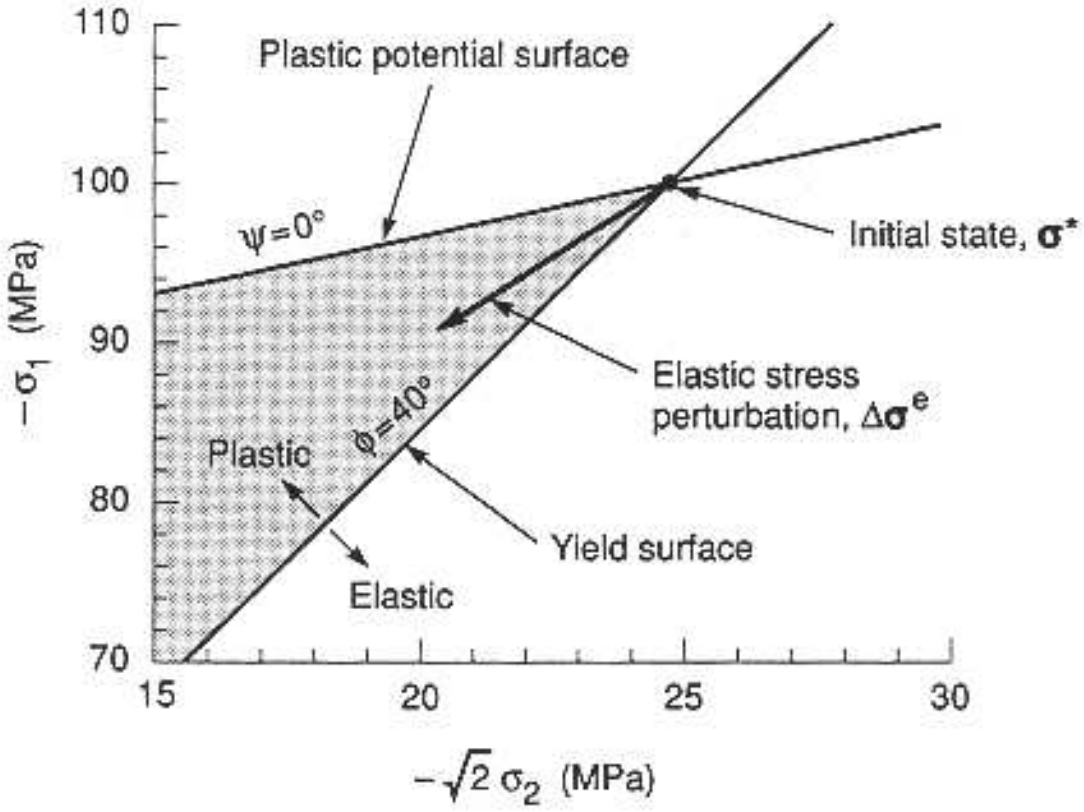


Figure 2.7. The yield surface and plastic potential with the Sandler-Rubin wedge illustrated. (Figure from unpublished work of T.A. Pučik [23])

Porous materials may undergo inelastic deformation (pore collapse) due to purely hydrostatic loading. For this reason the yield surface for these materials must have a “cap” on the hydrostatic axis. These materials also typically exhibit considerable hardening, which is often assumed to be isotropic in nature. In some models, this causes the “cap” to expand outward as a material undergoes shear loading, effectively increasing the yield strength of the material in hydrostatic compression. In this study we seek to asses the validity of existing models which predict this increase in hydrostatic yield strength due to shear loading.

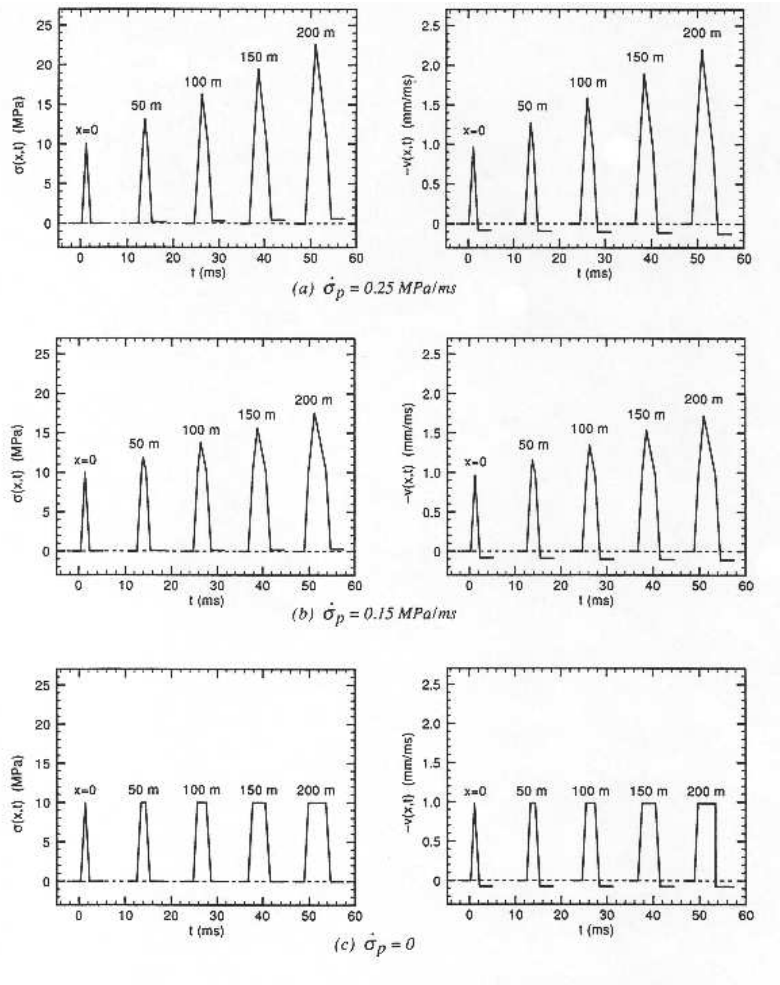


Figure 2.8. Possible analytical solutions to the example problem of Fig. 2.6 (derived by Pučik [23]). Pučik's analytical solution resulted in a family of solutions with two free parameters (v_p and $\dot{\sigma}_p$). Each set of plots represents a different choice for the free parameter $\dot{\sigma}_p$, as labeled. The plots on the left show a propagating triangular stress pulse, while the plots on the right show the corresponding velocity profiles.

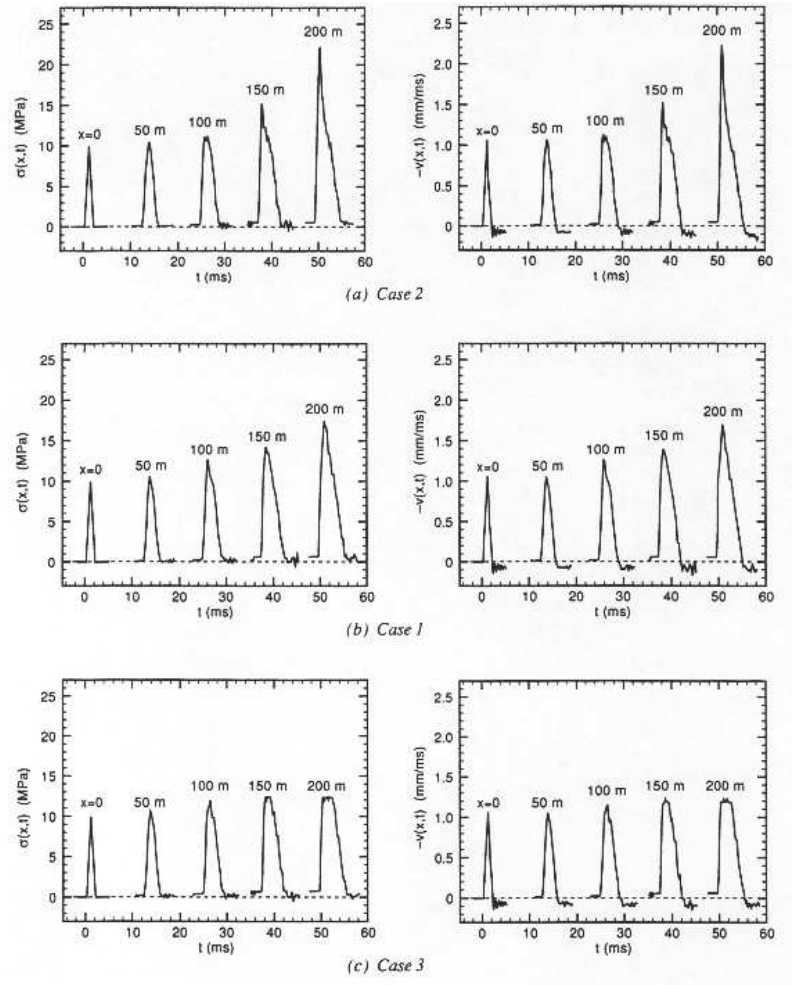


Figure 2.9. Some finite-element solutions to the Pučik wave-propagation problem. (Simulations performed by Pučik [23]) The plots on the left represent stress profiles of the shock wave, while the plots on the right represent the velocity profiles of the shock wave. Each plot shows the profile of the wave at various distances into the material. Each case was performed with the exact same material properties and boundary conditions. The only different was a slight change of the initial positions of the nodes (on the order of round-off error).

Chapter 3

Axisymmetric Plasticity

The validation method presented in this paper analyzes axisymmetric test data in the framework of classical plasticity theory. The first step in presenting this method will be to simplify the governing equations of classical plasticity theory for the axisymmetric case. For the general case, the plastic tangent stiffness tensor T_{ijkl} may be written in terms of the elastic tangent stiffness tensor E_{ijkl}, the yield and flow potential functions f and g, and the ensemble hardening modulus H as [26]:

$$T_{ijkl} = E_{ijkl} - \frac{1}{\eta} P_{ij} Q_{kl} \tag{3.1}$$

$$P_{ij} = E_{ijkl} M_{kl} \tag{3.2}$$

$$Q_{kl} = E_{klop} N_{op} \tag{3.3}$$

$$M_{kl} = \frac{\frac{\partial g}{\partial \sigma_{kl}}}{\sqrt{\frac{\partial g}{\partial \sigma_{vw}} \frac{\partial g}{\partial \sigma_{vw}}}} \tag{3.4}$$

$$N_{kl} = \frac{\frac{\partial f}{\partial \sigma_{kl}}}{\sqrt{\frac{\partial f}{\partial \sigma_{vw}} \frac{\partial f}{\partial \sigma_{vw}}}} \tag{3.5}$$

$$\eta = P_{ij} N_{ij} + H \tag{3.6}$$

Yield functions for most materials have some degree of symmetry about the hydrostatic [111] axis. Because of this symmetry, it is often more convenient to express plasticity equations in terms of a coordinate system aligned with the hydrostat. In this report we will make use of “Lode” coordinates which represent a cylindrical coordinate system with the z-axis aligned with the hydrostat.

The unique feature of this coordinate system is that it is isomorphic to principal stress space, meaning that angles and lengths are preserved when transforming from principal stress space to Lode coordinate space. This allows geometrically accurate plots of the yield surface and incremental vectors to be constructed in a lower dimensional space. The Lode coordinates may be found from the Cauchy stress tensor using the following equations [26]:

$$\begin{aligned} \sigma_z &= \frac{1}{\sqrt{3}} tr\sigma \\ \sigma_r &= \|S\| \end{aligned} \tag{3.7}$$

where S is the stress deviator, and $\hat{S}$ is a unit tensor in the direction of the stress deviator.

Just as with a traditional cylindrical coordinate system, we also define base "vectors" (in this case, second order tensors) associated with each coordinate in equation (3.7) [26]:

$$\begin{aligned} E_z &= \frac{I}{\|I\|} = \frac{I}{\sqrt{3}} \\ E_r &= \hat{S} \end{aligned} \tag{3.8}$$

where $\hat{S}$ is a unit tensor in the direction of the stress deviator S, and I is the identity tensor. Using these coordinates under axisymmetric loading, the Cauchy stress tensor may be decomposed as follows:

$$\sigma = \sigma_r E_r + \sigma_z E_z \tag{3.9}$$

If the material is assumed to be either isotropic or transversely isotropic, the strain tensor may also be decomposed in the same manner by substituting the strain tensor for the Cauchy stress tensor in equation (3.7):

$$\varepsilon = \varepsilon_r E_r + \varepsilon_z E_z \tag{3.10}$$

Using these relations, it can be shown that for isotropic materials under axisymmetric loading, Hooke's law can be written in matrix notation as:

$$\begin{bmatrix} \dot{\sigma}_r \\ \dot{\sigma}_z \end{bmatrix} = \begin{bmatrix} 2G & 0 \\ 0 & 3K \end{bmatrix} \begin{bmatrix} \dot{\varepsilon}_r \\ \dot{\varepsilon}_z \end{bmatrix} \tag{3.11}$$

where G is the tangent shear modulus and K is the tangent bulk modulus. The 2×2 matrix above is a representation of the elastic tangent stiffness tensor used in equation (3.1). Under the same conditions, the plastic tangent stiffness in (3.1) may also be simplified into a 2×2 matrix as follows:

$$T = E - \frac{1}{\eta} P \otimes Q \tag{3.12}$$

where,

$$\begin{bmatrix} P_r \\ P_z \end{bmatrix} = \begin{bmatrix} 2G & 0 \\ 0 & 3K \end{bmatrix} \begin{bmatrix} M_r \\ M_z \end{bmatrix} \tag{3.13}$$

$$\begin{bmatrix} Q_r \\ Q_z \end{bmatrix} = \begin{bmatrix} 2G & 0 \\ 0 & 3K \end{bmatrix} \begin{bmatrix} N_r \\ N_z \end{bmatrix} \tag{3.14}$$

$$\eta = P \cdot N + H \tag{3.15}$$

and the subscripts r and z indicate the components in the corresponding Lode coordinate directions. We have now reduced the plastic tangent stiffness down to a 2×2 matrix representation for the case of an isotropic material under axisymmetric loading which is assumed to obey classical plasticity theory. Since this reduces the number of independent components of T from 81 to 4, this greatly simplifies the task of experimentally measuring the plastic tangent stiffness tensor.

Chapter 4

Methodology

Flow Rule Validation

To calculate the four components of a tensor such as T, we require two independent sets of vectors related by that tensor. For the case of the plastic tangent stiffness tensor, this means two independent strain increment vectors, and the corresponding stress increment vectors. Since T is a function of the stress state and loading history, these stress and strain increments must occur at the same stress state and point in the loading history. How these incremental vectors are obtained will be discussed later. First we describe the process of solving for the components of the tangent stiffness tensor given the independent sets of vectors related by it. Suppose we have two sets of stress increments ($\dot{\sigma}_1$, $\dot{\sigma}_2$), and strain increments ($\dot{\varepsilon}_1$, $\dot{\varepsilon}_2$) related by the same plastic tangent stiffness tensor:

$$\begin{bmatrix} \dot{\sigma}_{1r} \\ \dot{\sigma}_{1z} \end{bmatrix} = \begin{bmatrix} T_{11} & T_{12} \\ T_{21} & T_{22} \end{bmatrix} \begin{bmatrix} \dot{\varepsilon}_{1r} \\ \dot{\varepsilon}_{1z} \end{bmatrix} \tag{4.1}$$

and

$$\begin{bmatrix} \dot{\sigma}_{2r} \\ \dot{\sigma}_{2z} \end{bmatrix} = \begin{bmatrix} T_{11} & T_{12} \\ T_{21} & T_{22} \end{bmatrix} \begin{bmatrix} \dot{\varepsilon}_{2r} \\ \dot{\varepsilon}_{2z} \end{bmatrix} \tag{4.2}$$

The two equations above may be combined into a single matrix equation:

$$\begin{bmatrix} \dot{\sigma}_{1r} & \dot{\sigma}_{2r} \\ \dot{\sigma}_{1z} & \dot{\sigma}_{2z} \end{bmatrix} = \begin{bmatrix} T_{11} & T_{12} \\ T_{21} & T_{22} \end{bmatrix} \begin{bmatrix} \dot{\varepsilon}_{1r} & \dot{\varepsilon}_{2r} \\ \dot{\varepsilon}_{1z} & \dot{\varepsilon}_{2z} \end{bmatrix} \tag{4.3}$$

where the subscripts 1 and 2 indicate the first and second vector set. The components of T can be found by multiplying both sides of equation (4.3) by the inverse of the strain matrix:

$$\begin{bmatrix} T_{11} & T_{12} \\ T_{21} & T_{22} \end{bmatrix} = \begin{bmatrix} \dot{\sigma}_{r1} & \dot{\sigma}_{r2} \\ \dot{\sigma}_{z1} & \dot{\sigma}_{z2} \end{bmatrix} \begin{bmatrix} \dot{\varepsilon}_{r1} & \dot{\varepsilon}_{r2} \\ \dot{\varepsilon}_{z1} & \dot{\varepsilon}_{z2} \end{bmatrix}^{-1} \tag{4.4}$$

If there were more than two independent stress/strain increment sets related by the same tensor, the strain and strain rate matrices in equation (4.3) would not be square. A pseudo-inverse operation could be used in equation (4.4) instead of the inverse operation. This would yield the tensor which best fits the vector data.

Obtaining two independent stress/strain increments at the same material state is not trivial. It is to avoid this problem that most studies of this nature turn to computational methods, which allow this to be done easily. As discussed above, most experimental studies have sought to overcome this problem by preparing a set of nominally identical specimens and loading them each through identical load paths, then applying a different loading increment to each specimen. Valuable data have been obtained using this method, which will serve as a validation measure for the current study. To eliminate the need for "identical" samples, the method described in this report allows independent loading increments to be obtained at the same state from a single specimen using cyclically applied loading increments and an interpolation scheme.

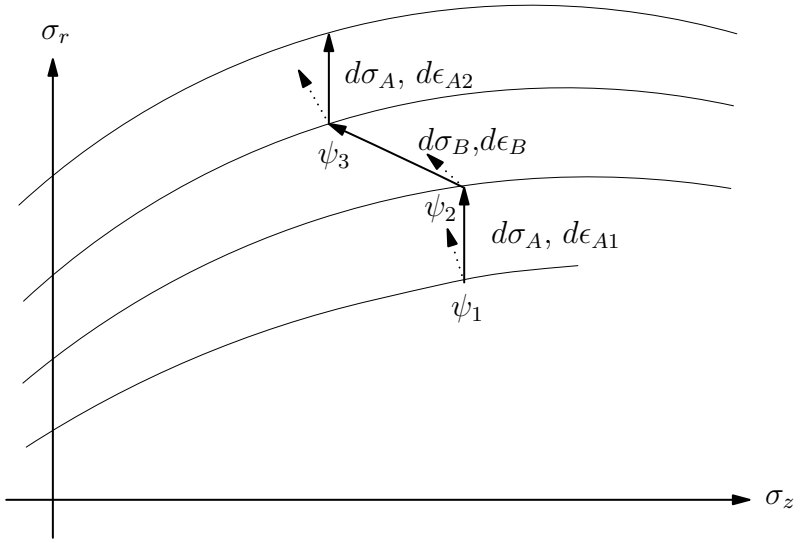


Figure 4.1. A simple cyclically applied incremental loading. Solid vector lines indicate stress vectors, dotted vector lines indicate strain vectors.

This concept is illustrated in Figure 4.1, where the cyclical load begins at an initial material state denoted by ψ_1. An incremental stress loading vector $d\sigma_A$ is then applied taking the material state to ψ_2. Then, a different stress loading vector $d\sigma_B$ is applied, taking the material state to ψ_3. Finally, the incremental loading vector $d\sigma_A$ is applied again, this time beginning from material state ψ_3. In each case, the incremental strain vector is measured. We are now left with three stress/strain incremental vector sets at three different material states. If we wish to find the tangent stiffness tensor at material state ψ_2, we need to know what the strain response vector would have been had we applied the loading vector $d\sigma_A$ at material state ψ_2. While we do not have this information, we do know what the strain response vector corresponding to $d\sigma_A$ was immediately

before, and immediately after material state ψ_2. It is assumed that interpolation may be used with these two pieces of information to infer what the strain response *would have been* at material state ψ_2 if the loading vector $d\sigma_A$ would have been applied at that point. In the limit of small loading increments this assumption is valid if the material changes in a continuous manner with the state variables. The material could change discontinuously as a result of vertices in the yield function, phase transformations, and other such sources. The validity of this assumption will be assessed by comparing the results of this analysis with studies which have used other methods and assumptions. With this interpolated strain response vector we will have two independent loading vectors, and the corresponding strain vectors at the same material state. This is sufficient to find the components of the tangent stiffness tensor using equation (4.4).

In practice, a slightly more complicated incremental loading cycle has been used. Rather than only using two independent loading directions, four have been used. Unloading increments have been included in the cycle, to allow the potentially evolving elastic tangent stiffness to be calculated in a similar manner.

Knowing the plastic and elastic tangent stiffness tensors will allow M and N to be calculated directly from the experimental data. To do this we solve equation (3.12) for the second term on the right, which we will label A:

$$A = E - T = \frac{1}{\eta} P \otimes Q \tag{4.5}$$

The rows of A should be scalar multiples of Q and the columns should be scalar multiples of P. To find the directions of P and Q we perform a polar decomposition of A. To perform this decomposition we define:

$$\begin{aligned} U^2 &= A^T \cdot A \\ &= (Q \otimes P) \cdot (P \otimes Q) \\ &= (P \cdot P) Q \otimes Q \end{aligned} \tag{4.6}$$

As shown, U^2 will be a scalar multiple of the dyad $Q \otimes Q$. U^2 should then have one large eigenvalue and one small eigenvalue. The eigenvector associated with the large eigenvalue will be in the direction of Q. Similarly we define:

$$\begin{aligned} V^2 &= A \cdot A^T \\ &= (P \otimes Q) \cdot (Q \otimes P) \\ &= (Q \cdot Q) P \otimes P \end{aligned} \tag{4.7}$$

Again, the eigenvector associated with the largest eigenvalue of V^2 will be in the direction of P. We now use the definitions of P and Q to write:

$$P^* = \alpha E \cdot M \tag{4.8}$$

$$Q^* = \beta E \cdot N \tag{4.9}$$

where α and β are some unknown scalars, and P^* and Q^* are scalar multiples of P and Q respectively. Since E is known from the unloading vectors, equations (3.2) and (3.3) may be solved for the directions of M and N:

$$M^* = E^{-1} \cdot P^* \tag{4.10}$$

$$N^* = E^{-1} \cdot Q^* \tag{4.11}$$

where $*$ is again used to indicate some scalar multiple of a variable, which may then be used to generate a unit vector in the direction of the tensor.

Cap Model Hardening Validation

To assess the validity of an increase in hydrostatic yield strength due to inelastic shear deformation, a series of modified triaxial compression load paths has been designed. The first of these load paths consists of purely hydrostatic loading, with small unloading increments applied periodically. This test is performed to identify the level of hydrostatic loading where inelastic deformation occurs. This will be the initial location of the "cap" of the yield surface. The second test is a traditional triaxial compression test. In this test the sample is loaded hydrostatically to a point just below the cap identified in the first test. Then the lateral stress is held constant while the axial stress is monotonically increased until the material fails. As the axial stress is increased, the volumetric strain is monitored. The volumetric strain will initially decrease (decrease in volume), then will reach a point where the sample volume begins to increase.

Figure 4.2 illustrates the third load path through stress space. The path is identical to the traditional triaxial compression path (load path 2), except that after the onset of dilatation, the triaxial compression leg is stopped. The specimen is returned to a state of pure hydrostatic stress via a path with a constant mean stress. The specimen is then loaded in hydrostatic compression to the limits of the machine capacity. As Figure 4.2 illustrates, according to some models, the shear loading should greatly increase the hydrostatic yield strength. The proposed validation load path tests this by first inelastically loading in shear to cause the desired hardening, then loading in hydrostatic compression to see if the hydrostatic yield strength is significantly different than that of a virgin sample.

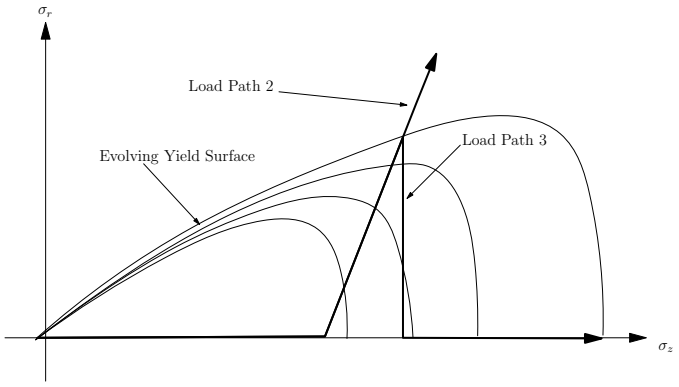


Figure 4.2. Sketch of a triaxial compression test (bold arrow) with a corresponding unvalidated yield surface evolution that predicts outward motion of the cap even after onset of dilatation; in the theoretical model under investigation, the onset of dilatation corresponds to the point where the load path crosses over the peak point of the evolving cap.

Chapter 5

Testing Procedure

Sample Preparation

Three metals, a ceramic and a rock were tested as part of this study. Sample sizes are listed in the test list. All samples were prepared into the shape of a right circular cylinder. The dimensions of all samples were nominally length-to-diameter ratios of 2:1 as recommended for uniaxial and triaxial compression tests (ASTM D4534). The metals and ceramic were delivered in rods and their outer diameter was used as is, except that it was cleaned and or sanded lightly. The rods were cut to length using a saw. The rock samples were cored from blocks of rock, perpendicular to bedding. The ends of all samples were ground flat and parallel using a surface grinder.

The metal and ceramic samples were mounted with strain gages to record axial and lateral strains as shown in Fig. (5.1). Two (at 180° intervals) or three (at 120° intervals) strain gage pairs were mounted at the middle of each specimen, each pair consisting of an axial and a lateral strain gage. The gages are mounted with a thin layer of quick curing epoxy and are placed by hand on the specimen. The redundancy in strain measurements was done in order to assess the potential for specimen/loading column alignment, asymmetry in the loading, etc. The strain gages are 2% foil gages with a resolution of 10 μstrains. For each strain gage pair, the axial strain gage (parallel to the long axis of the sample) and lateral strain gage (perpendicular to the long axis of the sample) were used to measure axial and lateral strains, respectively. The redundancy of strain gage measurements was used to best quantify strains measured, as well as to determine if there was sample misalignment and, in some cases, to account for loss of an individual gage output during a test.

Metal specimens were coated with paint-on urethane to protect the strain gages and to hold the sample and the end caps together. An attempt was made to minimize sample misalignment by inserting a spherical interface at top platen.

Prepared rock specimens (Fig. 5.2) were first covered with a single ply of thin (.005 in) annealed copper (Fig. 5.3) to prevent the confining pressure fluid (Isopar) from contacting and/or entering the pore space of the specimen when it was placed in the pressure vessel. The jacket was fabricated by winding it around the specimen and soldering a seal along the specimen axis. Liquid polyurethane was applied to the end of the copper jacket that lapped over the two cylindrical steel end caps that were placed on either end of the specimen. For curing, this assembly was mounted in

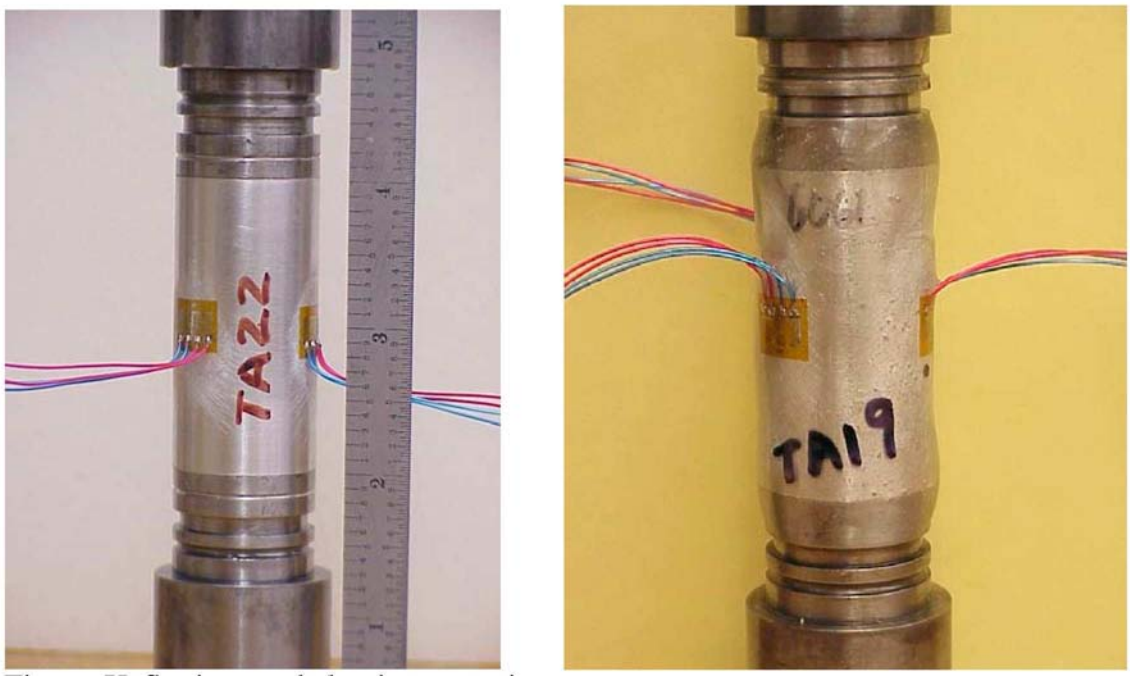


Figure 5.1. Strain gaged aluminum specimens

a lathe and slowly rotated around its central axis to maintain uniform thickness of the polyurethane lapping membrane.

When the urethane had cured, the sample was placed in a pressure vessel and pressurized externally using line air pressure. This pressurization pressed the copper jacket snuggly against the rock. Next, on opposing sides of the sample at the axial midpoint, a locator button was soldered (Fig. 5.4).

Instead of strain gages, rock test specimens were instrumented with electronic deformation transducers before they were placed in the pressure vessel assembly. Radial deformation was measured as the point measurement across the specimen diameter by a linear variable differential transformer (LVDT). The resolution of the LVDTs used is 0.0002. The radial LVDT is spring loaded and is positioned on the buttons attached to the sample (Fig. 5.4). Axial deformation was measured by two linear variable differential transformers (LVDTs) mounted to the specimen end caps across the specimen length. The displacement recorded is the average from the two gages. The change in this electrical output versus displacement was established prior to testing through calibration.

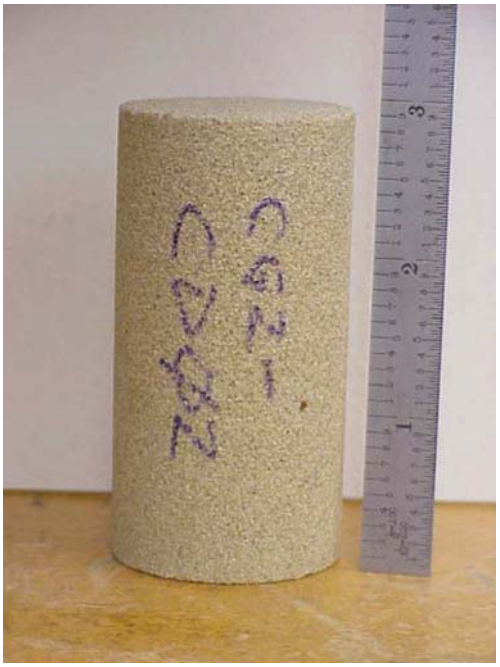


Figure 5.2. Right circular cylinder of Castlegate sandstone.

Test Method

Strength and deformational properties of pressure-sensitive materials such as rock are commonly determined using the quasi-static triaxial compression test. In using this technique, cylindrical test specimens are initially subjected to an all-around pressure (or confining pressure) and then are loaded to failure by applying compressive force to the ends of the specimens (i.e., parallel to their central axes). The difference between the axial load (expressed in terms of stress) at failure and the confining pressure applied to the sides of the specimen is defined as the confined compressive strength. The effect of confining pressure on compressive strength is evaluated by conducting a series of tests at different confining pressures spanning the range of interest. Test specimens are normally instrumented (described above) to measure axial and radial deformations (strains) during the application of both the confining pressure (i.e., hydrostatic loading) and axial load (i.e., shear loading). Stress-strain data are useful in evaluating particular mechanical properties such as elastic moduli.

Figure 5.5 shows the computer-controlled servohydraulic testing system used to conduct the room-temperature (77F) quasi-static triaxial compression tests for this study. The system comprised an SBEL pressure vessel assembly and an MTS Systems reaction frame. During testing, the pressure vessel housed the test specimen and was hydraulically connected to a pressure intensifier capable of inducing pressures up to 55,000 psi using silicon oil (Isopar) as the pressurizing medium. The reaction frame is equipped with a movable cross-head to accommodate various



Figure 5.3. Right circular cylinder of Castlegate sandstone jacketed in copper with end caps attached.

sizes of pressure vessel assemblies and is capable of applying axial loads up to 1,000,0000 pounds through a hydraulic actuator located in the base of the frame. Vessel pressures were measured by a pressure transducer plumbed directly into a port machined in the vessel, whereas axial loads were measured by a load cell inside the pressure vessel (resolution of 5 pounds, accurate to 0.5% at full scale [45,000 lbf]).

Setup of the quasi-static triaxial compression tests included placing the jacketed, instrumented specimen assembly into the pressure vessel, connecting instrumentation leads to feed-throughs in the pressure vessel, filling the vessel with oil, and mounting the pressure vessel assembly into the reaction frame (see Fig. 5.5). The actuator in the base of the frame was then advanced gradually raising the pressure vessel assembly into position for the test. No axial load was placed on the sample prior to the test, rather, the loading piston was advanced until it was very close to applying a load. Then, initiation of the test was turned over to the TESTAR test system controllers which automatically increased the confining pressure to the correct target hydrostatic stress (all-around pressure); the loading frame was in displacement control while increasing the confining pressure. Confining pressure loading was sometimes interrupted several times during each test to initiate an unload/reload cycle. The unload/reload stress-strain data may be used to evaluate elastic moduli.

For the tests on rock, once the test system had stabilized at the target pressure, the system was

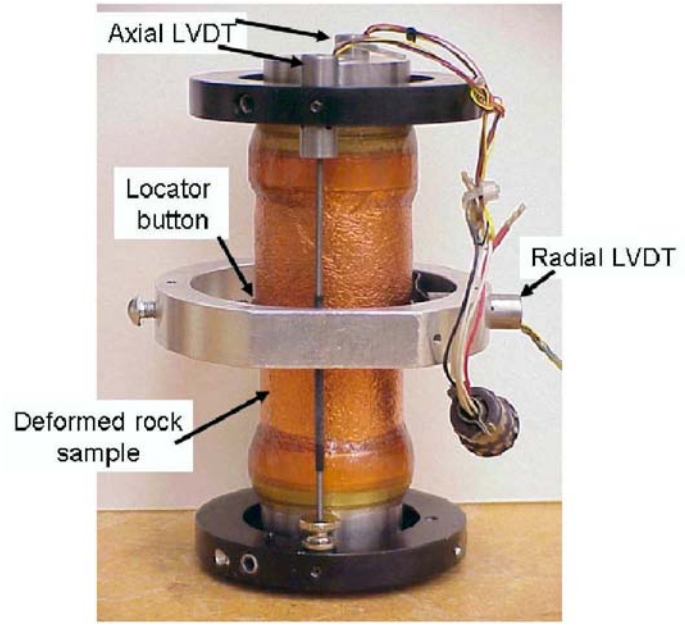


Figure 5.4. Right circular cylinder of deformed Castlegate sandstone, showing the complete sample assembly with axial and radial LVDTs

switched to stroke control and additional axial load was applied to the specimen using axial strain rate as the feedback mode. When the system was switched to total stroke control, the location of the top of the sample had to be found by the machine. This was accomplished by telling the machine to search for the sample in axial load steps of a specific size until the sample is found by applying a small force/stress. During this time, the confining pressure is held constant. Ultimately, the sample is found and some time later, the test is begun, by increasing axial stress at a specified rate to arrive at a starting stress state in net path mode. In data analysis, there is a time pick on start of the test. For absolute determinations of axial stress, the internal force gage reading should be re-zeroed at the test start. The strain rate applied in all tests was $1 \times 10^{-4}\ s^{-1}$. Axial loading was sometimes interrupted several times during each test to initiate an unload/reload cycle. Axial loading continued until either a peak axial load was observed or the desired range of the deformation was achieved.

For the tests on metal and ceramic, once the test system had stabilized at the target pressure, the system was switched to total axial stress control using the internal load cell and confining pressure transducer. When the system was switched to total axial stress control, the location of the top of the sample had to be "found" by the machine. If a path load test was performed, at this point in the test, the path loading was begun. When in net loading or path loading, lateral and axial loads were programmed and controlled separately and simultaneously based on a rate to target stress state(s). It will be shown later that sometimes the stress states were achieved by multi-directional axisymmetric loading.

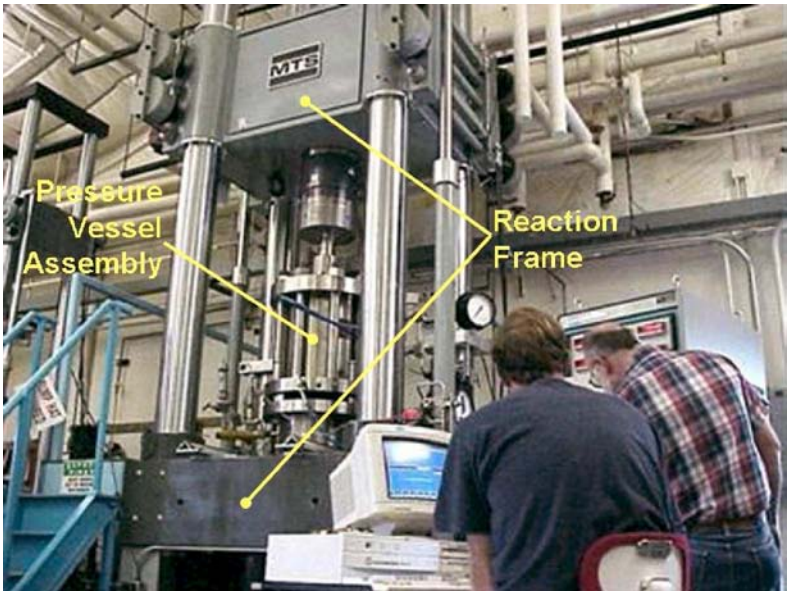


Figure 5.5. Testing system used to conduct quasi-static triaxial compression tests.

We completed a total of 43 experiments on copper (2), aluminum, steel, ceramic (2), Salem Limestone, and Castlegate Sandstone (Table 5). Some of the experiments were conducted to figure out how to best perform an experiment, some experiments were conducted to search out materials that we could test in a manner such that we could measure the desired response within the load limits of the experimental apparatus with the desired control on force (stress) and displacement (strain) to provide value to the analysis.

Calibration

Data collected in the experimental study included force, pressure, and displacement. Typically, these data are acquired using electronic transducers in which the electrical output is proportional to the change in the measured variable. In all cases, the constants of proportionality were determined through careful calibration using standards traceable to the National Institute for Standards and Technology.

Table 5.1. Experiment number, test date, specimen dimensions and confining pressure.

Test ID	file Date	Material	Diameter in	Length in	Confining Pressure ksi	notes		
LP-TA01	11/17/2006	C101 copper	0.500	1.050	5	simple triax		
LP-TA02	11/20/2006	Porous ceramic (filter mat'l)	0.505	0.990	5	simple triax	damaged during initial ax loading	
LP-TA03	12/11//2006	C101 copper	0.500	1.020	various	simple step program demo		
LP-TA04	2/21/2007	C101 pure copper	0.500	1.010	20	simple path control	stress states not Z-R space	
LP-TA05	2/23/2007	C101 pure copper	0.500	1.050	15	first z-r space control		
LP-TA06	2/26/2007	steel billet blank	1.000	2.000	14	load path	z-r control	
LP-TA07	5/17/2007	NA –Steel Billet	0.900	2.000	10	load path		
LP-TA08	5/18/2007	Macor ceramic	0.540	1.055	15	load path	no strain data	
LP-TA09	5/22/2007	Macor ceramic	0.540	1.079	24	load path		
LP-TA10	5/23/2007	Macor low porosity ceramic	0.540	1.080	22			
LP-TA11	5/23/2007	C101 copper rod	0.500	1.030	15	load path	attempt to define control data	
LP-TA12	6/26/2007	C101 copper rod	0.500	1.010	15	load path		
LP-TA13	9/21/2007	Copper bar annealed	0.998	1.971	15	load path		
LP-TA14	11/7/2007	Porous ceramic	1.040	2.010	4.5, 6.5	load path 15% legs	no failure	
LP-TA15	5/16/2008	6061-T0 Alum bar (extruded, annealed)			15	load path 15% legs	first use of leg tags	
LP-TA16	5/22/2008	6061-T0 Alum bar (extruded, annealed)			17.5	load path 15% legs		
LP-TA17	5/29/2008	6061-T0 Alum bar (extruded, annealed)	1.002	1.740	21.5	load path 15% legs		
LP-TA18	6/2/2008	6061-T0 Alum bar (extruded, annealed)	1.001	2.004	20	net path only		
LP-TA19	6/4/2008	6061-T0 Alum bar (extruded, annealed)	1.002	1.901	20	load path 15% legs		
LP-TA20	6/26/2008	6061-T0 Alum bar (extruded, annealed)	1.002	1.902	19.4	load path 15% legs		
LP-TA21	7/1/2008	6061-T0 Alum bar (extruded, annealed)	1.002	1.899	20.6	load path 15% legs		
LP-TA22	9/9/2008	6061-T0 Alum bar (extruded, annealed)	1.001	2.023	19.4	load path 50% legs		
LP-TA23	9/10/2008	6061-T0 Alum bar (extruded, annealed)	1.001	2.020	18.8	load path 50% legs		
LP-TA24	9/10/2008	6061-T0 Alum bar (extruded, annealed)	1.002	2.014	18.4	load path 50% legs		
LP-TA25	9/11/2008	6061-T0 Alum bar (extruded, annealed)	1.002	2.017	19.4	net path only		
SL-CD01	2/12/2007	Salem limestone	1.010	2.000	13.5	Cap development		
SL-CD03	2/13/2007	Salem limestone			na	Cap development	strain errors during hydro	
SL-CD04	2/14/2007	Salem limestone				Cap development		
SL-CD05	2/16/2007	Salem limestone	1.010	2.000	15	Cap development		
CG-CD02	6/18/2008	Castlegate sandstone	1.994	3.910	59	Cap development	hydrostatic	
CG-CD03	6/24/2008	Castlegate sandstone	1.991	3.854	10, 37	Cap development	hydrostat, triax	
CG2-CD01	8/22/2008	Castlegate sandstone	1.495	2.933	5	Cap development	hydrostat, triax	new sample size
CG2-CD02	8/25/2008	Castlegate sandstone	1.496	2.916	5	Cap development	hydrostat, triax	
CG2-CD03	8/26/2008	Castlegate sandstone	1.496	2.917	50	Cap development	hydrostatic	
CG2-CD04	8/27/2008	Castlegate sandstone	1.496	2.925	53.5	Cap development	hydrostatic	
CG2-CD05	8/28/2008	Castlegate sandstone	1.494	2.848	56	Cap development	hydrostatic	
CG2-CD06	8/29/2008	Castlegate sandstone	1.492	2.937	32	Cap development	hydrostat, triax	
CG2-CD07	8/29/2008	Castlegate sandstone	1.492	2.895	30	Cap development	hydrostat, triax	
CG2-CD08	9/3/2008	Castlegate sandstone	1.494	2.919	30	Cap development	hydrostat, triax	2 lateral gages
CG2-CD09	9/5/2008	Castlegate sandstone	1.494	2.926	24	Cap development	hydrostat, triax	
CG2-CD10	9/6/2008	Castlegate sandstone	1.493	3.073	20	Cap development	hydrostat, triax	
CG2-CD11	9/7/2008	Castlegate sandstone	1.494	3.090	12	Cap development	hydrostat, triax	
CG2-CD12	9/12/2008	Castlegate sandstone	1.494	3.000	7	Cap development	hydrostat, triax	Pc per Holcomb

Chapter 6

Discussion of Results

Regular Flow Rule

The first aim of this study was to develop a load path suitable for assessing the validity of the classical plasticity assumption of a regular flow rule. Four loading directions were selected. We define a stress increment by:

$$\begin{aligned} \dot{\sigma}_z &= \dot{\Sigma}\cos\alpha \\ \dot{\sigma}_r &= \dot{\Sigma}\sin\alpha \end{aligned} \tag{6.1}$$

where $\dot{\Sigma}$ is the increment magnitude and α is the angle formed between the stress increment and the hydrostatic compression axis. The four legs labeled A, B, C and D are described in Table (6).

Smaller increments were used in early tests, but the measurements had a low degree of repeatability since the "noise" was of the same order of magnitude as the measurements themselves. The increments were progressively made larger until good repeatability was attained.

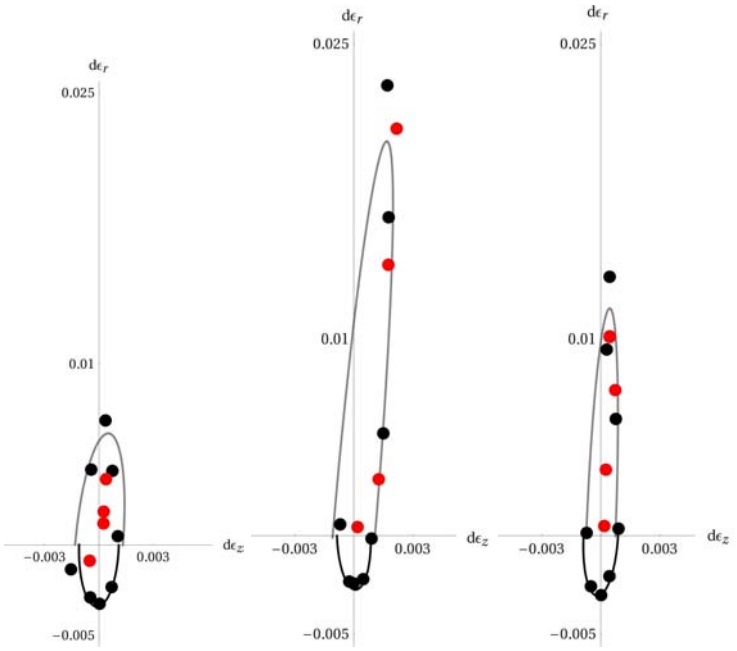
As discussed previously, unloading increments were included so that the elastic properties of the material could also be calculated. The unloading increments were chosen to have the same magnitude as the loading increments. This not only allows the elastic tangent stiffness to be computed, but also allows the plastic strain increments to be directly measured. This is done by measuring the strain increment during the loading and unloading increments of each cycle. The strain

Table 6.1. Description of stress increments where α is the angle formed with the hydrostatic compression axis, and $\dot{\Sigma}$ is the total increment magnitude.

Leg	α	$\dot{\Sigma}$
A	90°	300 psi
B	180°	300 psi
C	35°	300 psi
D	125°	300 psi

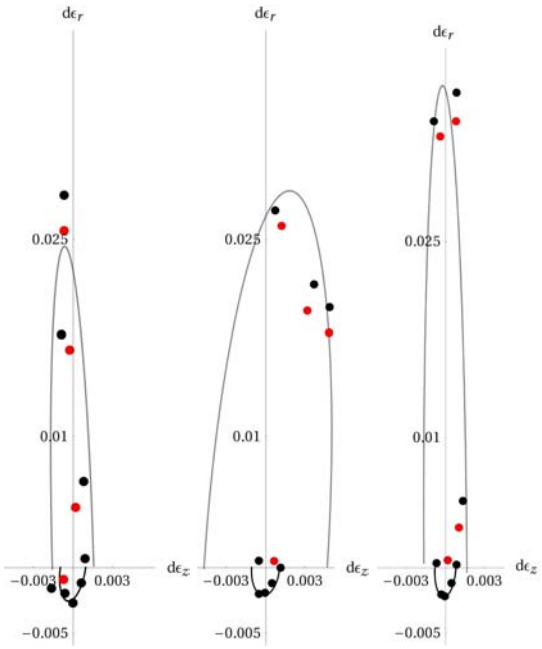
that remains after completely unloading each loading increment is the plastic strain increment for that loading cycle.

Figs. 6.1 and 6.2 show the strain response envelopes for three different tests. These envelopes are constructed from interpolated strain increments from the first loading cycle, which is near the initiation of yielding for each sample. A key feature of these response envelopes is the orientation of the plastic strain increments (red dots). With the exception of a single increment in Fig. 6.1(a), all of the plastic strain increments lie nearly in a straight line in the first quadrant. Similar results were found for the other stress cycles. This means that the direction of the plastic strain increment is the same regardless of the loading direction, which indicates a regular flow rule. This is consistent with the experimental and numerical studies mentioned previously, which seems to validate the interpolation scheme used in this study.



(a) Second cycle of LP-TA22 **(b)** Second cycle of LP-TA23 **(c)** Second cycle of LP-TA24

Figure 6.1. Response envelopes for the second stress cycle of tests LP-TA22 (a), LP-TA23 (a) and LP-TA24 (c). Black dots indicate total strain increments, red dots indicate plastic strain increments. All strain increments have been interpolated to a common material state using a cyclical loading cycle. The partial ellipses are a visualization of the best fit tangent stiffness tensors C (black) and T (gray), which were found via a pseudo-inverse method using the four stress/strain increment pairs. These ellipses represent a circle in stress space mapped to strain space.



(a) Third cycle of LP-TA22 **(b)** Third cycle of LP-TA23 **(c)** Third cycle of LP-TA24

Figure 6.2. Response envelopes for the third stress cycle of tests LP-TA22 (a), LP-TA23 (b) and LP-TA24 (c). Black dots indicate total strain increments, red dots indicate plastic strain increments. All strain increments have been interpolated to a common material state using a cyclical loading cycle. The partial ellipses are a visualization of the best fit tangent stiffness tensors C (black) and T (gray), which were found via a pseudo-inverse method using the four stress/strain increment pairs. These ellipses represent a circle in stress space mapped to strain space.

The plastic strain increments in the third quadrant for test LP-TA22 merit some discussion. The increments shown in Fig. 6.1(a) and 6.2(a) are not anomalies, but were observed for every load increment B in that test. This loading direction is of particular interest because for models which use a pressure dependent yield strength and a non-associated flow rule, this direction lies in or near the Sandler-Rubin wedge. Some degree of pressure dependence in the yield strength was observed in these tests. This means that loading increment B should be directed outward from the yield surface, but at a relatively shallow angle. For such a stress increment the corresponding plastic strain increment would be expected to be small compared to the total strain increment. Since the plastic strain increments are small for these loading increments, they are more prone to experimental error. Nevertheless, the fact that every loading increment B exhibited this behavior is enough to suggest that there *may* be something unusual occurring for loads in this direction.

Non-associated Flow Rule

As discussed previously, the load path used in this study was designed in such a manner as to allow the plastic tangent stiffness tensor T and the elastic tangent stiffness tensor C to be computed directly from the measured stress and strain increments. These calculations were performed using equation (4.4). These tensors are visualized as ellipses in Figs. 6.1 and 6.2. These ellipses represent a circle in stress space $\sigma_r^2 + \sigma_z^2 = (300psi)^2$, transformed to strain space via the calculated "best fit" stiffness tensors T and C. The ellipses for the second cycle (Fig. 6.1) appear to fit the data rather well. It is noted that the strain response envelope should be continuous. This means that the ellipse formed by the plastic tangent stiffness tensor T and the ellipse formed by the elastic tangent stiffness tensor C should intersect where the yield surface intersect the circle in stress space. This is nearly the case for the strain envelopes in Fig. 6.1. However, the strain envelopes for the third cycle (Fig. 6.2) are discontinuous. This might indicate that, at such large plastic strain increment magnitudes, more data are required to obtain a better fit for tangent stiffness tensors. Alternatively, noting that the initially nearly uniform distribution of stimulus vectors (i.e. the stress increments) transform to a grouping of relatively clustered response vectors (strain increments), it is possible that the material is undergoing a nonlinearity in the response vector density. An example of a nonlinear response vector density is shown in Fig. 2.1(d), perhaps even suggesting the formation of an "unattainable" wedge in the response vectors. Again, further data for a larger variety of loading directions is needed to investigate this conjecture.

Using these "best fit" tangent stiffness tensors, the directions of the yield surface normal N and plastic strain rate direction M were calculated using equations (4.5) through (4.9). The results of these calculations are found in Table 6. The directions of M and N do not coincide for any of the cases, which seems to indicate a non-associated flow rule. Induced anisotropy may play a role in creating apparent non-associativity. Despite having been annealed, it is clear that some degree of anisotropy was inherent in the specimens used in these tests. This can be clearly seen in the σ_r vs ε_r stress strain curves, as in Fig. 6.3. Due to the unidirectional nature of the initial phase of the load path, it is not possible to discern the amount of anisotropy which was inherent in the sample, and how much was induced by plastic deformation. This adds a degree of uncertainty in the results of this aspect of the study that can be rectified by adding stress increment probing to the initial elastic legs. Due to these factors, and the limited amount of data, more investigation would be required to make any firm conclusions based upon these calculations.

Table 6.2. Direction of the yield surface normal N and the plastic strain rate M referenced to the hydrostatic compression axis.

Step	θ_M	θ_N
2	39°	66°
3	105°	146°
4	125°	198°

(a) LP-TA22

Step	θ_M	θ_N
2	99°	120°
3	153°	173°
4	-	-

(b) LP-TA23

Step	θ_M	θ_N
2	83°	122°
3	116°	163°
4	131°	179°

(c) LP-TA24

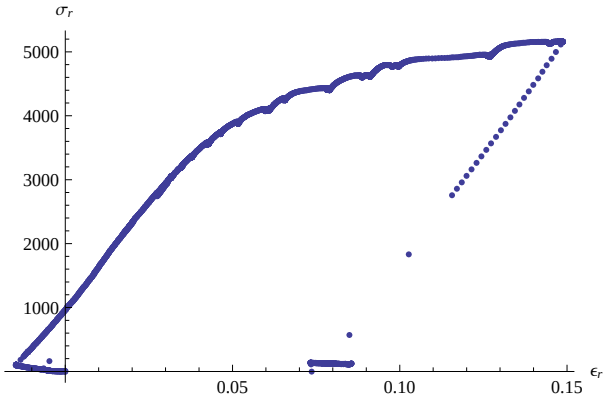


Figure 6.3. The σ_r vs. ε_r stress strain curve for test LP-TA20, illustrating the initial anisotropy in the material. The anisotropy is evidenced by the change (decrease) in the strain ε_r during the initial hydrostatic loading leg of the test where the σ_r stress remains nearly constant. This indicates that the material is undergoing a shear deformation due to a purely hydrostatic loading.

Cap Model Validation

As discussed in the Introduction, non-proportional loading experiments were proposed to investigate the validity of an existing model [6] for the evolution of the cap hydrostat intersection point (i.e., the hydrostatic elastic limit) in response to first loading away from this point (see the cap evolution illustrated in Fig. 4.2).

As seen in Fig. 6.4 the geomechanics theory under investigation accurately predicts dilatation observed in triaxial compression (TXC), but it does so by moving the cap outward (see Fig. 4.2). Such behavior, which has never been validated, is counterintuitive because it implies that dilatation (increasing void space) actually increases the material's resistance to yield in hydrostatic compression. Validating this prediction requires first selecting a material that exhibits dilatation in TXC so that the dilation phase can be interrupted with a change in the loading direction to probe the movement of the cap in response to dilatation. Standard geomechanics testing typically involves no such change in loading directions. Therefore existing data that exhibits dilatation in TXC, such as that in Fig. 6.4 or more recent similar data for Castlegate Sandstone [28] is of limited value in this validation effort other than to suggest an appropriate material for testing. Given that the recent Castlegate Sandstone tested by Holcomb and coworkers [28] displayed a clear dilatation "knee", it seemed natural to reproduce those results and extend them with an excursion to the hydrostat. The block of Castlegate sandstone used by Holcomb was no longer available, so new samples from a different block were used. Unfortunately, however, the TXC dilatation behavior observed by Holcomb was not observed in the new samples. Contrast, for example, the difference in character between Fig. 6.4, which exhibits dilatation, and the blue curve in Fig. A.5, which shows no

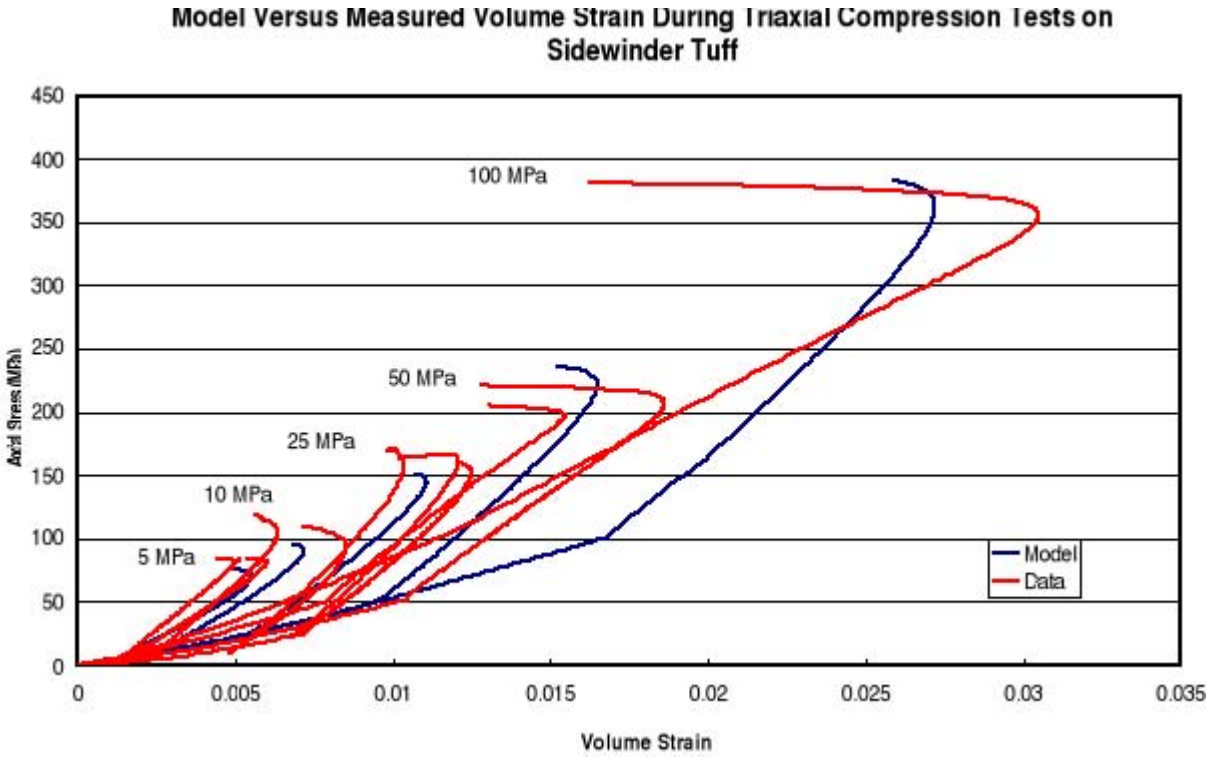


Figure 6.4. Validation of a geomechanics model for loading of Sidewinder Tuff under triaxial compression [27]. (Note: the present work aims to extend validation for changes in the loading direction away from standard triaxial compression load paths of this kind.)

dilatation.

Hydrostatic compression and triaxial compression tests were performed on several Castlegate sandstone specimens at a variety of confining pressures. The hydrostatic compression tests revealed that the hydrostatic yield strength of this material is approximately 35 ksi. For the triaxial compression tests with a confining pressure above 12 ksi the machine capacity was reached before reaching failure or dilatation. For tests with a confining pressure of 12 ksi or less the material did fail, but no dilatation was observed prior to failure. The hardening models under consideration in this study predict an increase in hydrostatic yield strength even in the dilatation range. Since dilatation was never observed in the tests, no assessment of the validity of this aspect of these models is possible from the data. However, the fact that no dilatation was observed, along with some unusual behavior of the lateral strain measurements, calls for further investigation.

Chapter 7

Conclusions

Systematic laboratory experiments on three metals, two rock types, and one ceramic have been conducted to explore validity of unproven assumptions that are common to virtually all plasticity models used in production-level engineering simulations. A particular goal has been to resolve the paradox that non-associativity has been experimentally well established for most materials (including metals), while at the same time any form of non-associativity admits a physically inadmissible dynamic instability that is equivalent to spontaneous motion from a quiescent state. Noting that the stress increments in standard testing are significantly different from the increment that induces instability, it was conjectured that a revision might be required in engineering plasticity models that allows the plastic tangent tensor to vary with the loading direction. Such a feature, if observed, would correspond to a need to revise existing plasticity theories to accommodate incremental nonlinearity. Testing for this possibility required nonstandard tests that aim to quantify the effect of a variety of loading directions on the material response. A secondary goal that also requires changing the loading direction was to assess the merits of hardening models for cap plasticity that counterintuitively predict that volumetric expansion from crack growth in shear causes hydrostatic strengthening.

For tractability, the laboratory experiments were limited to axisymmetric loading, and changes in loading direction were achieved through independent control of axial and lateral components of stress. A cyclic path through stress space was applied, and a means to interpolate between repeated pairs of stimulus-response vectors to any desired point along the loading path was developed. The result of this data analysis was information about material response to stress increments in eight possible directions. The response vectors were visualized using Gudehus strain response diagrams, which simply join the strain increment vectors at their tails so that the tips of these vectors form a closed curve. If the assumption of incremental linearity that is used in classical plasticity theory is correct, then the Gudehus diagram for total strain increments will be an ellipse in elastic loading and the continuous union of two ellipses in elastic-plastic loading. This was generally observed in the data, and mathematical formulas were provided to perform a least-squares fit to the data to determine the tangent modulus for a classical plasticity model to minimize error in general loading. The residual from such a calculation serves as a quantitative metric of the approximation error associated with using classical models.

Since the experiments included both loading and unloading legs, the data were further reduced to decompose the strain increment response vector into elastic and plastic parts, which enabled investigation of the assumption of a regular flow rule. This rule presumes that only the magnitude

of the plastic strain increment is affected by the total strain increment vector, whereas the direction of the plastic strain increment is fixed. In a Gudehus plot, the regular flow rule therefore predicts that the plastic strain increment vectors must point in a single direction. This general behavior was observed overall, but in some of the tests, the loading increment that was closest to the theoretical direction for instability deviated from this direction. Further experiments are needed to confirm the unusual behavior in this loading direction. If this phenomenon is real, then it would preclude the theoretical instability of classical plasticity theories, and revisions of these theories would require introduction of an additional zone of loading with a third tangent tensor, distinct from the conventional plastic and elastic tangent tensors. There are alternative interpretations of the observations in these tests (such as introduction of a backstrain) that might equally well predict such behavior. Moreover, as discussed above, some degree of transverse anisotropy was observed in the results, which could also cause behavior that would be missed by isotropic theories. The material behavior observed in the axisymmetric testing of this research was consistent with several DEM simulations [12] under similar conditions, which suggests that the interpolation scheme used in our study is reasonable and also suggests that the trends observed in the DEM studies are suggestive of real material behavior. As such, it should be noted that the DEM studies explored a much wider range of loading directions, some of which exhibited severe deviations from classical plasticity theory. Therefore further testing is recommended.

As is clear from the numerous test results in the Appendix, a large number of experiments were conducted. Of these, however, only a few gave data that were suitable for analysis of plastic flow behavior. The majority of tests served to develop the testing methodology and material selection. For this reason, our investigation of the validity of plasticity assumptions should be regarded as incomplete but meriting followup testing using the new techniques developed in this research effort.

Although the data are not yet conclusive, the potential for invalidation of incremental plasticity, together with noticeable induced anisotropy, casts serious doubt on the predictiveness of classical nonassociative plasticity models at Sandia (and elsewhere). Controlled validation data are rarely available to the constitutive modeler. This research can improve theories for extrapolating from limited calibration data to the still large set of unexplored loading trajectories typical in engineering applications. Any engineering simulation involving non-monotonic stress increments will probably significantly benefit from investment in development of incrementally nonlinear plasticity theories, as well as induced anisotropy. To

prioritize new experimental and theoretical efforts in this area, it is recommended that the loading paths that materials undergo in engineering simulations be monitored so that those loading paths receive highest priority in testing.

References

[1] A. Belyakov, K. Tsuzaki, Y. Kimura, Y. Kimura, and Y. Mishima. Comparative study on microstructure evolution upon unidirectional and multidirectional cold working in an fe-15 *Materials Science and Engineering: A*, 456(1-2):323 – 331, 2007.

[2] A. Strachan. First principles-based multiscale modeling of materials. In *Multiscale Material Modeling Minisymposium at the Seventh U.S. National Congress on Computational Mechanics*, 2003. July 27-31, 2003, Albuquerque, proceedings not published.

[3] G.Z. Voyiadjis and R.K.A. Al-Rub. Nonlocal gradient-dependent thermodynamics for modeling scale-dependent plasticity. *Int. J. for Multiscale Computational Engineering*, 5(3-4):295–323, 2007.

[4] J.R. Rice R. Hill. Constitutive analysis of elastic-plastic crystals at arbitrary strain. *J. Mech. Phys. Solids*, 20:401–413, 1972.

[5] G.R. Johnson and W.H. Cook. A constitutive model and data for metals applicable at high strain rate. In *Proc. 7th International Symposium on Ballistics*, pages 541–547, 1983.

[6] A. F. Fossum and R. M. Brannon. *The SANDIA GEOMODEL Theory and Users Guide*. Sandia National Laboratories Report SAND2004-3226, Albuquerque, unlimited release edition, August 2004.

[7] R.M. Brannon and T. Fuller. On the induced anisotropy required for thermodynamic consistency with a pressure-dependent shear modulus. *Int. J. Solids Structures*, in review.

[8] R. Hill. *The mathematical theory of plasticity*. Oxford engineering science series. Oxford University Press, 1998.

[9] Z.J. Li, G. Winther, and N. Hansen. Anisotropy in rolled metals induced by dislocation structure. *Acta Materialia*, 54(2):401 – 410, 2006.

[10] Y. M. A. Hashash, J. I. Yao, and D. C. Wotring. Glyph and hyperstream representation of stress and strain tensors and material constitutive response. *Int. J. Numer. Anal. Meth. Geomech.*, 27:603–626, 2003.

[11] G. Gudehus. A comparison of some constitutive laws for soils under radially symmetric loading and unloading. In Aachen and Wittke, editors, *3rd International Conference on Numerical Methods in Geomechanics*, volume 4, pages 1309–1324. Balkema Publisher, 1979.

[12] G. Viggiani C. Tamagnini, F. Calvetti. An assessment of plasticity theories for modeling the incrementally nonlinear behavior of granular soils. *Journal of Engineering Mathematics*, 52:265–291, 2005.

[13] F. Darve F. Nicot. Basic features of plastic strains: From micro-mechanics to incrementally non-linear models. *International Journal of Plasticity*, 23:1555–1588, 2007.

[14] F. Alonso-Marroquin and H. J. Herrmann. Calculation of the incremental stress-strain relation of a polygonal packing. *Phys. Rev. E*, 66(2):021301, Aug 2002.

[15] N. Kuganenthira A Anandarajah, Khaled Sobhan. Incremental stress-strain behavior of granular soil. *Journal of Geotechnical Engineering*, 121:57–68, 1995.

[16] T. Doanh P. Royis. Theoretical analysis of strain response envelopes using incrementally non-linear constitutive equations. *Int. J. Numer. Anal. Meth. Geomech.*, 22:97–132, 1998.

[17] D.C. Drucker. A more fundamental approach to plastic stress-strain relations. In *Proceedings of the U.S. National Congress of Applied Mechanics*, pages 487–491, 1951.

[18] D.C. Drucker. Some implications of work hardening and ideal plasticity. *Quarterly of Applied Mathematics*, 7:411–418, 1950.

[19] R.J. Sober W.A. Spitzig and O. Richmond. The effect of hydrostatic pressure on the deformation behavior of maraging and hy-80 steels and its implications for plasticity theory. *Metallurgical Transactions A*, 7A:1703–1710, 1976.

[20] A. Scarpas X. Liu, X.H. Cheng and J. Blaauwendraad. Numerical modelling of nonlinear response of soil. part 1: Constitutive model. *International Journal of Solids and Structures*, 42:1849–1881, 2005.

[21] I.S. Sandler and D. Rubin. The consequences of non-associated plasticity in dynamic problems. In C.S. Desai, editor, *Constitutive Laws for Engineering Materials: Theory and Applications*, pages 345–352. Elsevier Science Publishing, 1987.

[22] I.S. Sandler and T.A. Pučik. Non-uniqueness in dynamic rate-independent non-associated plasticity. pages 1–2.

[23] T. A. Pučik. A case study of instability and nonuniqueness induced by nonassociated plastic flow. Unpublished.

[24] M. Gordon and F. X. Garaizar. Wave speeds for an elastoplastic model for two-dimensional deformations with a non-associative flow rule. Center for Research in Scientific Computation and Department of Mathematics, Box 8205, North Carolina State University, Raleigh, NC 27695.

[25] R.M. Brannon and W.J. Drugan. Influence of non-classical elastic-plastic constitutive features on shock wave existence and spectral solutions. *J. Mech. Phys. Solids*, 41(2):297–330, 1993.

[26] R.M. Brannon. *Elements of Phenomenological Plasticity: geometrical insights, computational algorithms, and applications in shock physics*. Shock Wave Science and Technology Reference Library: Solids I. Springer-New York, 2007.

[27] A.F. Fossum. Triaxial compression testing of sidewinder tuff. Unpublished.

[28] D.R. Holcomb. Triaxial compression testing of castlegate sandstone. Unpublished.

Appendix A

Summary of Tests

A.1 Cap Model Validation Tests

A.1.1 CG-CD02

This test was a purely hydrostatic test. The maximum pressure attained in this test was approximately 60 ksi, with resulting maximum volumetric strain of approximately 10%. The material appeared to yield at approximately 40 ksi pressure (σ_z =69ksi) and 4.5% volumetric strain as shown if Fig. (A.1).

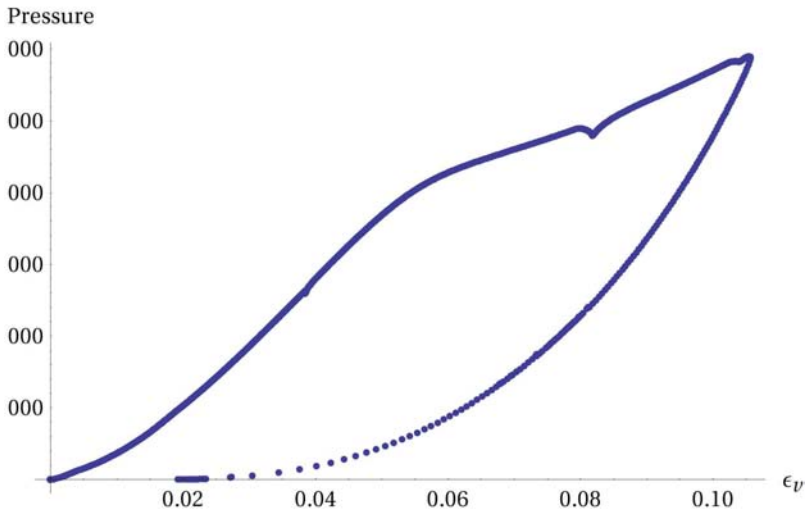


Figure A.1. Hydrostatic compression curve for CG-CD02. ε_v represents the volumetric strain.

A.1.2 CG-CD03

This test was an attempt at load path three (triaxial compression until midway between the critical point and failure point, then return to hydrostatic loading). The sample was subjected to hydrostatic loading to 10 ksi, then underwent triaxial compression until the stress deviator reached 9591 ksi. The load was then ramped down to the hydrostatic axis and hydrostatic loading continued until the pressure was approximately 37 ksi. The lateral strain gage was very erratic, resulting in strange discontinuous stress/strain curves.

A.1.3 CG2-CD03

This test was a purely hydrostatic test. The material appeared to yield at approximately 35 ksi as shown in the plot below. Near the end of the test the lateral strain gage failed resulting in the sharp "spike" in the stress/strain curves.

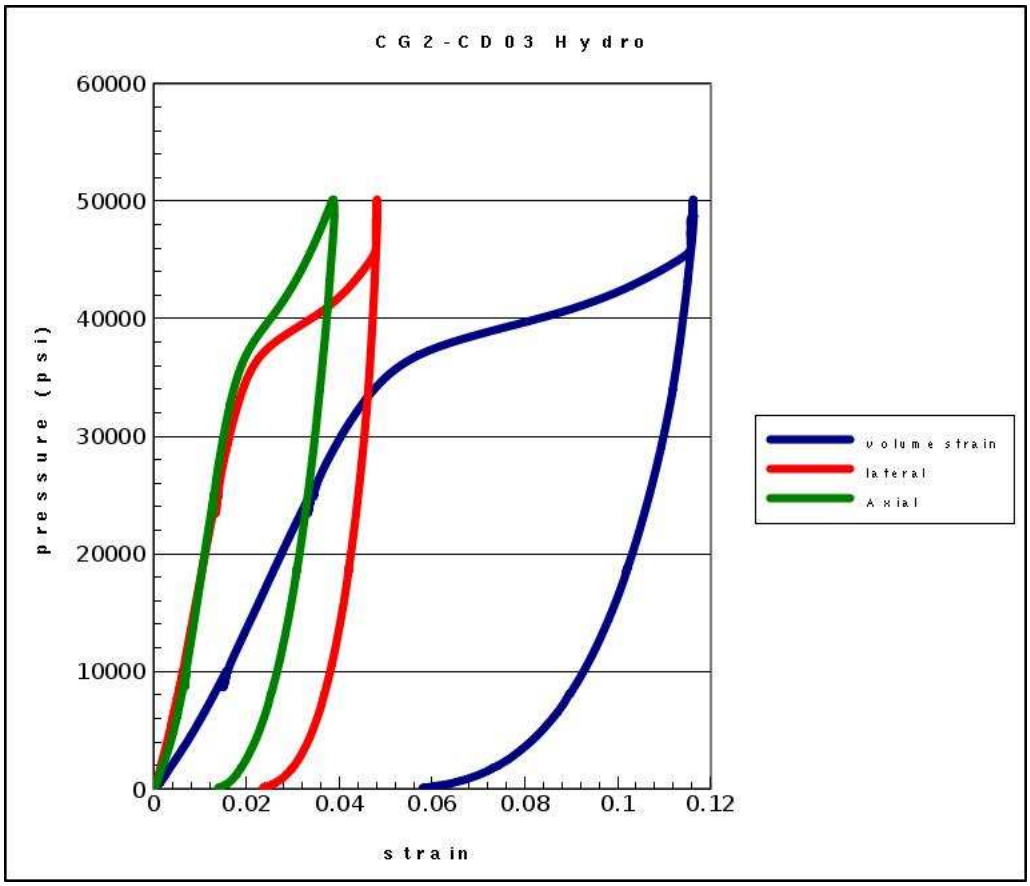


Figure A.2. Stress/strain curves for test CG2-CD03.

A.1.4 CG2-CD04

This test was also a hydrostatic test, however, the results were quite different from CG2-CD03.

A.1.5 CG2-CD05

This test appears was identical to CG2-CD04. This seems to suggest that these two test agree, and that there is a problem with CG2-CD03.

A.1.6 CG2-CD06

This test was a triaxial compression test with a confining pressure of 32 ksi. The lateral strain measurement appeared to be very unusual as shown in Fig. A.3. The load cell capacity was reached before the material failed. No dilatation was observed in this test.

A.1.7 CG2-CD07

Due to the strange lateral strain measurement in CG2-CD06, the test was repeated with a confining pressure of 30 ksi. Similar results were observed. As with test CG2-CD07, the load cell reached its limit before the material failed.

A.1.8 CG2-CD09

In a attempt to fail the material the confining pressure was further reduced to 24 ksi. Material failure was still not attained before the load cell capacity was reached. However, the strain measurements were trending in the expected directions.

A.1.9 CG2-CD10

The confining pressure was further reduced to 20 ksi with results similar to CG2-CD09. Various strain measurements are shown plotted versus axial stress in Fig. A.4.

A.1.10 CG2-CD11

The confining pressure was further reduced to 12 ksi and material failure was attained. However, a critical point (onset of dilatation) was not observed. Various strain measurements are plotted

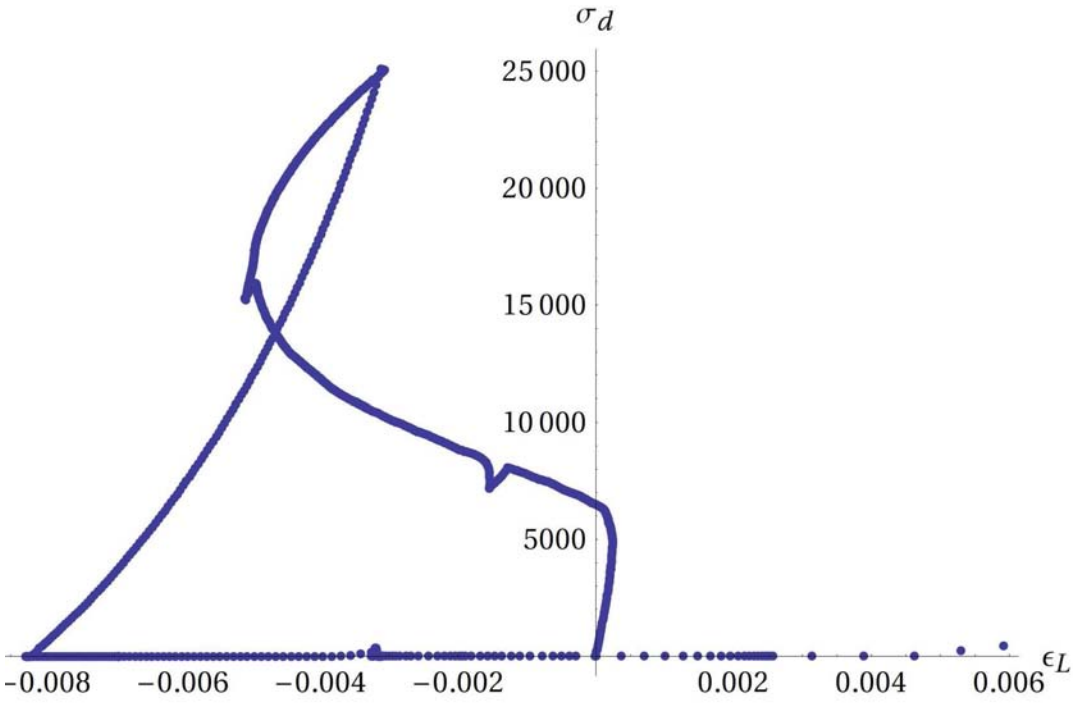


Figure A.3. Lateral strain measurement vs. differential stress from test CG2-CD06. Note that during the hydrostatic leg the lateral strain first increases, then decreases, then increases again while there is not change in loading direction. This result seems very unusual.

versus axial stress in Fig. A.5.

A.1.11 G2-CD12

The confining pressure was further reduced to 7 ksi, and again material failure was attained. As with CG2-CD11 no critical point was observed.

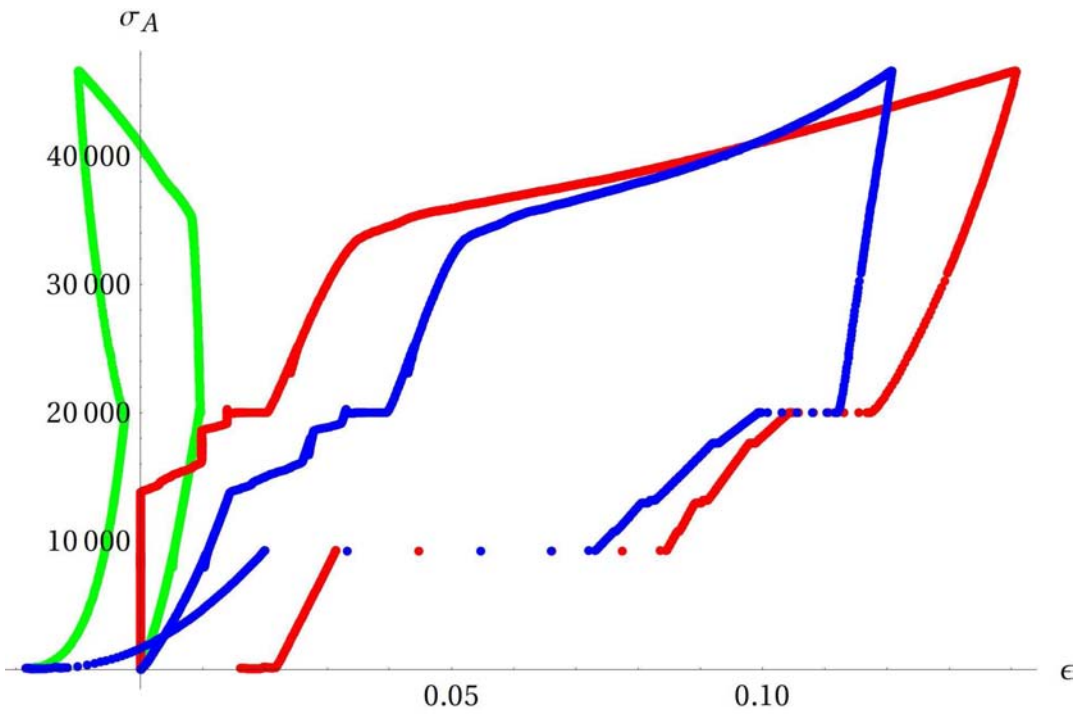


Figure A.4. Various strain measurements vs. axial stress for test CG2-CD10. Red curve is the axial strain, blue is the volumetric strain, and the green is the lateral strain.

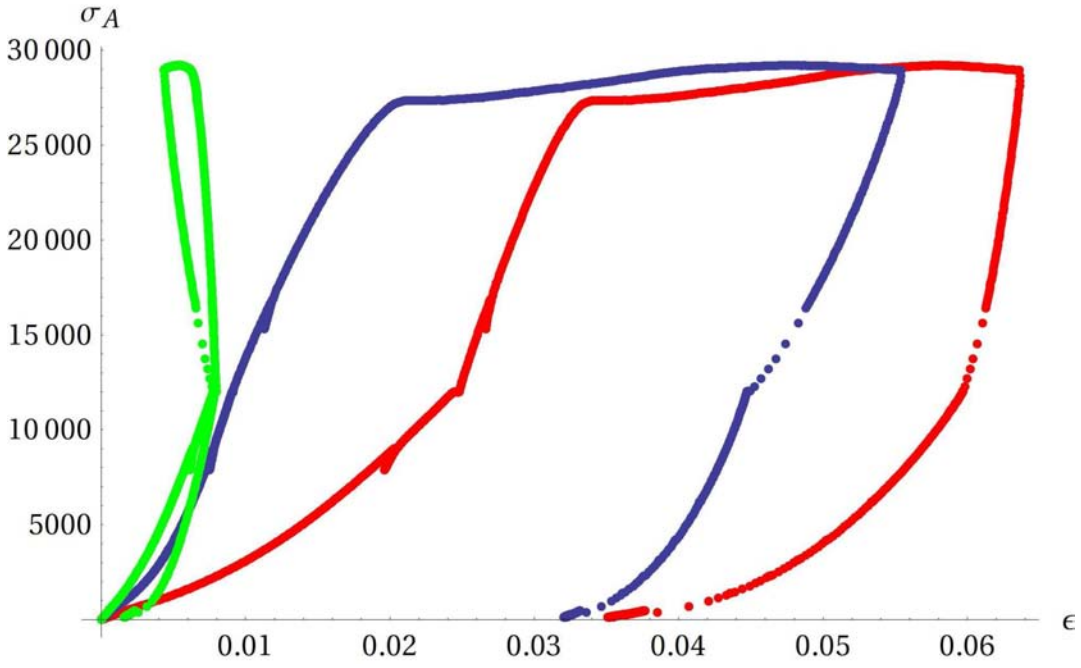


Figure A.5. Various strain measurements vs. axial stress for test CG2-CD11. Red curve is the axial strain, blue is the volumetric strain, and the green is the lateral strain.

A.2 Flow Rule Validation Tests

A.2.1 LP-TA18

This test was a calibration test. The sample was hydrostatically compressed to 20 ksi, then loaded through a triaxial path with net σ_r/σ_z angle of 110 degrees. This test was used to determine the yield strength of the material. This helped to determine where to begin the loading profile for latter tests. Summary plots for this test may be found in Figs. A.6, A.7, and A.8.

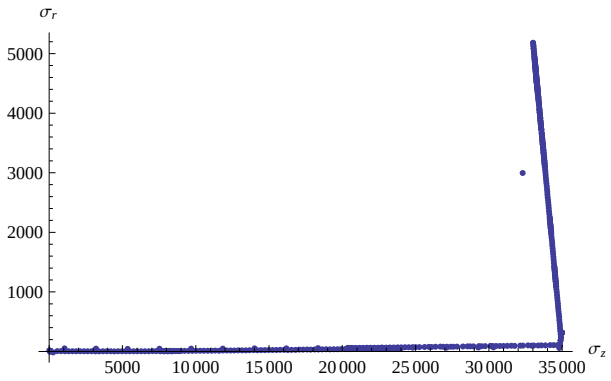


Figure A.6. The loading path for test LP-TA18 in r-z stress space

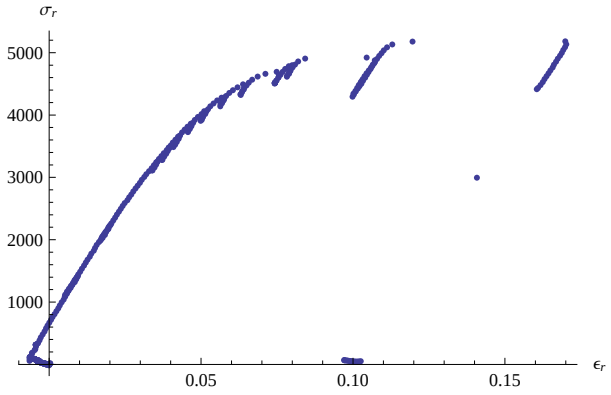


Figure A.7. The σ_r/ε_r stress strain plot for test LP-TA18.

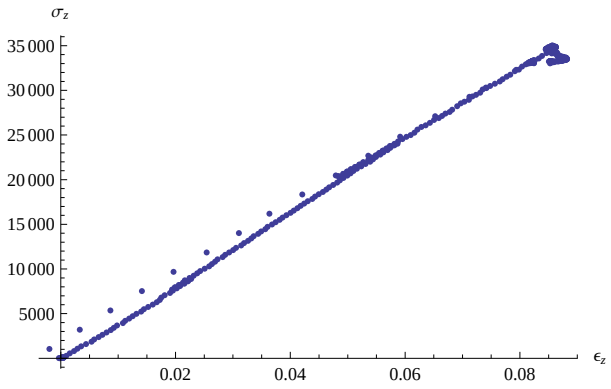


Figure A.8. The σ_z/ε_z stress strain plot for test LP-TA18.

A.2.2 LP-TA19

This test used the same net path as LP-TA18. When the stress difference reached 3500 psi the zig-zag load path was initiated. This load path was continued until the material failed. One of the three axial strain gages was not in good agreement with the other two. The lateral gage readings appeared to be good. This data included tags that indicate the beginning and end of each leg and step in the loading path. These tags are used to extract the incremental vectors from the data. The unloading increments used in this test were too small to allow useful data to be subtracted. Fig. A.12 is a plot of shear stress versus shear strain for tests LP-TA18 and LP-TA19. The plot seems to indicate work-hardening in sample LP-TA19. Summary plots for this test may be found in Figs. A.9, A.10, and A.11.

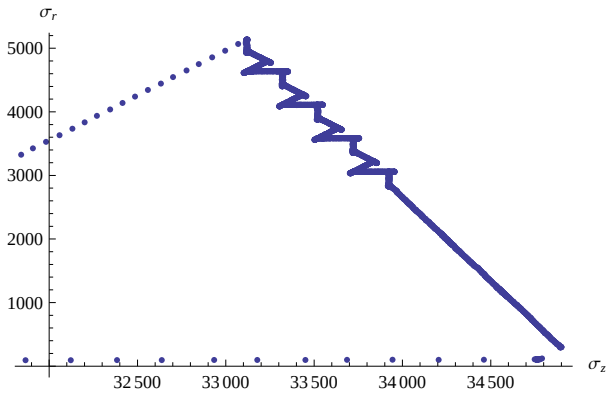


Figure A.9. The loading path for test LP-TA19 in r-z stress space

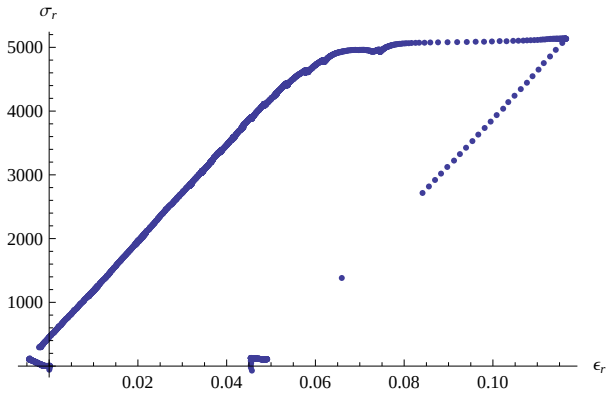


Figure A.10. The σ_r/ε_r stress strain plot for test LP-TA19.

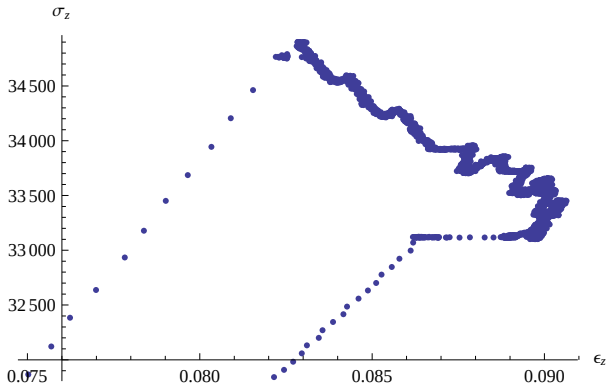


Figure A.11. The σ_z/ε_z stress strain plot for test LP-TA19.

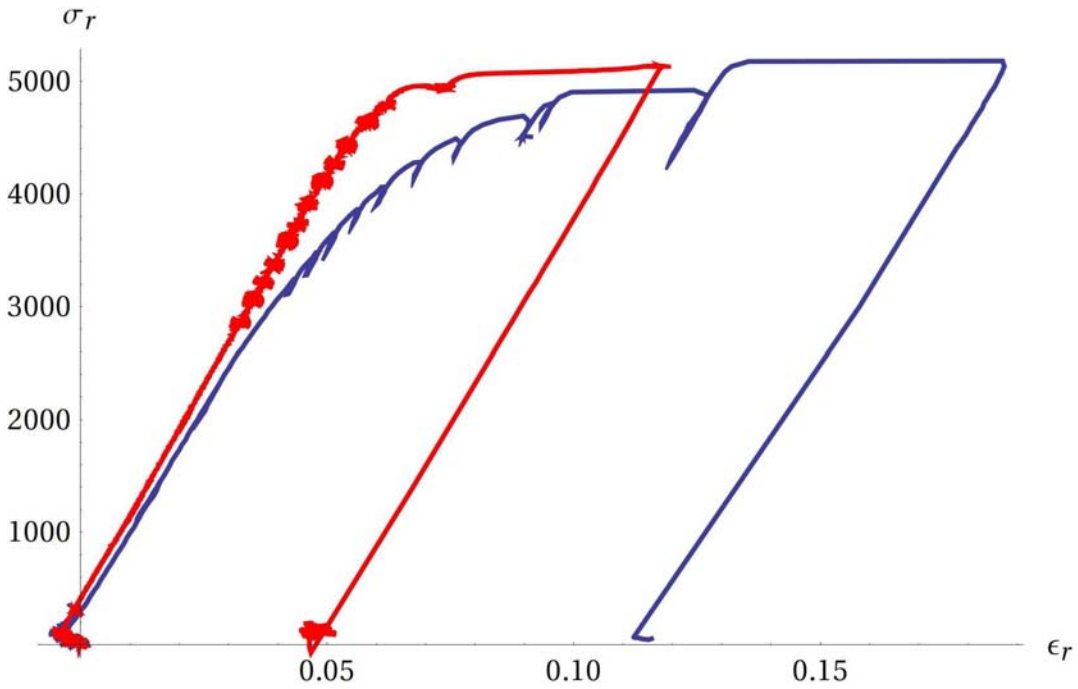


Figure A.12. Equivalent shear stress σ_r versus equivalent shear strain ε_r for test LP-TA18 (blue) and LP-TA19 (red).

A.2.3 LP-TA20

This data was similar to LP-TA19, except is was performed at a lower confining pressure. This data did not include tags indicating the beginning and end of the steps. For this reason the incremental vectors were not extracted from the data. Summary plots for this test may be found in Figs. A.13, A.14, and A.15.

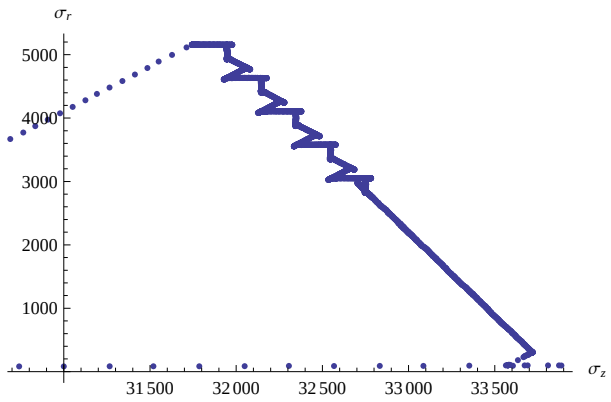


Figure A.13. The loading path for test LP-TA20 in r-z stress space

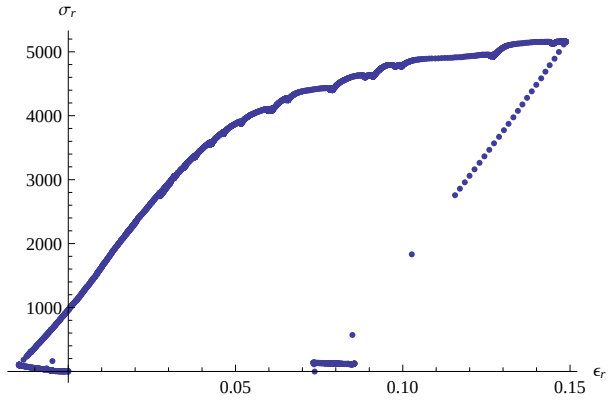


Figure A.14. The σ_r/ε_r stress strain plot for test LP-TA20.

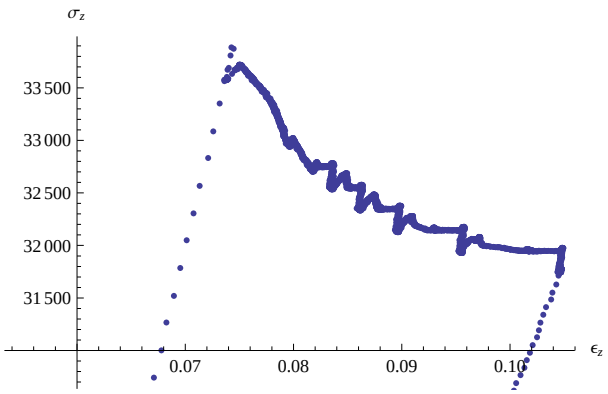


Figure A.15. The σ_z/ε_z stress strain plot for test LP-TA20.

A.2.4 LP-TA21

This data was similar to LP-TA19, except it was performed at a lower confining pressure. This data did include the leg and step tags. However, the unloading increments for this test were also too small to allow useful data to be extracted. Summary plots for this test may be found in Figs. A.16, A.17, and A.18.

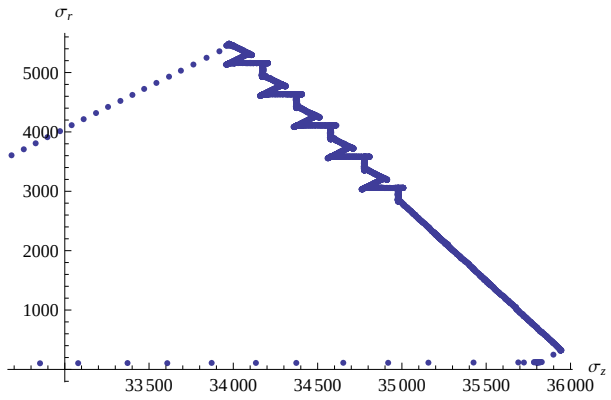


Figure A.16. The loading path for test LP-TA21 in r-z stress space

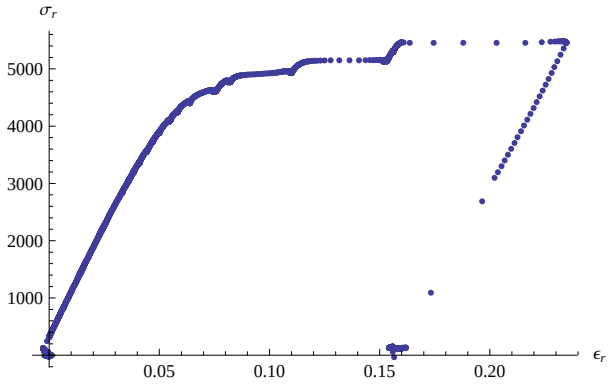


Figure A.17. The σ_r/ε_r stress strain plot for test LP-TA21.

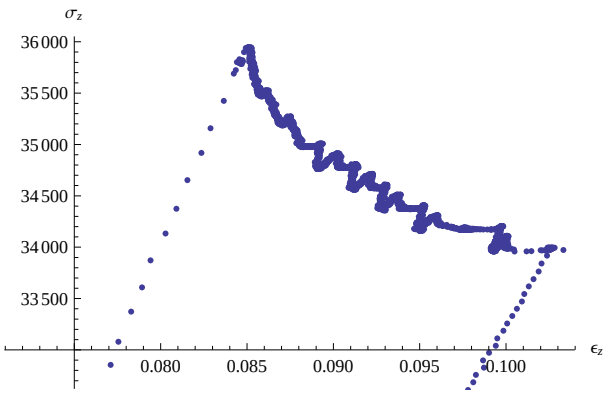


Figure A.18. The σ_z/ε_z stress strain plot for test LP-TA21.

A.2.5 LP-TA22

The loading profile was changed for this dataset. The loading increments were increased from 230 psi in magnitude to 300 psi. The loading increments were chosen to be the same magnitude as the loading increments, but with opposite direction. This means that each loading increment is fully unloaded, the reloaded. This allows useful information to be extracted from both the loading and unloading increments. Also, since the loading legs are fully unloaded, the plastic strain can be directly measured by measuring the strain that remains after unloading each stress increment. This proved to be very useful. Summary plots for this test may be found in Figs. A.19, A.20, and A.21.

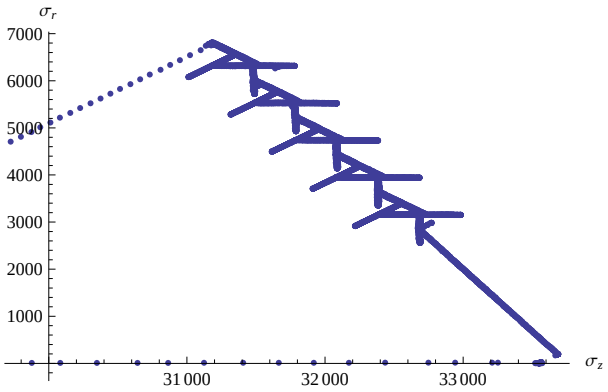


Figure A.19. The loading path for test LP-TA22 in r-z stress space

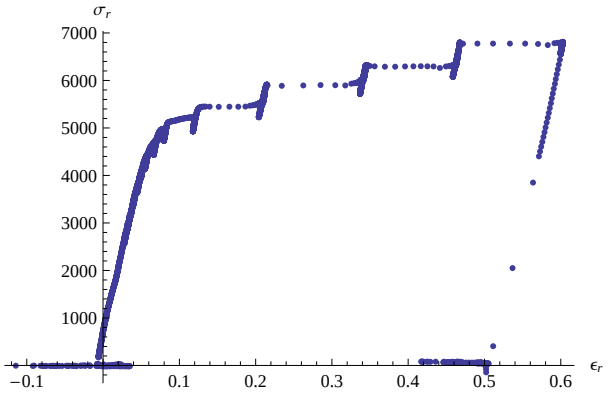


Figure A.20. The σ_r/ε_r stress strain plot for test LP-TA22.

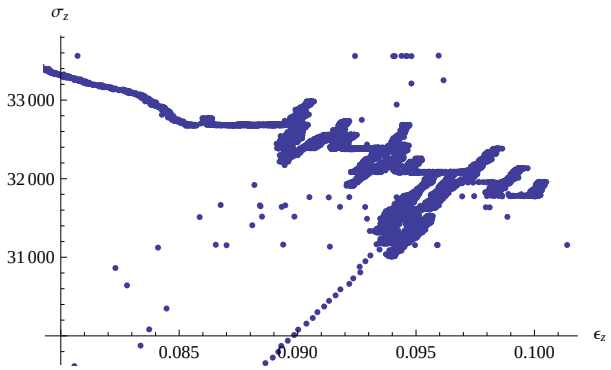


Figure A.21. The σ_z/ε_z stress strain plot for test LP-TA22.

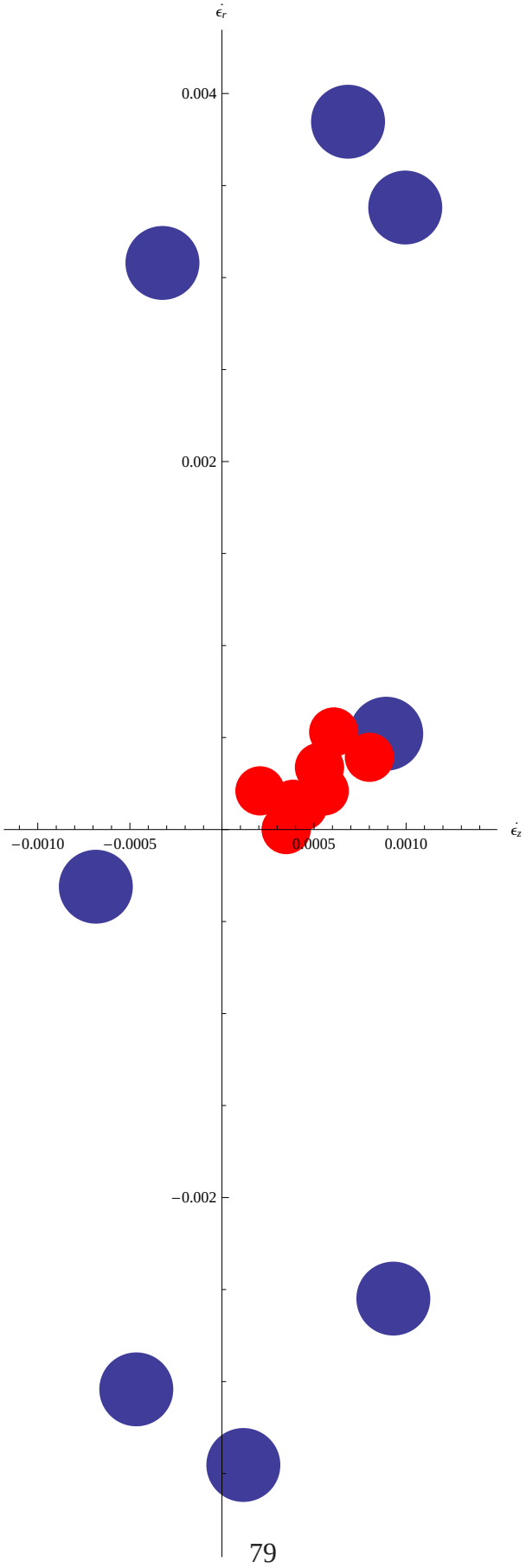


Figure A.22. Strain response envelope for the second loading cycle for test LP-TA22.

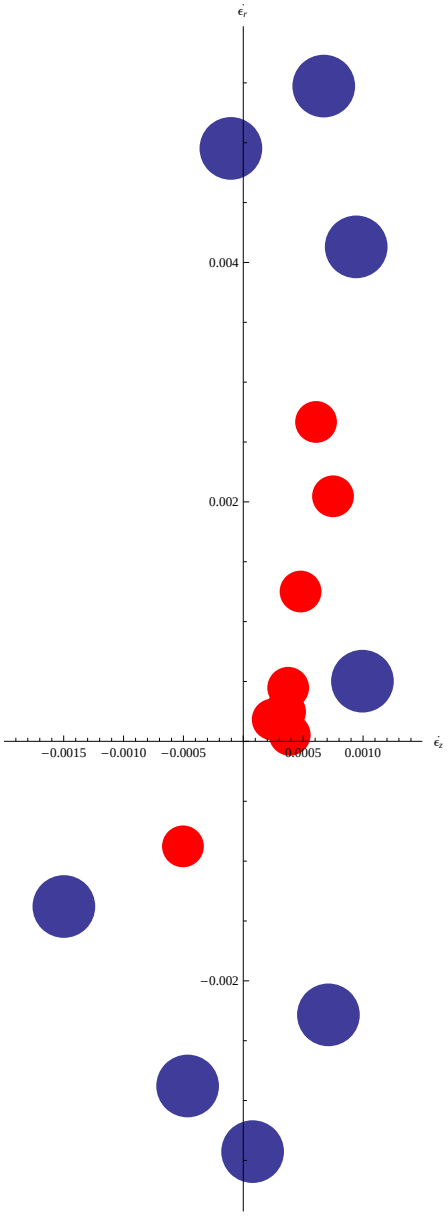


Figure A.23. Strain response envelope for the third loading cycle for test LP-TA22.

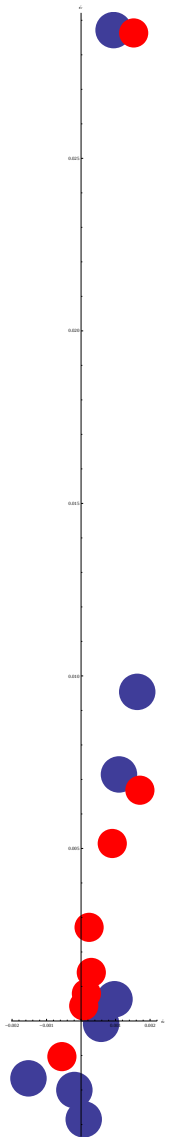


Figure A.24. Strain response envelope for the fourth loading cycle for test LP-TA22.

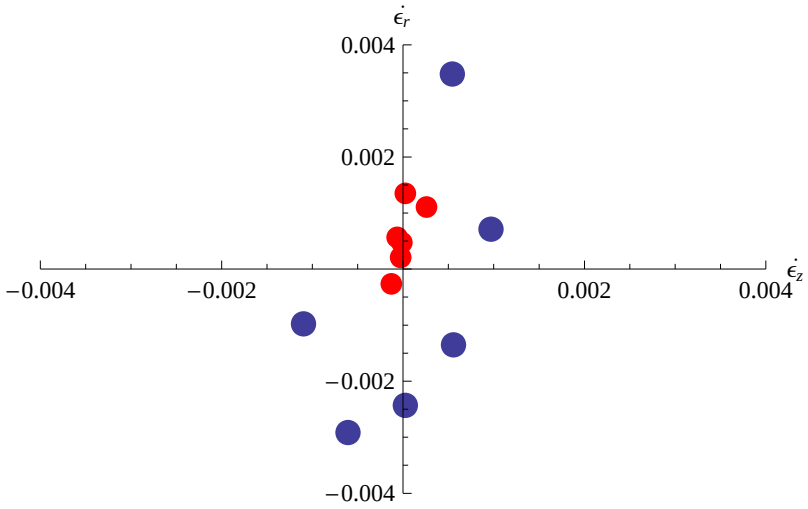


Figure A.25. Strain response envelope for the fifth loading cycle for test LP-TA22.

A.2.6 LP-TA23

This test was similar to LP-TA23, only at a slightly lower pressure. Summary plots for this test may be found in Figs. A.26, A.27, and A.28.

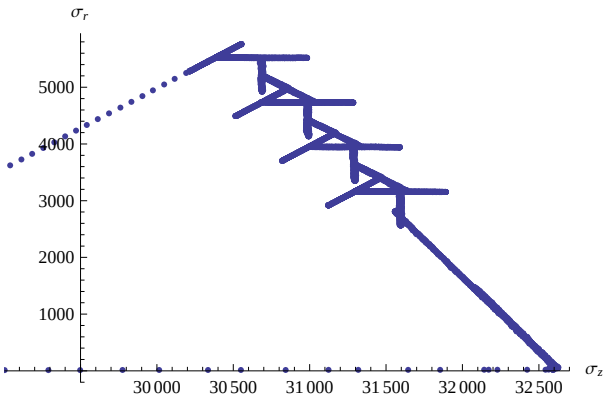


Figure A.26. The loading path for test LP-TA23 in r-z stress space

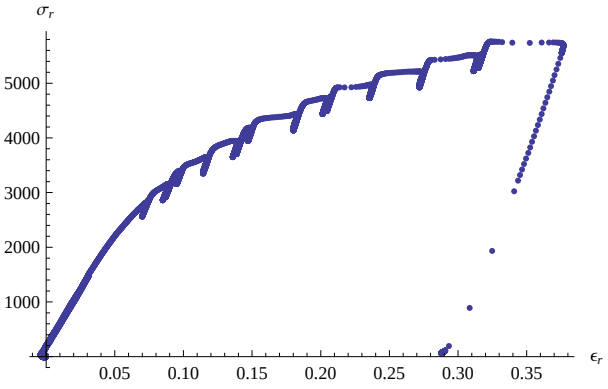


Figure A.27. The σ_r/ε_r stress strain plot for test LP-TA23.

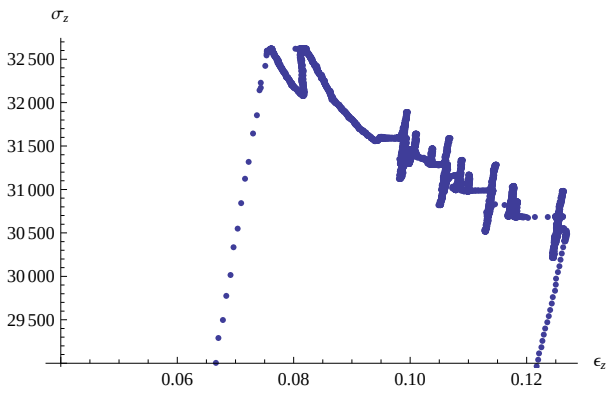


Figure A.28. The σ_z/ε_z stress strain plot for test LP-TA23.

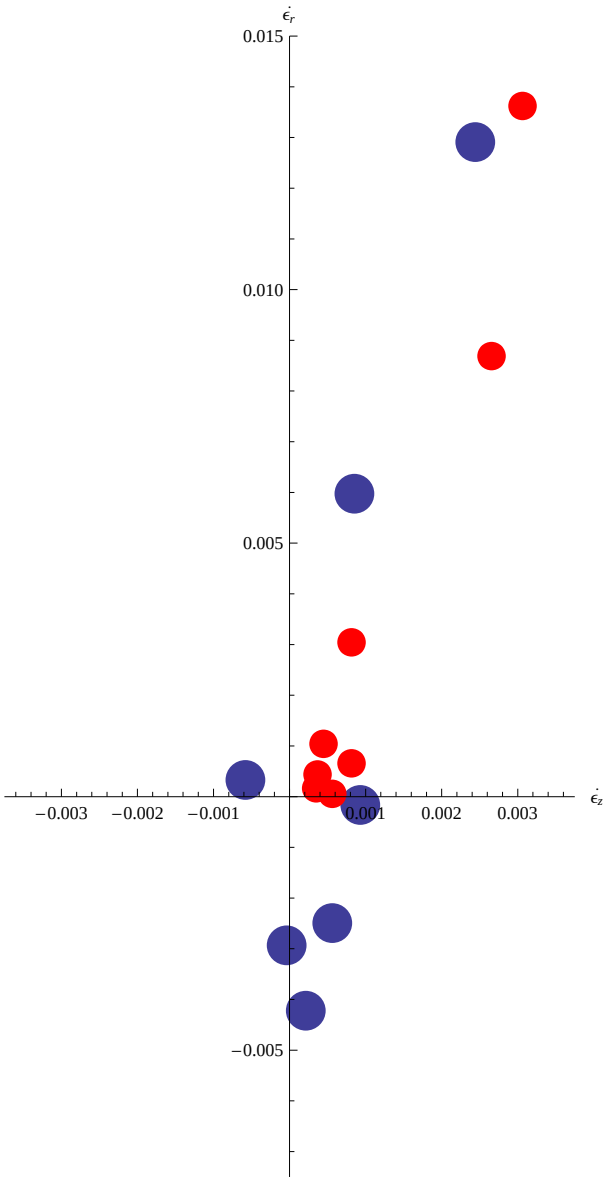


Figure A.29. Strain response envelope for the second loading cycle for test LP-TA23.

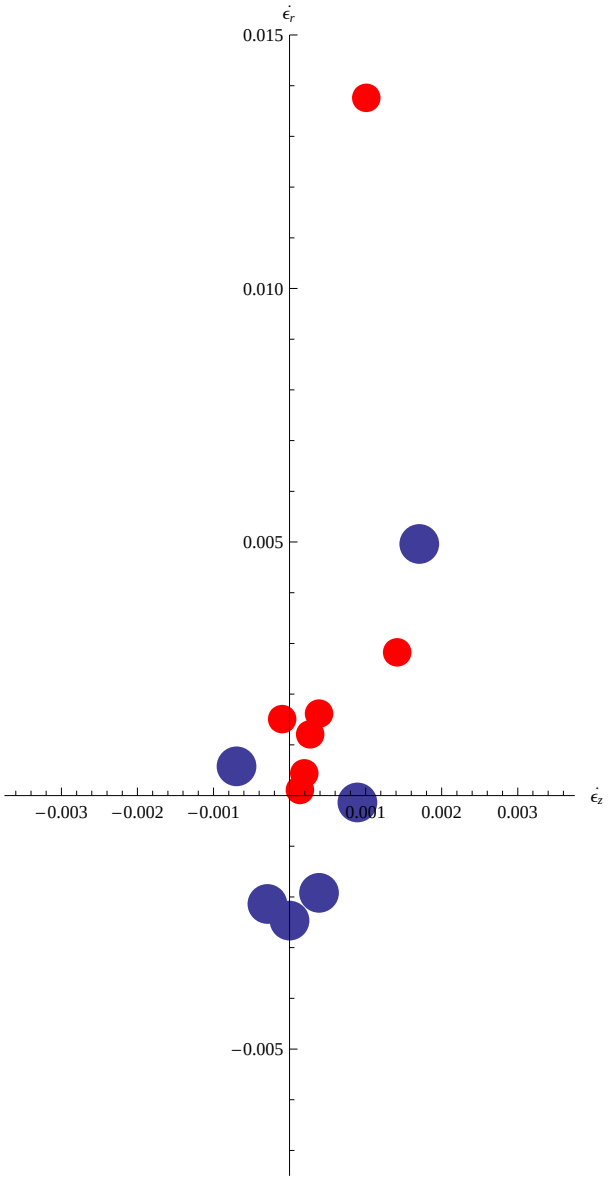


Figure A.30. Strain response envelope for the third loading cycle for test LP-TA23.

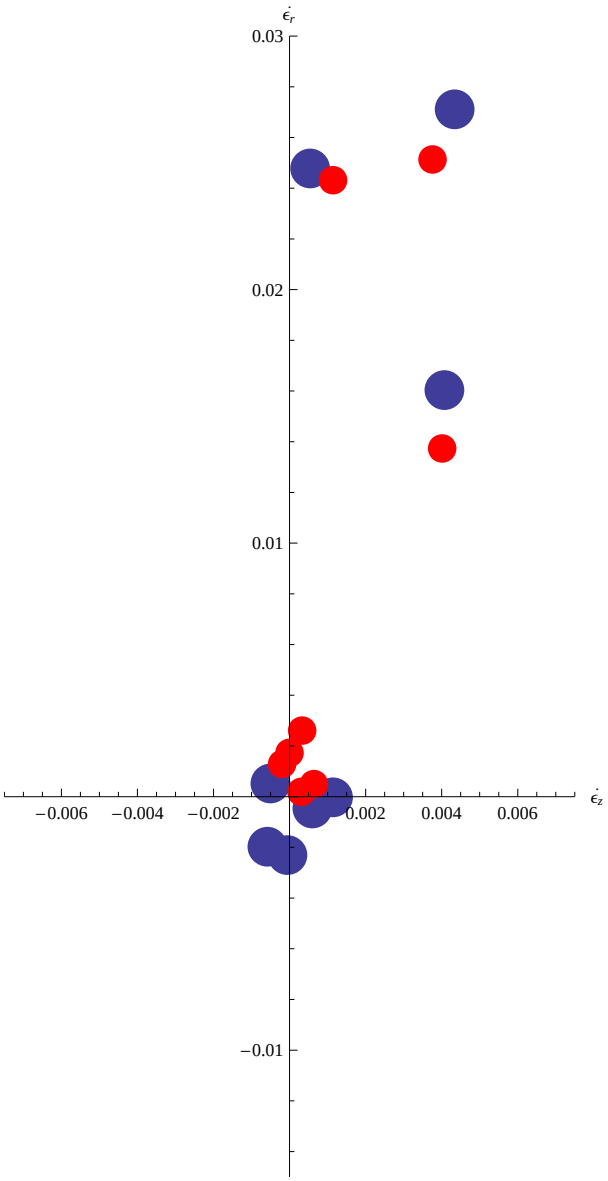


Figure A.31. Strain response envelope for the fourth loading cycle for test LP-TA23.

A.2.7 LP-TA24

This test was similar to LP-TA23, but performed at a slightly lower pressure. Summary plots for this test may be found in Figs. A.32, A.33, and A.34.

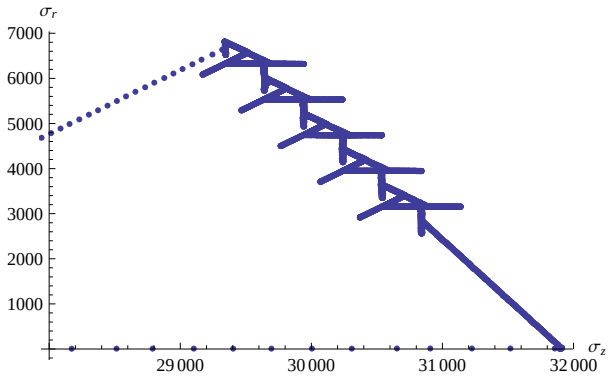


Figure A.32. The loading path for test LP-TA24 in r-z stress space

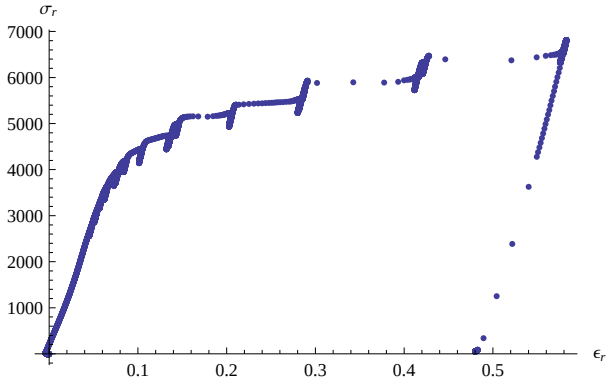


Figure A.33. The σ_r/ε_r stress strain plot for test LP-TA24.

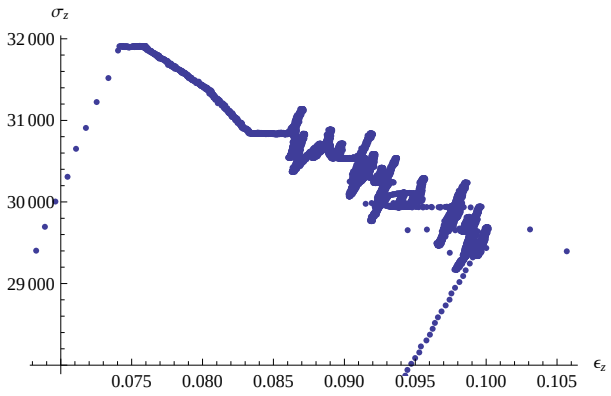


Figure A.34. The σ_z/ε_z stress strain plot for test LP-TA24.

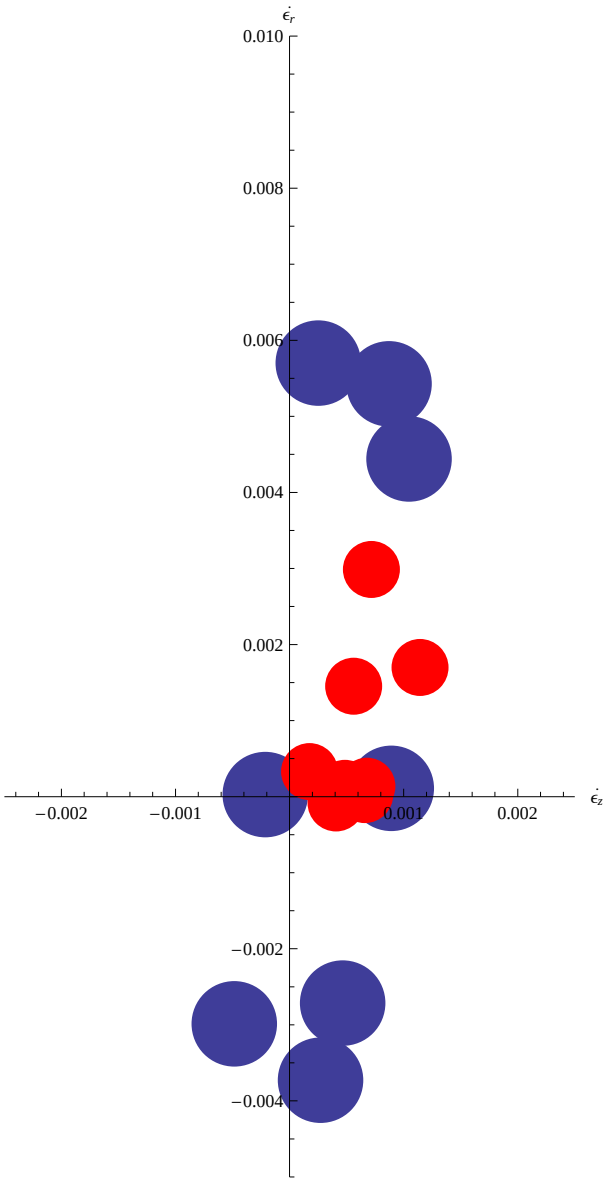


Figure A.35. Strain response envelope for the second loading cycle for test LP-TA24.

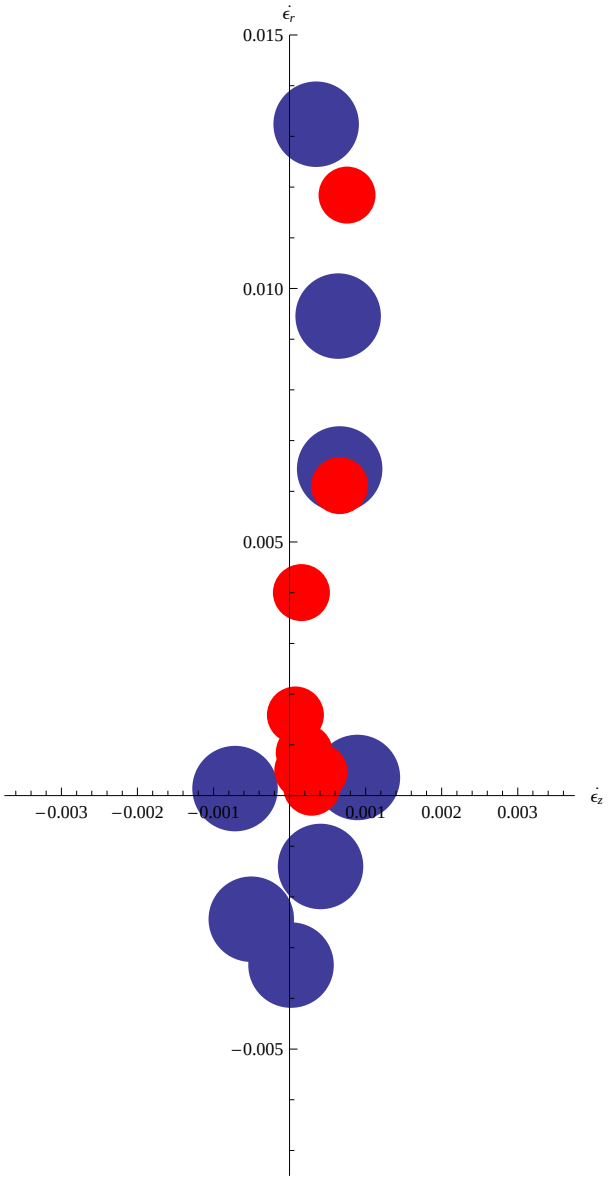


Figure A.36. Strain response envelope for the third loading cycle for test LP-TA24.

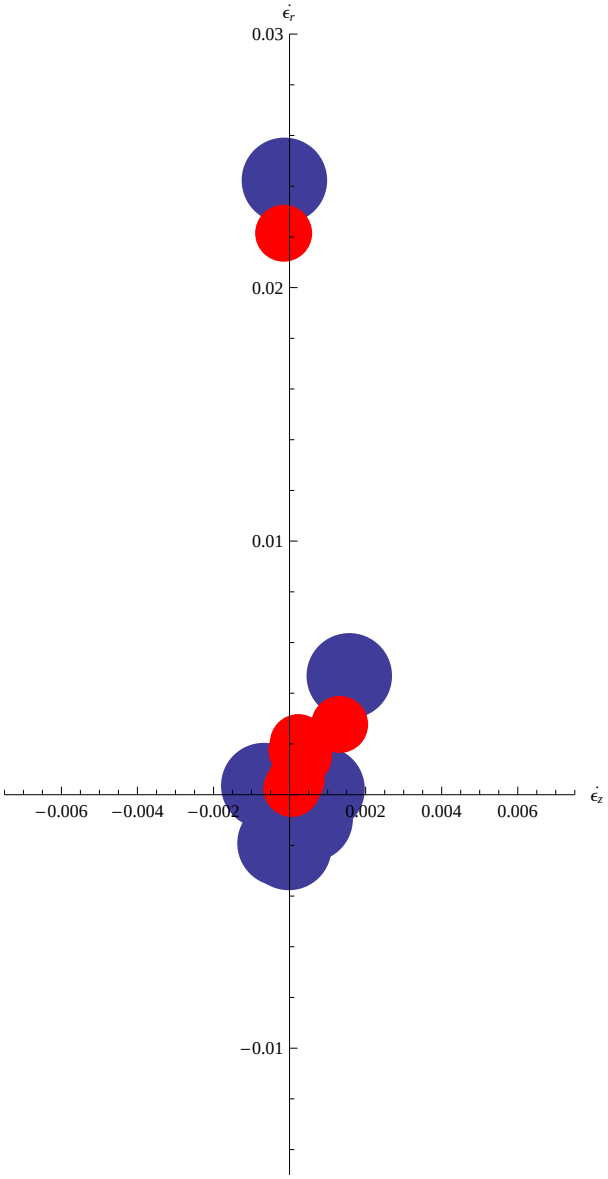


Figure A.37. Strain response envelope for the fourth loading cycle for test LP-TA24.

A.2.8 LP-TA25

This test followed the same net load path as LP-TA22, but did not change loading direction. This test was included for comparison with the load paths with changes in loading direction. Summary plots for this test may be found in Figs. A.38, A.39, and A.40.

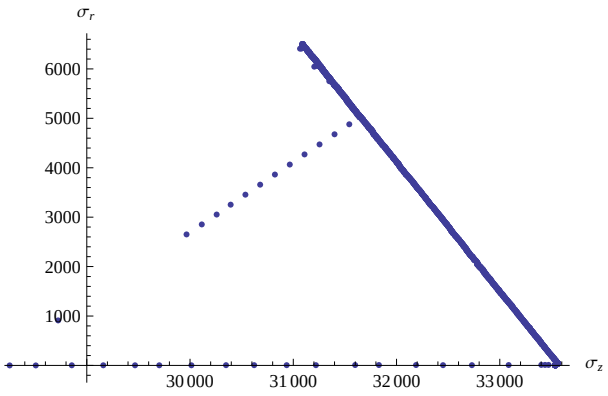


Figure A.38. The loading path for test LP-TA25 in r-z stress space

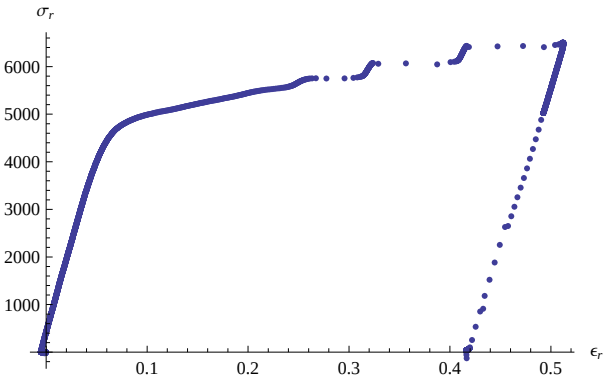


Figure A.39. The σ_r/ε_r stress strain plot for test LP-TA25.

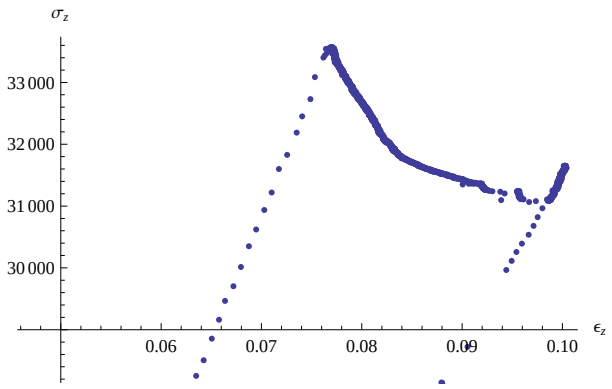


Figure A.40. The σ_z/ε_z stress strain plot for test LP-TA25.

A.2.9 LP-TA26

This test used an initial confining pressure of 10 ksi, and then followed the net loading path with no changes in the loading direction. Summary plots for this test may be found in Figs. A.41, A.42, and A.43.

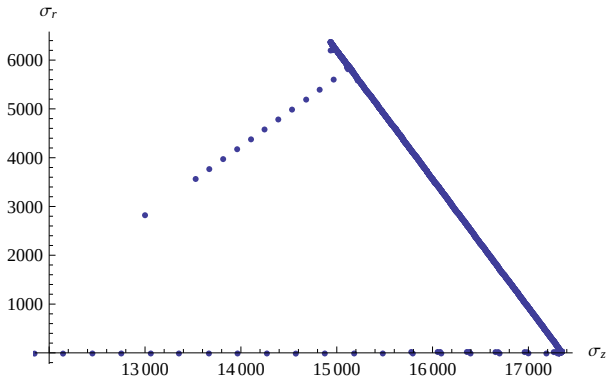


Figure A.41. The loading path for test LP-TA26 in r-z stress space

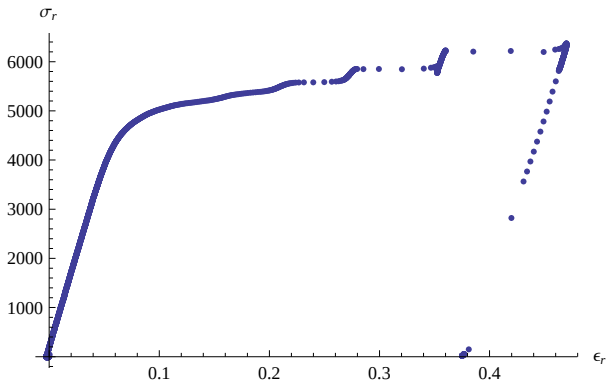


Figure A.42. The σ_r/ε_r stress strain plot for test LP-TA26.

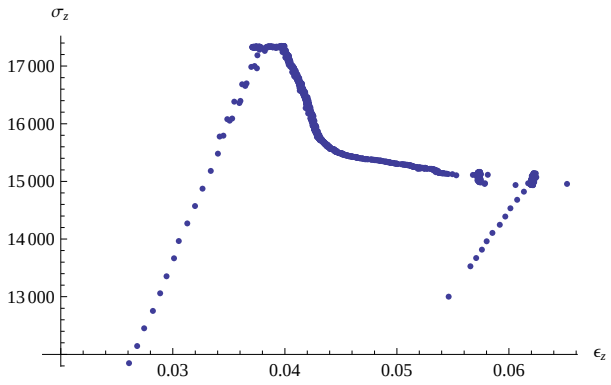


Figure A.43. The σ_z/ε_z stress strain plot for test LP-TA26.

A.2.10 LP-TA27

This test used an initial confining pressure of 10 ksi, then used then loaded to just below the yield point, and began applying loading increments in several directions. The loading and unloading increments both had a magnitude of 300 psi. Summary plots for this test may be found in Figs. A.44 through A.49 .

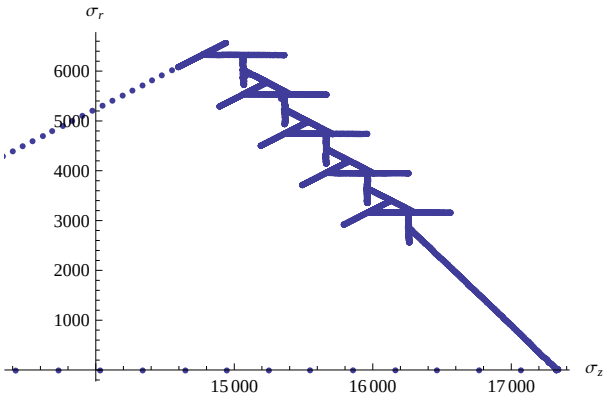


Figure A.44. The loading path for test LP-TA27 in r-z stress space

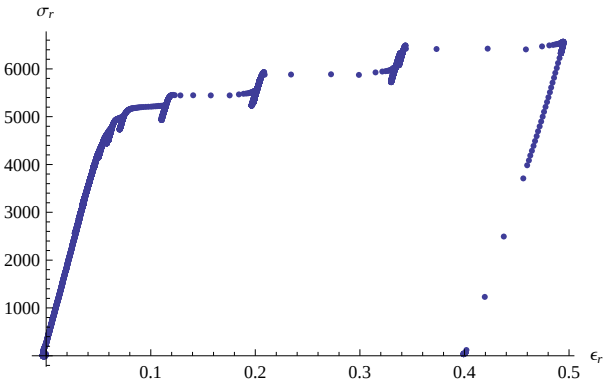


Figure A.45. The σ_r/ε_r stress strain plot for test LP-TA27.

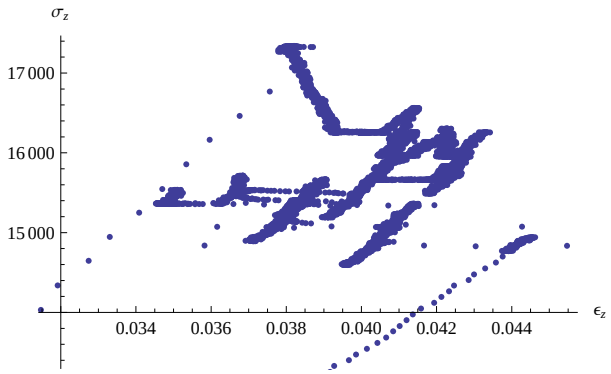


Figure A.46. The σ_z/ε_z stress strain plot for test LP-TA27.

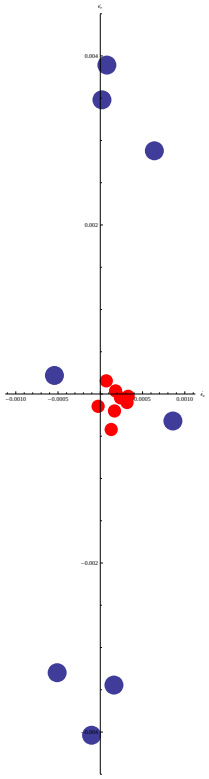


Figure A.47. Strain response envelope for the second loading cycle for test LP-TA27.

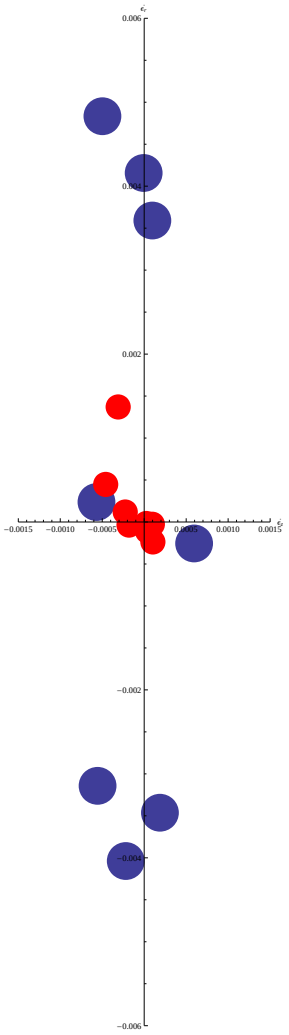


Figure A.48. Strain response envelope for the third loading cycle for test LP-TA27.

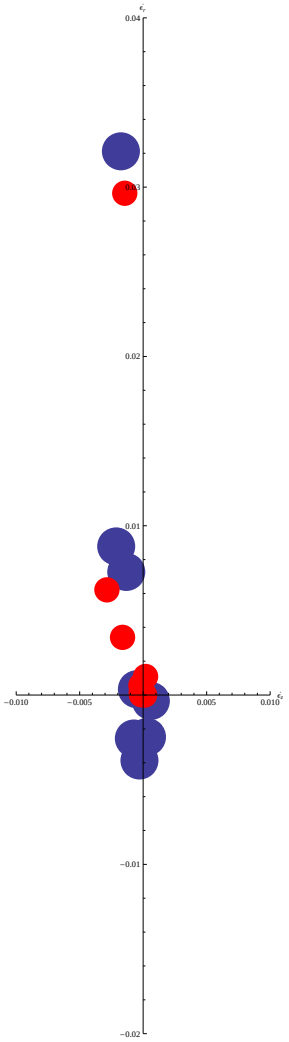


Figure A.49. Strain response envelope for the fourth loading cycle for test LP-TA27.

A.2.11 CD2-LP02

This test was performed using a sample of Castlegate sandstone, and used an initial confining pressure of 20 ksi. It then followed a loading path with an σ_r/σ_z angle of 110 degrees until the sample failed. This test was used do find the yield point for use with test CG2-LP03. Summary plots are shown in Figs. A.50 through A.52.

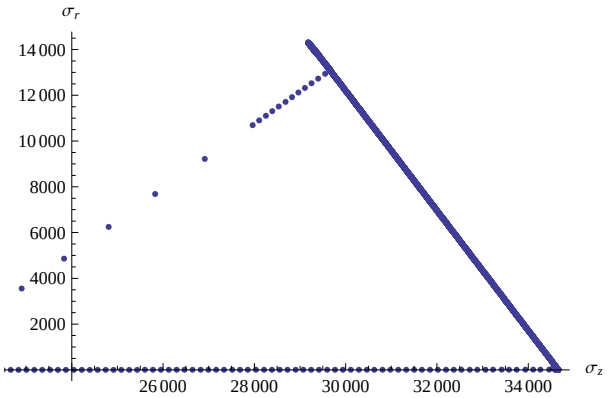


Figure A.50. The loading path used for test CG2-LP02

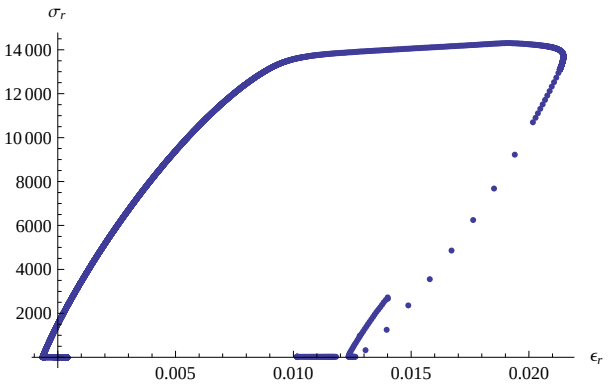


Figure A.51. Stress (σ_r) vs. strain (ε_r) plot for test CG2-LP02

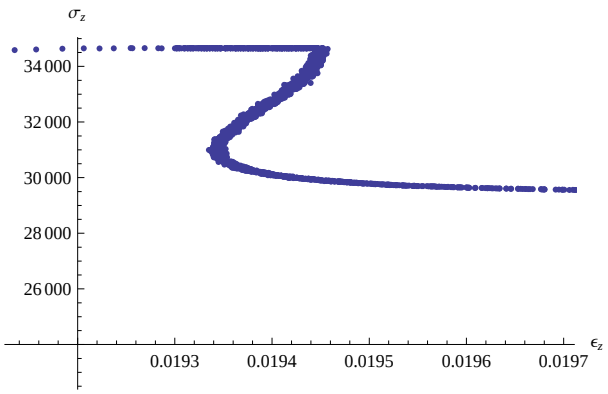


Figure A.52. Stress (σ_z) vs. strain (ε_z) plot for test CG2-LP02

A.2.12 CG2-LP03

This test followed the same net path as CG2-LP02, but began applying loading increments in multiple directions just before the yield limit was reached. Summary plots are found in Figs. A.53 through A.65.

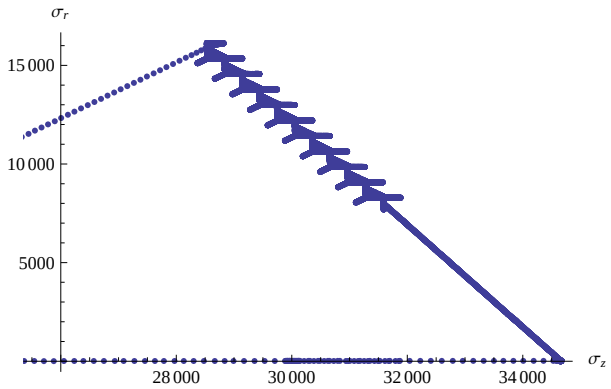


Figure A.53. The loading path used for test CG2-LP03

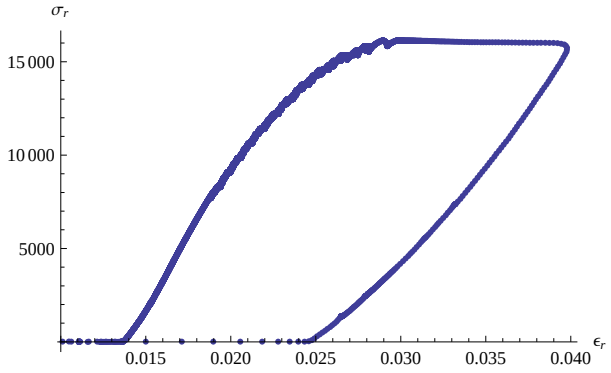


Figure A.54. Stress (σ_r) vs. strain (ε_r) plot for test CG2-LP03

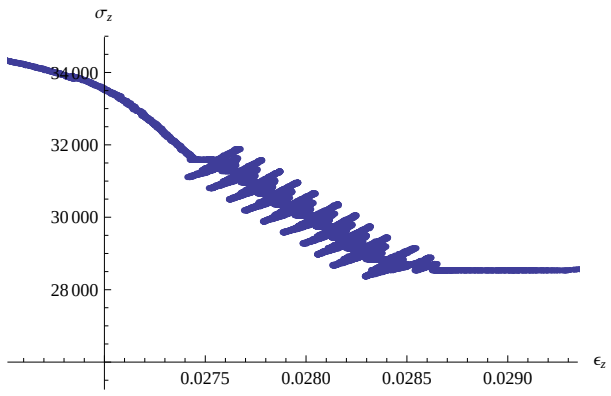


Figure A.55. Stress (σ_z) vs. strain (ε_z) plot for test CG2-LP03

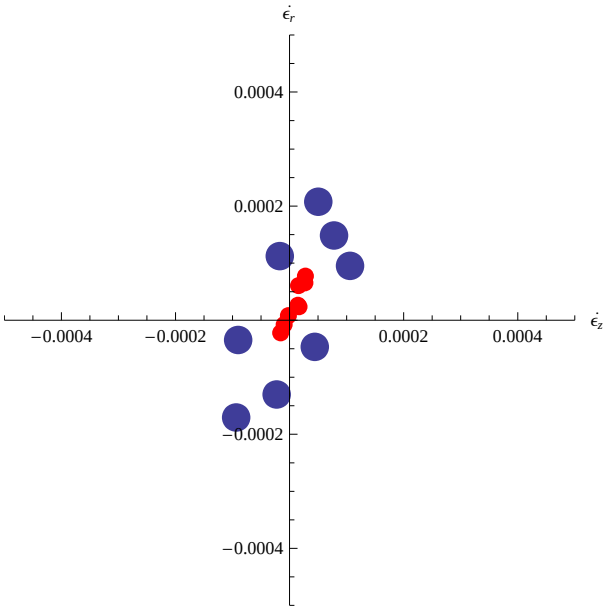


Figure A.56. Strain response envelope for the second loading cycle of test CG2-LP03.

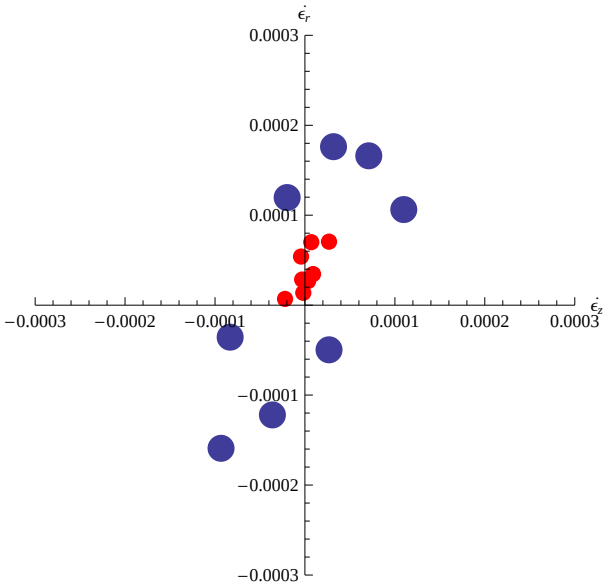


Figure A.57. Strain response envelope for the third loading cycle of test CG2-LP03.

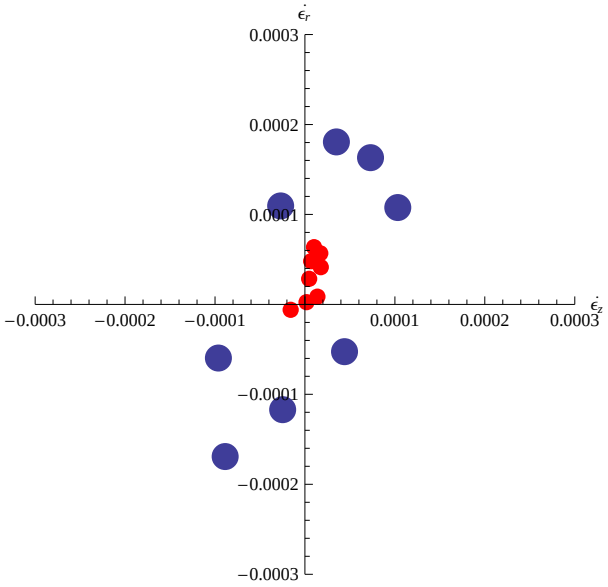


Figure A.58. Strain response envelope for the fourth loading cycle of test CG2-LP03.

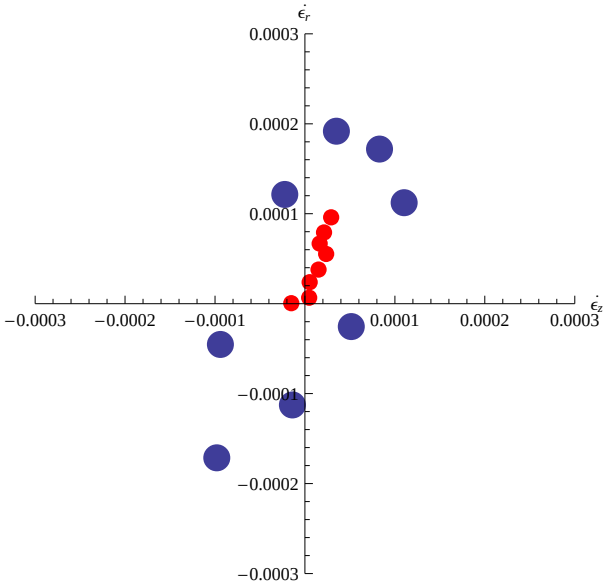


Figure A.59. Strain response envelope for the fifth loading cycle of test CG2-LP03.

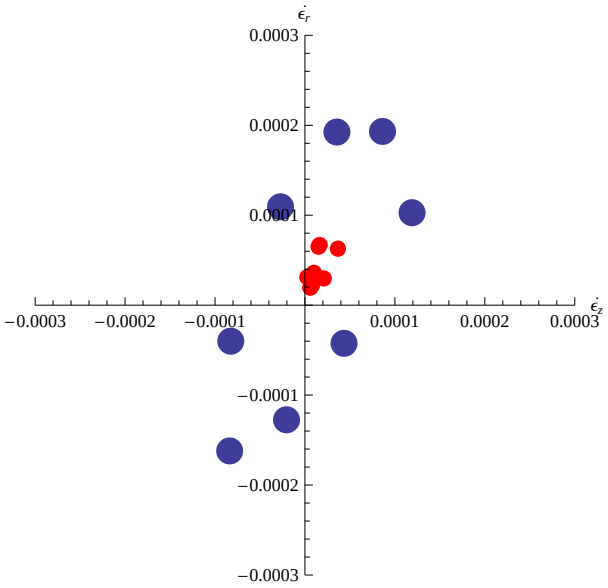


Figure A.60. Strain response envelope for the sixth loading cycle of test CG2-LP03.

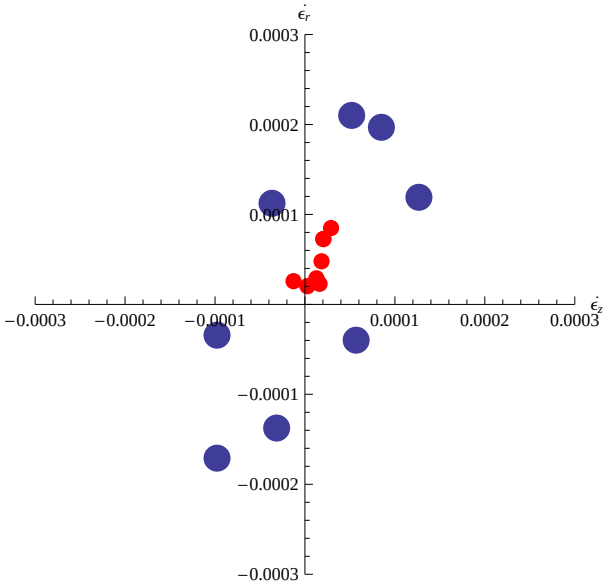


Figure A.61. Strain response envelope for the seventh loading cycle of test CG2-LP03.

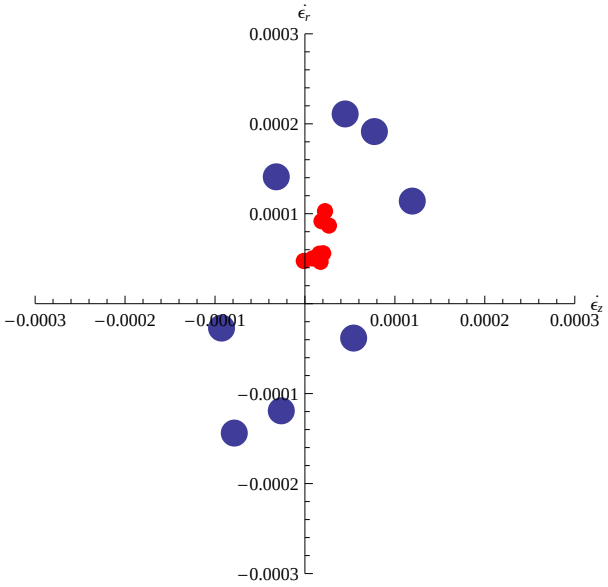


Figure A.62. Strain response envelope for the eighth loading cycle of test CG2-LP03.

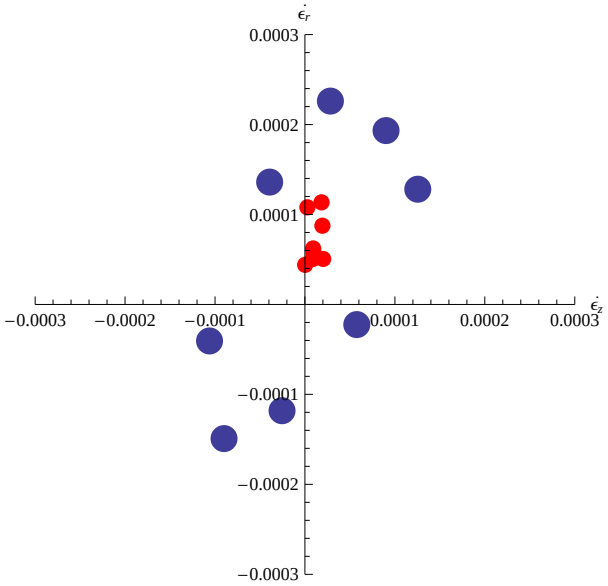


Figure A.63. Strain response envelope for the ninth loading cycle of test CG2-LP03.

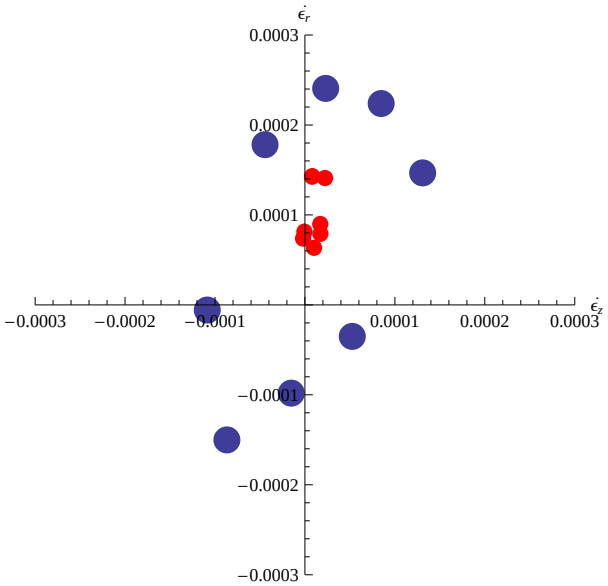


Figure A.64. Strain response envelope for the tenth loading cycle of test CG2-LP03.

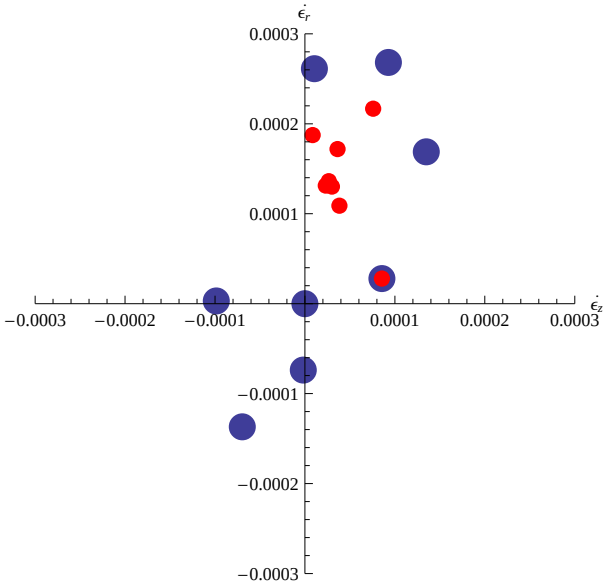


Figure A.65. Strain response envelope for the eleventh loading cycle of test CG2-LP03.

DISTRIBUTION:

1 Elias C. Aifantis
Mechanical Engineering - Engineering Mechanics
College of Engineering
1400 Townsend Drive
Houghton, MI
USA 49931-1295

1 Andrew A. Wereszczak
Metals & Ceramics Division
Oak Ridge National Laboratory
P. O. Box 2008
Oak Ridge, TN 37831-6068

1 Robert McMeeking
Fraser Noble Building Rm. F028
Kings College
Aberdeen AB24 3UE
Scotland
United Kingdom

1 Howard L. Schreyer
Department of Mechanical Engineering
The University of New Mexico
Albuquerque, NM 87131

1 Carl Krauthauser
U.S. Army Research Laboratory
Armor Mechanics Branch
ATTN: AMSRD-ARL-WM-TA
Aberdeen Proving Ground, MD 21005-5066

1 Charles Anderson
Engineering Dynamics Department
Southwest Research Institute
9503 W Commerce
San Antonio, Texas 78227-1301

1 David Benson
Dept. of Mechanical and Aerospace Engineering
University of California
Gilman Drive
La Jolla, CA 920

1 David M. Stepp
U.S. Army Research Office
P.O. Box 12211
Research Triangle Park, NC 27709-2211

1 Donald A. Simons
Northrop Grumman Corp.
W. Sixth St.
PO BOX 471
San Pedro, CA 90733-047

1 Eugene Sevin
1782 Kenton Circle
Lyndhurst, OH 44124-304

1 Frank Addessio
PO Box 1663
Los Alamos, NM 87545

1 George Z.Voyiadjis
12718 N. Oak Hills Pkwy.
Baton Rouge, LA 70810

1 Gianluc Cusatis
Department of Civil and Envir= onmental Engineering
Johnsson Engineering Center
Rensselaer Polytechnic Institute
Eighth St
Troy, NY 12180-359

1 Igor Sevostianov
New Mexico State University
AMSC 3450
1040 South Horseshoe
Las Cruces, NM 8800

1 Ivan Sandler
Weidlinger Associates Inc.
375 Hudson Street
New York, NY 10014-3656

1 James Caruthers
Forney Hall, Room 2043
Purdue University
480 Stadium Mall Drive
West Lafayette, IN 47907-2100

1 James D. Walker
Computational constitutive modeling
Southwest Research Institute
9503 W Commerce
San Antonio, Texas 78227-1301

1 Joe Wells
102 Pine Hill Blvd
Mashpee, MA 02649-2869

1 John Rowe
Combat Systems
ATTN: SFAE-GCS-CS (John Rowe)
65011East Eleven Mile Road
Warren, MI 48397-500

1 Kaushik A. Iyer
17000 Science Drive, Suite 200
Bowie, MD 2071

1 Kent T. Danielson
U.S. Army Engineer Research and Development Center
Impact & Explosion Effects Branch
3909 Halls Ferry Rd,
Vicksburg, MS 39180-6199

1 Ken Zuo
Mechanical & Aerospace Engineering
The University of Alabama
N274 Technology Hall
Huntsville, Alabama 35899

1 Larry Behrmann
14910 Airline Rd
Rosharon, TX 77583

1 Len Schwer
Schwer Engineering & Consulting Services
6122 Aaron Court
Windsor, CA 95492-865

1 Mark Kachanov
Tufts University
200 College Avenue
Anderson Hall
Medford MA 02155

1 SIA NEMAT-NASSER
Center of Excellence for Advanced Materials
Department of Mechanical and Aerospace Engineering
University of California, San Diego
4209 Engineering Building 1
9500 Gilman Drive
La Jolla, CA 92093-0416

1 Nicolaie Cristescu
Department of Mechanical and Aerospace Engineering
University of Florida
231 Aero. Bldg.
PO Box 116250
Gainesville, Florida 32611-625

1 Raja K Mishra
General Motors Corp
Mail Code 480-106-212
Research & Development Center
30500 Mound Road
Warren, MI 4831

1 Dr. Ravi Chandran
Department of Metallurgical Engineering
University of Utah
135 South 1460 East Room 412,
Salt Lake City, UT 84112

1 Reaz A. Chaudhuri
Material Science and Engineering
50 S Central Campus Dr. Room 4102 MEB
Salt Lake City, UT 84112

1 Roger Ghanem
University of Southern California
Department of Aerospace and Mechanical Engineering
Los Angeles, CA 90089-2531

1 Scott Schoenfeld
U.S. Army Research Laboratory
Armor Mechanics Branch
ATTN: AMSRD-ARL-WM-TA
Aberdeen Proving Ground, MD 21005-5066

1 E.S. Folias
Department of Mathematics
155 S. 1400 E.
Salt Lake City, Utah 84112

1 Tom Stoughton
Manufacturing Systems Research Lab
GM R&D Center
30500 Mound Road
Warren, MI 48090-9055

1 Walter Gerstle
Civil Engineering
MSC01 1070
1 University Of New Mexico
Albuquerque, NM 87131-0001

1 Weinong Wayne Chen
School of Aeronautics & Astronautics
Purdue University
315 N. Grant Street,
West Lafayette, IN 47907-202

1 Yuki(Yasuyuki) Horie
AFRL/MNME Munitions Directorate
2306 Perimeter Road
Eglin AFB, FL 32542

1 Félix Darve
Laboratoire 3S-R
Domaine Universitaire - BP53X
38041 Grenoble Cedex 9
France

1 Claudio Tamagnini
Dipartimento di Ingegneria Civile e Ambientale
Via G. Duranti 93-06125
Perugia
Italy

1 A. Anandarajah
Department of Civil Engineering
3400 Charles Street
Johns Hopkins University
Baltimore, Maryland 21218

1 MS 0372 John Pott, 01524
1 MS 0706 Tom Dewers, 06315
1 MS 0706 Tom Pfeifle, 06315
1 MS 0372 William M Scherzinger, 01524
1 MS 1031 Dave Bronowski, 06315
1 MS 0706 Stephen Bauer, 06315
1 MS 0751 Dale S. Preece, 06117
1 MS 0557 Daniel Segalman, 01524
1 MS 0384 Hal Morgan, 01540
1 MS 0835 James Peery, 09142
1 MS 0372 Joe Bishop, 01525
1 MS 0372 Mike Stone, 01525
1 MS 0372 Gerald Wellman, 01525
1 MS 0847 John Red-Horse, 09211
1 MS 0847 Jonathan Rath, 09127
1 MS 0751 Laurence S Costin, 06117
1 MS 0820 Paul Yarrington, 09230
1 MS 0819 Randall Summers, 09231
1 MS 0847 Rodney May, 09126
1 MS 0847 Samuel Key, 09121
1 MS 0899 Technical Library, 9536 (electronic)
1 MS 0123 D. Chavez, LDRD Office, 1011



Sandia National Laboratories